THE ROLE OF IONIC FUNCTIONALITY ON CHARGE INJECTION PROCESSES IN CONJUGATED POLYMERS AND FULLERENES

by

CHRISTOPHER DAVID WEBER

A DISSERTATION

Presented to the Department of Chemistry and Biochemistry
and the Graduate School of the University of Oregon
in partial fulfillment of the requirements
for the degree of
Doctor of Philosophy

December 2013

DISSERTATION APPROVAL PAGE

Student: Christopher David Weber

Title: The Role of Ionic Functionality on Charge Injection Processes in Conjugated Polymers and Fullerenes

This dissertation has been accepted and approved in partial fulfillment of the requirements for the Doctor of Philosophy degree in the Department of Chemistry and Biochemistry by:

Catherine J. Page	Chairperson
Mark C. Lonergan	Advisor
Victoria J. DeRose	Core Member
David C. Johnson	Core Member
Benjamin McMorran	Institutional Representative

and

Kimberly Andrews Espy	Vice President for Research and Innovation; Dean of the Graduate School

Original approval signatures are on file with the University of Oregon Graduate School.

Degree awarded December 2013

DISSERTATION ABSTRACT

Christopher David Weber

Doctor of Philosophy

Department of Chemistry and Biochemistry

December 2013

Title: The Role of Ionic Functionality on Charge Injection Processes in Conjugated Polymers and Fullerenes

Understanding the fundamental chemistry of conjugated polymers and fullerenes has been the subject of intense research for the last three decades, with the last ten years seeing increased research toward the application of these materials into functional organic electronic devices such as organic photovoltaic devices (OPVs). This field has seen significant advances is cell efficiency in just the last few years (to >10%), in large part due to the development of new donor and acceptor materials, the fine tuning of fabrication parameters to control material nanostructure, as well as the introduction of new interfacial materials such as ionically functionalized conjugated polymers, also known as conjugated polyelectrolytes (CPEs).

This dissertation aims to further understand the fundamental chemistry associated with charge injection processes in CPEs and ionically functionalized fullerenes. The role of ionic functionality on electrochemical, chemical, and interfacial charge injection processes is explored. The results presented demonstrate the use of ionic functionality to control the spatial doping profile of a bilayer structure of anionically and cationically functionalized CPEs to fabricate a p-n junction (Chapter II). The role of ionic functionality on chemical charge injection processes is explored via the reaction of polyacetylene and

polythiophene based CPEs with molecular oxygen (Chapters III and IV). The results show the dramatic effect of ionic functionality, as well as the specific role of the counterion, on the photooxidative stability of CPEs. The control of reaction pathway via counterion charge density is also explored (Chapter IV) and shows a continuum of reaction pathways based on the charge density of the counter cation. Finally, the role of ionic functionality on interfacial charge injection processes in a functional OPV is explored using a cationically functionalized fullerene derivative (Chapters V and VI). Cell performance increases due to an increase in open-circuit voltage and substantial reduction in series resistance resulting from the high conductivity of the interfacial fullerene layer. The chemical origin of this high conductivity is explored in Chapter VI and shown to likely be the result of chemical reactions occurring between the counter anion and the fullerene core.

This dissertation contains coauthored, previously published and unpublished work.

CURRICULUM VITAE

NAME OF AUTHOR: Christopher David Weber

GRADUATE AND UNDERGRADUATE SCHOOLS ATTENDED:

University of Oregon, Eugene, OR
The Richard Stockton College of New Jersey, Pomona, NJ

DEGREES AWARDED:

Doctor of Philosophy, Chemistry, 2013, University of Oregon
Master of Science, Chemistry, 2009, University of Oregon
Bachelor of Science, Chemistry, 2006, The Richard Stockton College of New Jersey

AREAS OF SPECIAL INTEREST:

Organic Photovoltaics
Organic Electronics
Electrochemistry
Photochemistry

PROFESSIONAL EXPERIENCE:

Graduate Research Assistant, Department of Chemistry and Biochemistry, University of Oregon, Eugene, OR, 2008-2013

Graduate Teaching Assistant, Department of Chemistry and Biochemistry, University of Oregon, Eugene, OR, 2007-2008

GRANTS, AWARDS, AND HONORS:

Doctoral Research Fellowship, University of Oregon, 2012-2013

National Science Foundation IGERT Fellowship, 2009-2011

PUBLICATIONS:

Weber, C.D.; Bradley, C.; Walker, E.M.; Robinson, S.G.; Lonergan, M.C. " Increased Performance of Inverted Organic Photovoltaic Cells using a Cationically Functionalized Fullerene Interfacial Layer," *submitted Sol. Eng. Mater. Sol. Cells*, 2013.

Weber, C. D.; Bradley, C.; Lonergan, M. C. "Solution Phase n-Doping of C_{60} and PCBM using Tetrabutylammonium Fluoride," *accepted J. Mater. Chem. A*, 2013.

Weber, C.D.; Robinson, S. G.; Stay, D.P.; Vonnegut, C. L.; Lonergan, M.C. "Ionic Stabilization of the Polythiophene-Oxygen Charge Transfer Complex," *ACS Macro Lett.*, **2012,** 1, 499-503.

Chase, D.T.; Fix, A.G.; Kang, K.J.; Rose, B.D.; Weber, C.D.; Zhong, Y.; Zakharov, L.N.; Lonergan, M.C.; Haley, M.M. "6,12-Diarylindeno[1,2-b]fluorenes: Syntheses, Photophysics, and Ambipolar OFETs," *J. Am. Chem. Soc.*, **2012,** 134, 10349-10352.

Chrostowska, A.; Xu, S.; Lamm, A.N.; Maziere, A.; Weber, C.D.; Dargelos, A.; Baylere, P.; Graciaa, A.; Liu, S. "UV-Photoelectron Spectroscopy of 1,2 and 1,3-Azaborines: A Combined Experimental and Computational Electronic Structure Analysis," *J. Am. Chem. Soc.*, **2012,** 134, 10279-10285.

Weber, C.D.; Robinson, S.G.; Lonergan, M.C. "Ionic Functionality and the Polyacetylene-Oxygen Charge Transfer Complex," *Macromolecules*, **2011,** 44, 4600-4604.

Chase, D.T.; Fix, A.G.; Rose, B.M.; Weber, C.D.; Nobusue, S.; Stockwell, C.E.; Zakharov, L.N.; Lonergan, M.C.; Haley, M.M. "Electron -Accepting 6,12-Diethynylindeno[1,2-b]fluorenes: Synthesis, Crystal Structures, and Photophysical Properties," *Angew. Chem. Int. Ed.*, **2011,** 50, 11103-11106.

Rose, B.D.; Chase, D.T.; Weber, C.D.; Zakharov, L.N.; Lonergan, M.C.; Haley, M.M. "Synthesis, Crystal Structures, and Photophysical Properties of Electron Accepting Diethynylindenofluorenediones," *Org. Lett.*, **2011,** 13, 2106-2109.

Robinson, S.G.; Johnson, D.H.; Weber, C.D.; Lonergan, M.C. "Polyelectrolyte Mediated Electrochemical Fabrication of a Polyacetylene p-n Junction," *Chem. Mater.*, **2010,** 22, 241-246.

ACKNOWLEDGMENTS

I would like to thank Dr. Mark Lonergan for his guidance and continuous support over the years. I would like to thank the members of the Lonergan lab, past and present, in particular those who have served as coauthors to the work presented herein. I would like to acknowledge members of the Haley and Liu labs with whom I collaborated on several projects. I also would like to express my gratitude to my committee members for their support, with a special acknowledgement of Dr. David Cohen who served as my outside committee member prior to his passing. Though I had only limited contact with Dr. Cohen over the years, the insight and advice he provided during that time is invaluable and sincerely appreciated. The work reported herein was supported by funding from the Division of Chemical Sciences, Geosciences, and Biosciences, Office of Basic Energy Sciences of the U.S. Department of Energy through Grant DE-FG02-07ER15907, National Science Foundation IGERT program under Grant No. DGE-0549503, and the University of Oregon Doctoral Research Fellowship award.

TABLE OF CONTENTS

Chapter Page

I. GENERAL INTRODUCTION 1

1.1. Dissertation Goals and Objectives 1

1.2. Organic Photovoltaic Cell Basics 3

1.2.1. Charge Photogeneration 3

1.2.2. Open-Circuit Voltage 6

1.2.3. Short-Circuit Current Density 7

1.2.4. Fill Factor 8

1.3. Electrochemical Charge Injection in Conjugated Polymers and CPEs 9

1.4. Chemical Charge Injection in Conjugated Polymers and CPEs 13

1.5. Interfacial Charge Injection Properties of Conjugated Polymers and Fullerenes in OPVs 15

1.6. Dissertation Overview 17

1.6.1. Chapter II. Polyelectrolyte-Mediated Electrochemical Fabrication of a Polyacetylene p-n Junction 17

1.6.2. Chapter III. Ionic Functionality and the Polyacetylene-Oxygen Charge-Transfer Complex 18

1.6.3. Chapter IV. Ionic Stabilization of the Polythiophene-Oxygen Charge-Transfer Complex 18

1.6.4. Chapter V. Increased Performance of Inverted Organic Photovoltaic Cells using a Cationically Functionalized Fullerene Interfacial Layer. 19

1.6.5. Chapter VI. Solution Phase n-doping of C_{60} and PCBM using Tetrabutylammonium Fluoride 20

1.6.6. Chapter VII. Concluding Summary 20

Chapter Page

II. POLYELECTROLYTE-MEDIATED ELECTROCHEMICAL FABRICATION OF A POLYACETYLENE p-n JUNCTION 21

2.1. Introduction 21

2.2. Experimental Methods 24

2.2.1. Materials 24

2.2.2. Device Fabrication 25

2.2.3. p-n Junction Formation 26

2.2.4. Instrumentation and Characterization 26

2.3. Results and Discussion 27

2.4. Conclusions 38

2.5. Bridge to Chapter III 39

III. IONIC FUNCTIONALITY AND THE POLYACETYLENE-OXYGEN CHARGE-TRANSFER COMPLEX 40

3.1. Introduction 40

3.2. Experimental 42

3.3. Results 43

3.4. Discussion 50

3.5. Conclusion 52

3.6. Bridge to Chapter IV 53

Chapter Page

IV. IONIC STABILIZATION OF THE POLYTHIOPHENE-OXYGEN CHARGE-TRANSFER COMPLEX 54

4.1. Experimental Methods 65

4.2. Bridge to Chapter V 66

V. INCREASED PERFORMANCE OF INVERTED ORGANIC PHOTOVOLTAIC CELLS USING A CATIONICALLY FUNCTIONALIZED FULLERENE INTERFACIAL LAYER 67

5.1. Introduction 67

5.2. Experimental 69

5.2.1 Synthesis of N,N,N-trimethyl-5-(N-methyl-3,4-[60]fulleropyrrolidin -2-yl)pentan-1-aminium bromide (NMFP-Br) 69

5.2.2 Device Fabrication 71

5.2.3 Measurements 71

5.3. Results and Discussion 72

5.4. Conclusion 77

5.5. Bridge to Chapter VI 78

VI. SOLUTION PHASE n-DOPING OF C_{60} AND PCBM USING TETRABUTYLAMMONIUM FLUORIDE 79

6.1. Conclusions 88

Chapter Page

VII. CONCLUDING SUMMARY 90

APPENDICES 93

A. SUPPORTING INFORMATION TO CHAPTER III 93

B. SUPPORTING INFORMATION TO CHAPTER IV 98

C. SUPPORTING INFORMATION TO CHAPTER VI 109

REFERENCES CITED 114

LIST OF FIGURES

Figure Page

1.1 Structure of conventional OPV 4

1.2 Chemical structures and energy levels of P3HT:PCBM active layer 5

1.3 OPV J-V characteristics under illumination 6

2.1 Schematic for doping of a conjugated polymer p-n junction 23

2.2. Schematic of PMEC fabrication of a polyacetylene-based p-n junction 28

2.3. J-V_{app} behavior of a dry bilayer p-n junction 30

2.4. Absorption spectra of a bilayer undoped and after doping sequence 32

2.5. UV-vis absorption changes at 800nm of PA_c monolayer 33

2.6. EQCM results for a thick film of PA_c 35

2.7. J-V_{app} data for three fabricated PMEC p-n junctions 36

3.1. Change in absorbance of $TMAPA_A$ before and after ion exchange 44

3.2. FTIR of $TMAPA_A$ film as deposited and following Na^+ exchange 45

3.3 Normalized absorbance of thin films of PA_{TMS}, $TMAPA_A$, and $NaPA_A$, exposed to photo-oxidative conditions 47

3.4. Patterned ion exchange immediately after exchange and after ~3 days 48

3.5. Normalized absorbance of aqueous solutions of $TMAPA_A$ and $NaPA_A$ 49

4.1. Normalized absorbance of thin films of LiPT, NaPT, KPT, and TMAPT exposed to photooxidative conditions 57

4.2. UV-vis spectra of initial photooxidation of LiPT and TMAPT under oxygen at 90% and 60% relative humidity 58

4.3. Initial and final FTIR spectra of TMAPT film under oxygen at 90% relative humidity 59

Figure Page

4.4. Difference FTIR spectra of LiPT and KPT films photooxidized under oxygen at 90% relative humidity 61

5.1. Architecture of inverted device and chemical structure of NMFP-Br 72

5.2. J-V curves of devices under AM 1.5G illumination 73

5.3. External quantum efficiencies of i-OPVs with interlayer and no n-IFL 73

5.4. Dark J-V curves for devices containing NMFP-Br and no n-IFL 75

5.5. Conductivity as a function of annealing time at 120°C 77

6.1. Spectra of C_{60} solutions with TBAF 82

6.2. Time progression of C_{60} reaction solutions with 1eq and 6eq TBAF 83

6.3. Cyclic voltammetry of C_{60} with 0eq, 1.3eq, 5eq, and 10eq TBAF 84

6.4. Spectrum of PCBM / TBAF reaction solution 86

6.5. FTIR spectra of PCBM film and PCBM / TBAF crude product film 88

LIST OF TABLES

Table Page

5.1. Summary of device properties with different n-IFL thicknesses..... 74

LIST OF SCHEMES

Scheme Page

3.1. Generalized oxidation mechanism of polyacetylene 42

3.2. CTC stabilization by sodium ion migration..... 51

4.1. Chemical structure of poly(6-(3-2,2'-bithienyl)-hexanesulfonate) 56

6.1. Proposed reaction scheme for reaction of F^- and C_{60}..... 81

CHAPTER I

GENERAL INTRODUCTION

1.1. Dissertation Goal and Objectives

The goal of this dissertation is to demonstrate the role of ionic functionality on the charge injection processes in conjugated polymers and fullerenes. Conjugated polymers and fullerenes have received considerable research interest over the last few decades for potential applications in organic electronic devices such as organic light-emitting devices,[1] organic field-effect transistors,[2] sensors,[3] and organic photovoltaics (OPVs).[4-8] This latter field of research has witnessed considerable gains in just the last few years with OPV power conversion efficiencies progressing from ~ 5% in 2006 to over 10% in 2013 for single junction devices, and from ~2.5% to ~11% for tandem cells.[9-11] This same time has also seen the initial commercial deployment of organic light-emitting devices to the marketplace.[6]

While significant scientific understanding of the fundamental chemistry and physics of these materials has been achieved over the last few decades,[12,13] the recent surge in high efficiency devices with new device architectures and materials presents considerable knowledge gaps which must be addressed to further the understanding of these materials toward the rational design of high efficiency, long-lifetime devices.

Ionically functionalized conjugated polymers, also known as conjugated polyelectrolytes (CPEs), and ionically functionalized fullerenes (IFFs), though structurally and electronically similar to their non-ionic analogues, have been shown to have significant effects on the physics of organic electronic device operation such as in OPVs.[14-18] This dissertation aims to provide insight into the fundamental chemistry associated with charge injection processes in these materials in three principle areas of study with the following objective questions to be addressed:

1. Electrochemical charge injection - Can ionic functionality be used to control the electrochemical charge injection (doping) chemistry and spatial dopant distribution in bilayer heterostructures composed of anionically and cationically functionalized polymer layers?
2. Chemical charge injection - How does ionic functionality affect chemical charge injection processes in conjugated polymers, specifically with respect to charge transfer and subsequent chemical reactions with molecular oxygen?
3. Interfacial charge injection - How does ionic functionality affect the interfacial charge injection properties of a functional OPV utilizing a cationically functionalized fullerene interlayer?

The following sections will highlight the significance of these objectives with emphasis on the use of CPEs and IFFs in organic photovoltaics as well as a brief background in each area. While there are numerous potential applications in which CPEs can be utilized, the field of OPV research has seen a significant surge in the utilization of

CPEs in high efficiency devices. While the demonstration of improvements in device performance is important, many of the underlying chemical and physical processes at work in these devices remains uncertain, particularly with respect to the role of ionic functionality. To allow for a contextual understanding, a brief basic overview of organic photovoltaic devices is first presented. This OPV description is not intended to serve as a comprehensive analysis of the state of OPV physics and chemistry, but rather to introduce basic terms and concepts which will be referred to in subsequent chapters.

1.2. Organic Photovoltaic Cell Basics

1.2.1. Charge Photogeneration

The recent interest in organic photovoltaic cells is due to their light weight, low cost, solution processablity, flexibility, and the synthetic versatility with respect to the constituent materials.[4-8] Although similar to traditional silicon based solar cells in that electromagnetic radiation is converted to electricity, the mechanism by which electronic charge carriers are generated differs significantly. The OPV photoactive layer is composed of a bicontinuous, interpenetrating network of a donor and acceptor phases (a bulk hetero junction, BHJ) which is sandwiched between two electrodes.[5] The polarity of these electrodes is determined by their relative work functions. In the conventional geometry (Figure 1.1), the hole collecting electrode (anode) is a high work function transparent conducting oxide such as indium tin oxide (ITO), often modified with an interfacial layer such as PEDOT:PSS. The electron collecting electrode (cathode) is a

low work function metal such as aluminum. Conversely, the inverted cell geometry uses a interfacial layer to lower the ITO work function (i.e. via dipole interactions or using a n-doped material) resulting in the ITO serving as the cathode. Likewise a high work function metal such as gold or silver serves as the anode.

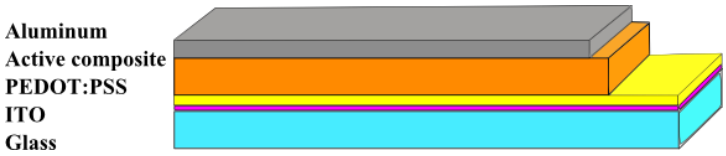

Figure 1.1. General structure of a conventional OPV. The active composite is composed of a blend of donor and acceptor species which phase segregates into the bicontinuous network or bulk heterojunction.

The materials utilized in OPVs for the donor and acceptor phases vary wildly from small molecule and polymeric donors and acceptors to hybrid systems composed of inorganic nanoparticles and fullerenes.[19,20] The most commonly employed, and highest efficiency, photoactive layers are composed of a conjugated polymer donors, such as poly(3-hexylthiophene) (P3HT) and fullerene acceptors such as 6,6-phenyl C_{61} butyric acid methyl ester (PCBM). Figure 1.2 shows the chemical structures and relative energy level positions. Upon absorption of light by the donor polymer, an electron-hole pair, or exciton, is generated. This coulombically bound pair diffuses randomly until it reaches the interface between the donor and acceptor phases (the D-A interface). At the D-A interface, the LUMO level offset between the donor and acceptor serves as the driving force for charge transfer to the acceptor phase, however, due to the low dielectric constant of organic materials, the electron and hole are still bound in a charge transfer state.[21] The pair is eventually separated thermally or by the influence of the built-in

voltage (V_{bi}) across the device which results from the difference in work functions of the two electrode contacts. Once separated, the charges migrate to the charge collecting electrodes under the influence of the built-in electric field until they are extracted. While simple, single particle descriptions of the charge photogeneration process, such as that presented, are effective to visualize the fundamental processes occurring in OPVs, it does not convey the complexity of an actual photovoltaic device.

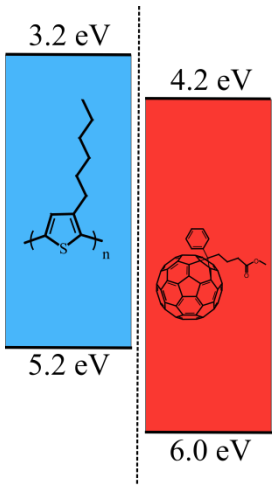

Figure 1.2. Chemical structures and energy levels of a P3HT:PCBM active layer reported relative to vacuum.

The device parameters used to determine a cell power conversion efficiency (η) are the same as those for inorganic solar cells.[22] Equation 1.1 shows the calculation used to determine power conversion efficiency.

$$\eta = \frac{V_{oc} \times J_{SC} \times FF}{I_{in}} \qquad \text{(eqn 1.1)}$$

Where V_{oc} is the open-circuit voltage, J_{sc} is the short-circuit current density, FF is the fill factor, and I_{in} is the incident light intensity. The determination of these parameters is accomplished by recording the cell current-voltage properties while under illumination (Figure 1.3). The standard light intensity utilized for these measurements is 100 mW/cm^2. These origin of these device parameters are discussed below.

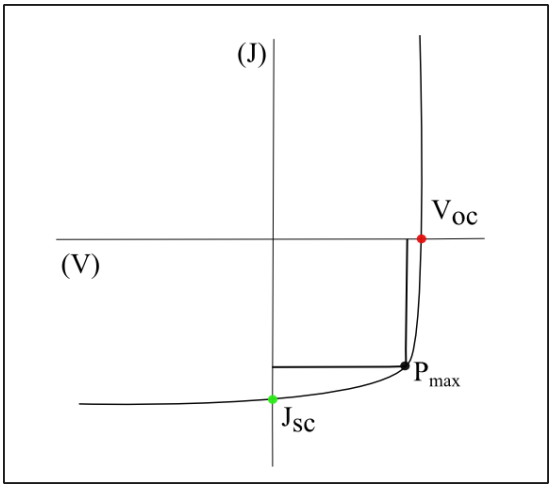

Figure 1.3. Illustration of OPV J-V characteristics under illumination and the positions of the V_{oc} (●), J_{sc} (●), and maximum power point (●, utilized for the determination of FF).

1.2.2. Open-Circuit Voltage

The V_{oc} is the difference in electrochemical potential which develops across the cell under illumination at zero current. More specifically it is the difference between the quasi Fermi levels for holes and electrons under illumination at open-circuit conditions (i.e. J = 0).[23,24] Given that the quasi Fermi levels for holes and electrons must converge at

the electrodes, to maximize V_{oc} it is important to match the work function of the electrodes with the HOMO / LUMO levels of the donor and acceptor respectively.[25] In OPVs, the maximum achievable V_{oc} for a given donor / acceptor combination is the difference between the donor HOMO and acceptor LUMO level assuming the device has ohmic contacts.[22] However, this maximum limit is seldom achieved due to a variety of reasons. Typical V_{oc}'s of highly optimized P3HT:PCBM devices are ~0.3-0.4 eV below this maximum. While numerous material and processing factors lead to reductions in V_{oc}, it is the temperature dependence of the quasi fermi level which results in what has been termed the "missing 0.3 eV."[26] Other factors which affect the V_{oc} are the voltage loss associated with the charge transfer state, trap states within the bulk which serve as recombination centers, poor alignment between the active layer HOMO / LUMO levels and electrode work functions, and interface recombination to name a few.[27]

1.2.3. Short-Circuit Current Density

The short-circuit current density (J_{sc}) is a measure of the ability of the photogenerated charge carriers to transit the active layer and be extracted by the appropriate electrodes.[22,23] Following separation of electron and holes via the charge transfer state, the charge carriers migrate to their respective electrodes under the influence of the built-in electric field. Thus the amount of charge that reaches and electrode will be dependent upon the charge transport properties of the given phase, such as the charge carrier mobility. Most organic semiconductors, such as conjugated polymers, have rather low mobility values (~10^{-3} - 10^{-4} cm^2 V^{-1} s^{-1} for P3HT hole

mobility).[28] These values are further reduced due to the disorder introduced via the interpenetrating BHJ matrix.[5] To alleviate this shortcoming, processing steps such as thermal or solvent annealing are utilized to increase the crystallinity of the donor and acceptor phases.[5,21] The value of the J_{sc} is also affected by recombination centers such as those due to impurities, defect sites induced by oxidation, as well as resistances associated with the electrode / active layer interface.[22]

1.2.4. Fill Factor

The fill factor in is defined as the ratio of the maximum cell power to the theoretical maximum, which is the product of V_{oc} and J_{sc} (eqn 1.2). The fill factor reflects the diode quality of the cell.[22,29]

$$FF = \frac{V_{mmp} \times J_{mmp}}{V_{OC} \times Jsc} \qquad \text{(eqn 1.2)}$$

Where J_{mmp} is the current at the maximum power point, V_{mmp} is the voltage at the maximum power point. The primary parameters which affect FF are the series and parallel resistances (R_s and R_p respectively). R_s is a measure of the resistances associated with the active layer / electrode contacts. For efficient cell operation it is desired that R_s be small. Increased interfacial resistance will also deleteriously affect J_{sc}, although Voc is typically not affected. The presence of energy barriers at the active layer / electrode interface, interfacial degradation due to photooxidation, and low conductivity of interfacial modification layers are common causes of increased series resistance.[22] R_p is a

measure of the cell shunt resistances due to leakage currents between the two electrodes. Such leakage can be the result of the direct connection via the donor or acceptor phase, micro-shorts resulting from small amounts of the top metal electrode coming in contact with the bottom electrode, as well inhomogeneities in active layer thickness. As opposed to the case with R_s, an infinite R_p is desired. In the case of a small R_p, a decrease in V_{oc} is typically seen, with little change in J_{sc}.[22,29]

1.3. Electrochemical Charge Injection in Conjugated Polymers and CPEs

The use of conjugated polymers in organic electronic devices is due to their unique chemical structure, specifically the series of alternating double and single bonds. This conjugation is due to the overlap of p-orbitals along the polymer backbone which facilitates the movement of electronic charge, either electrons or holes, along the length of the molecule. This delocalization of the electronic orbital results in the formation of an electronic "band-like" structure analogous to that seen in inorganic semiconductors.[13] The overlap of occupied and unoccupied orbitals leads to the formation of a valence and conduction band, respectively. The separation between band edges, or bandgap, is determined by the polymer structure. This bandgap determines the optical transition energy which plays a fundamental role in photogeneration of charge carriers in OPVs. In their neutral state conjugated polymers are insulating as a result of the bandgap, however, upon introduction of excess charge, conductivities in the semiconducting ($\sim 10^{-8}$ - 1 S / cm) to metallic range (~ 1 - 10^4 S / cm) can be realized.[30]

The introduction of electronic charge carriers into conjugated polymers can be readily accomplished using traditional electrochemical methods.[13] Most often in the study of these materials, polymer films are immobilized on an electrode and subjected to electrochemical characterization rather than using the solution phase molecule, as the diffusion of the macromolecular polymer molecule in solution is slow. The introduction of an electron (n-doping) or the introduction of a hole (p-doping) into the polymer film must be accompanied by introduction of a corresponding counterion from the solution phase electrolyte in order to maintain charge neutrality.[13,31] The electrochemical doping process of conjugated polymers differs from the doping of inorganic semiconductors in that the introduced electronic charge remains localized over a segment of the polymer backbone rather than delocalized over the bulk.[31] This localization is a consequence of the nature of the conjugated polymer molecule. Upon application of a suitable electrode potential (determined by the electronic structure of the particular polymer), an electron is removed (in the case of p-doping) from the polymer backbone via heterogeneous charge transfer at the polymer / electrode interface. Concomitant with ionization is an introduction of a solution phase anion to maintain charge neutrality. Due to the difference in geometry between the ionized and neutral polymer, it is energetically favorable for the molecule to undergo a structural deformation. This deformation results in localization (over 12-15 CH units in polyacetylene for example) of the introduced hole due to strong phonon-charge coupling in these materials.[32] This structural alteration and coupling results in the formation of new energy states within the bandgap, the energy and density of which is dependant upon the structure of the polymer and the level of doping. At higher levels of doping, these discrete states converge into 'band-like' sub bandgap

states. The presence of inter-bandgap energy states has implications for the absorption and emission properties of these materials, as the new energy states allow for optical transitions at energies less than that of the bandgap. These characteristic absorptions are commonly utilized as diagnostic signatures of the doping process.[13] The energy of these transitions is characteristic to specific polymers based on their electronic structure. These absorptions can also be used to determine the dopant density in electrochemically doped polymer films.

While CPEs share a similar electronic structure as their non-ionic analogues, such as bandgap energies and band edge energies (HOMO / LUMO levels), it is the presence of the bound ionic group and associated counterion which differs. Opposed to the case of the conventional conjugated polymer, upon electrochemical doping, CPEs can expel their counterion to solution rather than a solution phase ion being introduced. In the case of p-doping, an anionically functionalized CPE would expel a cation upon injection of a hole from the electrode. This results in the hole being compensated by the bound anion. This is often referred to as an internally compensated state and the process is sometimes referred to in the literature as 'self-doping' (although the name is misleading as charge must still be introduced).[33] This ability to expel the counterion from the film is beneficial for devices fabricated using conjugated polymers as the presence of mobile ions can have numerous deleterious effects for a given application. For example, mobile ion polarization causes a redistribution of the internal electric field across the device.[1,33] While this may be beneficial in devices such as polymer light-emitting electrochemical cells, it is deleterious in devices such as OPVs. Likewise, the presence of excess charge carriers and ions in the photoactive layer results in exciton quenching and reduced charge

photogeneration.[34] However, if the doped region can be isolated to specific regions of the device, such as the active layer / electrode interface, the benefits of the doped materials can be realized without altering charge photogeneration in the bulk. Such use of doped interfacial layers has been demonstrated using conjugated polymers such as PEDOT:PSS.[4-8,35] Evaporation of LiF as an electron selective layer between the bulk active layer and aluminum cathode in conventional OPVs is another common technique which has been suggested to result in interfacial n-doping.[36] The use of CPEs doped electrochemically to their conducting state provides another method to control interface energetics and charge extraction properties without the introduction of unwanted ions. As has been show in the literature, the electrode work function can be systematically controlled via the electrochemical doping of a polymeric or fullerene interfacial layer.[35,37] This control of the electrode work function, via the fermi level of the interfacial material, has a direct influence on the cell open-circuit voltage. However, the necessity to introduce mobile counterions has a deleterious effect on charge extraction and overall cell performance for some of the reason mentioned above. Thus, the use of CPEs as interfacial layers may allow for a similar control of electrode energetics without the unwanted inclusion of mobile ionic species. The internal compensation afforded by CPEs also allows for the control of doping density via synthetic control of the density of ionic groups bound to the polymer. As demonstrated in Chapter II, this allows for manipulation and control of device electronic properties through control of doping density.

1.4. Chemical Charge Injection in Conjugated Polymers and CPEs

The use of chemical species to dope conjugated polymers to a conducting state has been extensively studied over the years.[13] A common p-dopant is I_2, which upon oxidation of the polymer, serves as the balancing counterion in the form of I_3^- or I_5^- as well as other proposed polyatomic species.[38] A more common, unwanted, p-type dopant in conjugated polymers is molecular oxygen. However, as opposed to the case of I_2 doping to produce a stable conducting p-doped polymer, doping by oxygen is typically followed rapidly by chemical reactions between the polymer and oxygen which irreversible disrupts the conjugated structure of the molecule.[39-43] This disruption significantly degrades the electronic and optical properties of the polymer or device. It is this chemical reactivity between conjugated polymers (and fullerenes) and oxygen which has inhibited the commercial viability of OPVs fabricated using these materials.[44] Relative to studies on the electronic and electrochemical properties of conjugated polymers and OPVs, studies on the mechanism of polymer oxidation and photooxidation are relatively limited.

The oxidation of several conjugated polymers utilized in OPVs have been reported and all follow a similar general reaction scheme.[39-43] The oxidation of these materials is typically sensitive to light exposure (photooxidation) and depends on the particular material. For example, polyacetylene and poly(phenylene vinylene) will readily oxidize upon exposure to air in the dark, whereas polythiophene derivatives require exposure to light and oxygen.[45,46] In both cases the general scheme initiates with

the adsorption of oxygen on the polymer to form a charge-transfer complex (CTC) and results in partial p-doping of the polymer. The extent of charge transfer can vary from a partial sharing of electron density to full electron transfer to generate the contact ion pair. This process is typically reversible if the oxygen is removed (such as via vacuum) within a short period of time.[39,40] If removal of oxygen does not occur, follow-on chemical reactions proceed through a variety of mechanisms, most often through the formation of unstable peroxide species which give rise to free radicals such as •OH.[43] These species, in turn, react with and disrupt the conjugation of the polymer resulting in bleaching of the optical absorbance and degradation of electronic properties. Under photooxidative conditions, other mechanisms can proceed such as photosensitization of singlet oxygen ($^1O_2$) via the triplet excited state of the polymer.[47] This high energy form of oxygen then reacts with the conjugated backbone, again often leading to the formation of unstable peroxides and radicals. Photoinduced electron transfer to molecular oxygen to produce superoxide (O_2^-) has also been reported and is sensitive to the hydration of the oxygen molecule.[48] O_2^- is known as a highly reactive oxygen species.

As opposed to oxidation studies of non-ionic conjugated polymers, very little is reported with regard to the oxidative stability of CPEs, with the exceptions often being ancillary to the focus of the report.[49,50] Given the surge in the use of CPEs in functional devices, further study of the effect of ionic functionality on this charge injection process (hole injection from oxygen) is necessary. Such studies are also useful for the understanding of oxidation processes in non-ionic conjugated polymers as many of the initial products (i.e. the polymer-O2 CTC) are, at least partially, ionic in nature.[51] Chapters III and IV demonstrate the significant effect of ionic functionality on the initial

charge injection event, as well as subsequent reaction pathways and products. The understanding of charge injection processes between molecular oxygen and conjugated polymers is also highly relevant to the study of oxygen reduction reactions toward such applications as fuel cells in which efficient oxygen reduction plays a key role.

1.5. Interfacial Charge Injection Properties of Conjugated Polymers and Fullerenes in OPVs

The injection or extraction of charges across interfaces is central to any functional electronic device, with organic based devices being no exception. Such interfaces in OPVs may be organic / organic interfaces, such as at the donor / acceptor interface, or metal / organic such as at the charge collecting electrodes. As opposed to the types of charge injection mentioned in the previous two sections, interfacial charge injection does not occur with the inclusion (or expulsion) of a charge compensating counterions.[13] However, charge neutrality must be maintained and is done so, typically, via injection of charge of the opposite sign at the second electrode interface.[22] Other charge compensation mechanisms, such as capacitive charging, have also been demonstrated.[52] In OPVs, efficient, balanced extraction of photogenerated charge carriers is essential to achieving high efficiency, specifically by increasing the short-circuit current (J_{sc}) and fill factor (FF).[22, 29] Imbalanced extraction of charge carriers, such as due to an energy barrier at one of the electrodes, can result in the accumulation of space-charge which inhibits further charge extraction and decreases the overall J_{sc}. This can also often manifests as an S-shaped kink in the J-V curve which severely decreases the FF.[29] Large

series resistances at the charge collecting interfaces also result in FF decrease.[22,29] To address these issues, judicious selection of electrode materials to allow for an energetically downhill process is employed, however, this often results in a decrease of the cell V_{oc} due to the reduction of the cell built-in voltage.[23,24]

To address such concerns, charge selective interfacial layers are often deposited between the active layer and the charge collecting electrodes.[14] Such layers affect charge extraction by being selective to one sign of charge carrier, thus reducing recombination at the electrode interface and maximizing V_{oc} and J_{sc}. These materials can also be used to modify the electrode work function via dipole interactions, integer charge-transfer processes, or intentional doping, again maximizing V_{oc}.[35,37,53] The impact of interfacial resistance can be addressed via the use of highly conducting interface layers, such as PEDOT:PSS, or by controlling interlayer thickness.[18]

Recently, the use of CPEs has attracted significant interest for use as electron selective interfacial layers, with devices incorporating such materials achieving some of the highest power conversion efficiencies reported.[14-18] Many of the reported CPEs used as electron selective interfacial layers are based on the wide bandgap polyfluorene backbone.[18] The enhancement in cell efficiency in these devices is largely the result of an increase in V_{oc}, most often attributed to dipole orientation. However, due to the insulating nature of polyfluorene, very thin layers must be utilized to prevent the reduction in J_{sc} and FF due to series resistance. Polyfluorene also does not provide for alignment of LUMO levels with most acceptor molecules, such as PCBM, which can inhibit charge extraction. To address such issues, numerous groups have utilized fullerene based electron selective interlayers which provide for effective energy level

alignment with PCBM as well as provide another interface for exciton dissociation.[54-56] To reduce series resistance, chemical n-doping of these layers has been reported using such dopants as decamethylcobaltacene or alkali carbonates.[55,56] The use of ionically functionalized fullerenes as interfacial layers has received relatively little attention until recently. Jen et al. has demonstrated the unusual high conductivity of thin films of a cationic fulleropyrrolidinium derivative and suggested such conductivity is the result of charge transfer from the counter anion.[57] The use of ionically functionalized fullerenes is particularly attractive as presence of dipole interactions as well as orbital overlap with the fullerene acceptor and high conductivity can simultaneously increase the V_{oc} as well as maximizing the FF and J_{sc}. The application of a cationically functionalized fullerene derivative is demonstrated in Chapter V. The highly conductive nature of this material is demonstrated and explored further in Chapter VI using the model system of C_{60} and tetrabutylammonium fluoride.

1.6. Dissertation Overview

1.6.1. Chapter II. Polyelectrolyte-Mediated Electrochemical Fabrication of a Polyacetylene p-n Junction

This chapter will demonstrate the effect of ionic functionality on electrochemical charge injection processes in a bilayer structures of anioncally and cationically functionalized polyacetylene. Polyelectrolyte-mediated electrochemistry is utilized to selectively dope n- and p-type regions to fabricate an organic p-n junction. This chapter

is based on coauthored, published work: Robinson, S. G.; Weber, C. D.; Johnson, D. H.; Lonergan, M. C.; *Chemistry of Materials*, **2010,** 22, 241-246. My contributions to this work include electrochemical measurements, EQCM analysis, device fabrication, as well as participation in the determination and proposal of the electrochemical doping scheme presented.

1.6.2. Chapter III. Ionic Functionality and the Polyacetylene-Oxygen Charge-Transfer Complex

This chapter demonstrates the role of ionic functionality with respect to chemical charge injection from molecular oxygen in anionically functionalized polyacetylene thin films. The work illustrates the substantial effect of ionic functionality on the rate of photooxidation of polyacetylene thin films as well as the specific role of the counter cation. This chapter is based on coauthored, published work: Weber, C. D.; Robinson, S. G.; Lonergan, M. C.; *Macromolecules*, **2011,** 44, 4600-4604. The experimental design, data collection, and analysis was performed by myself with assistance from Steven Robinson in polymer synthesis and creation of the "O" image (Figure 3.4).

1.6.3. Chapter IV. Ionic Stabilization of the Polythiophene-Oxygen Charge-Transfer Complex

This chapter further explores the work presented in Chapter III using anionically functionalized polythiophene thin films with counter cations of varying charge density.

The work demonstrates the effect of ionic functionality on the chemical charge injection process from molecular oxygen using a more widely utilized conjugated polymer, polythiophene, and demonstrates control of chemical reaction pathways through the ionic stabilization of reaction intermediates. The chapter is based on coauthored, published work: Weber, C. D.; Robinson, S. G.; Stay, D. P.; Vonnegut, C. L.; Lonergan, M. C.; *ACS Macro Letters*, **2012,** 1, 499-503. Experimental design, data collection and analysis was performed by myself with assistance from Stephen Robinson and Chris Vonnegut (polymer synthesis and characterization) and David Stay (GPC analysis).

1.6.4. Chapter V. Increased Performance of Inverted Organic Photovoltaic Cells Using a Cationically Functionalized Fullerene Interfacial Layer

This chapter demonstrates the effect of ionic functionality on interfacial charge injection processes in a functional OPV. The work will show that an increase in cell open-circuit voltage and decrease in series resistance (resulting in an increase in overall performance) is likely the result of the decrease of the electrode work function due to the n-type nature of the NMFP-Br interlayer. The effects on interfacial charge transfer are discussed with respect to the highly conductive nature of the interfacial layer. This chapter is based on coauthored, unpublished results. The experimental design, device fabrication, data collection and analysis were performed by myself with assistance from Stephen Robinson (fullerene synthesis and characterization), Ethan Walker (EQE measurements) and Colin Bradley (conductivity measurements).

1.6.5. Chapter VI. Solution Phase n-doping of C_{60} and PCBM Using Tetrabutylammonium Fluoride

This chapter will expand upon the work of Chapter V by exploring the possible source of the unusual high conductivity of NMFP-Br films. The reaction between tetrabutylammonium fluoride (TBAF) and C_{60} is used as a model system to show the presence of chemical reactions which give rise to subsequent electron transfer events and fullerene n-doping. The analogous experiments using PCBM are also explored and show unique chemical reactivity with respect to the reaction with TBAF. This chapter is based on coauthored, published work: *J. Mater. Chem A.*, accepted manuscript, DOI: 10.1039/c3ta14132b. The experimental design, data collection and analysis was performed by myself with assistance from Colin Bradley (NMR).

1.6.6. Chapter VII. Concluding Summary

This chapter provides a general conclusion and highlights the result reported in this dissertation with respect to the objective question outlined in section 1.1.

CHAPTER II

POLYELECTROLYTE-MEDIATED ELECTROCHEMICAL FABRICATION OF A POLYACETYLENE p-n JUNCTION

2.1. Introduction

Junctions such as the p-n junction where there exists a discontinuity in dopant type or density are ubiquitous in silicon-based electronics,[1] but examples of such junctions are far less common with conjugated polymers. One important reason is the instability created by the mobile dopant ions that are typically present in doped conjugated polymers. In the case of a p-n junction, for instance, any diffusible dopant ions will support a bulk redox reaction between the n- and p-type regions that destroys the junction (reverse reaction of Figure 2.1A).[2]

A number of trapping approaches have been developed to overcome the problem of dopant-ion diffusion. These approaches rely on the application of an electrical bias across an ion-containing sample to drive redox disproportionation, thus forming n- and p-type regions at the electrodes (forward reaction in Figure 2.1A). The otherwise transient

junction is then trapped by reducing the temperature to freeze out the ions,[3-6] by using ion-pair monomers that are polymerized to reduce their mobility,[7,8] or by using ion-functionalized conjugated polymers (conjugated ionomers[9,10] or conjugated polyelectrolytes[11]), which allow the ions liberated in the disproportionation step to be removed by solvent washing (forward reaction of Figure 2.1B).[12] A key limitation of the above trapping approaches is that the doping of the two regions is coupled because they are two-electrode techniques. Oxidation at one electrode to form the p-type region is coupled to reduction at the other electrode to form the n-type region. Methods by which the n- and p-doped regions are created independently would provide for the creation of structures that are not possible with current trapping approaches. The goal of this paper is to demonstrate polyelectrolyte-mediated electrochemistry (PMEC) as a three-electrode method for separately introducing n- and p-type regions in the fabrication of a conjugated polymer p-n junction.

In the PMEC approach, doping is controlled by manipulating the counter-ions available to support electrochemical doping. The availability of counter-ions is controlled by using a combination of ion-functionalized conjugated polymers with different signs of exchangeable counter ions *and* a supporting electrolyte based on a large polymeric ion. Elliott and co-workers showed in the context of redox polymer films that the electrochemistry of a solid film can be controlled by using a polyelectrolyte-based supporting electrolyte.[13] In their work, redox processes that required the incorporation of the polymeric ion for charge compensation were suppressed.

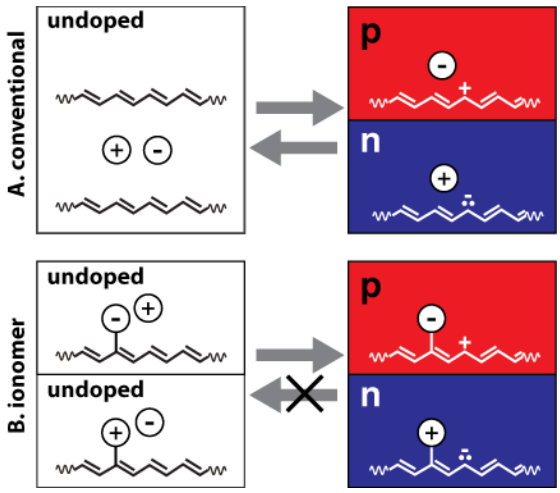

Figure 2.1. (A) Schematic for the doping (forward reaction) of a conventional conjugated polymer with dissolved salt to form a conjugated polymer p-n junction and undoping (reverse reaction) of a conjugated polymer p-n junction to form an undoped polymer and salt. The reverse reaction illustrates the instability of conjugated polymer p-n junctions containing mobile dopant counter ions. The forward reaction can be achieved, for example, by applying an electrical bias across the sample to drive redox disproportionation, but without a means of altering the mobility of the ions after doping, the resulting junction is unstable with respect to redox comproportionation (reverse reaction) after removal of the bias. (B) Schematic for the doping (forward reaction) of a bilayer structure consisting of anionic and cationic ion-functionalized conjugated polymers, with the loss of exchangeable ions, to form a conjugated polymer p-n junction. The resulting p-n junction is stabilized with respect to the reverse reaction because the dopant counter-ions are covalently bound to the polymer backbone.

In the electrochemical doping of a structure to form a p-n junction, the key is not simply to suppress all redox processes of one type (oxidation or reduction), but rather, to selectively oxidize or reduce certain regions. Herein, we demonstrate that this selective redox chemistry is possible by exploiting a combination of a polyelectrolyte-based supporting electrolyte and ion-functionalized conjugated polymers to fabricate a p-n junction. By building ions into the redox active solid film (i.e. using ion-functionalized conjugated polymers), redox processes that would otherwise be inhibited by the polyelectrolyte-based supporting electrolyte can be selectively restored.

Implicit to the PMEC approach is that the resulting p-n junction will be stabilized against reaction between the n- and p-type regions because it is based on ion-functionalized conjugated polymers and designed to yield internally compensated doped forms. Internal compensation refers to the situation where the charge on the polymer backbone is compensated by counter ions covalently bound to the polymer backbone.[14,15] Such covalently bound dopant ions are expected to have low mobility and hence be unable to support redox comproportionation of the p-n junction back to the undoped state (reverse reaction in Figure 2.1B).

2.2. Experimental Methods

2.2.1. Materials

Chloroform was distilled from P_2O_5. Methanol was distilled from Mg/iodine. Anhydrous dimethylformamide (DMF) was used as received. Acetonitrile (ACN) was doubly distilled from P_2O_5. Solvents were degassed using 3 freeze-pump-thaw cycles. Tetrabutylammonium polystyrene sulfonate (Bu_4NPSS) was synthesized by neutralizing polystyrene sulfonic acid (MW 70 000, Polysciences) with tetrabutylammonium hydroxide (Aldrich) and then dialyzing for four days using Spectra/Por 4 cellulose dialysis membranes. The resulting salt was dried in vacuo for 5 days at 80^{o}C. Tetramethylammonium tetrafluoroborate ($TMABF_4$)(Aldrich) was recrystalized from water and dried in vacuo at 80^{o}C for 5 days. The anionic polymer (PA_A) was synthesized using ring opening metathesis polymerization from tetramethylammonium β-

cyclooctatetraenylethyl sulfonate as reported previously.[10] The cationic copolymer (PA_C) was synthesized from trimethylsilylcyclooctatetraene and (2-cyclooctatetraenylethyl) trimethylammonium triflate as previously described.[16] The resulting co-polymer had a ratio of 7.7:1 trimethylsilyl (TMS) to trimethylammonium functional groups as determined by NMR. The tungsten alkylidene catalyst [$W{=}CH(o\text{-}C_6H_4OMe)(NC_6H_5)$-$[OCCH_3(CF_3)_2]_2(THF)$] used in the polymerizations was synthesized as described previously.[17]

2.2.2. Device Fabrication

Junctions were fabricated from sandwich structures consisting of a bilayer containing thin films of PA_C and PA_A sandwiched between gold electrodes. These bilayers were formed by spin coating first a DMF PA_C solution (5 μL, 20 mg/mL) followed by a methanol PA_A solution (10 μL, 20 mg/mL) onto a semi-transparent Au/Cr (15 nm, 1.5 nm) film electrode on a glass slide. The PA_C layer is insoluble in methanol which prevents dissolution when the PA_A layer is placed on top. The thickness of the individual layers using this approach could be varied from 150 to 600 nm. The actual thickness of each layer was measured using a Dektak 6M stylus surface profilometer. The bilayer was carefully cleaned back to the electrode edge and a top porous Au electrode[18] (15 nm) was then deposited by thermal evaporation over a portion of the bilayer. For optical absorption experiments, the bottom electrode was omitted because the pair of electrodes created strong interference effects that complicated interpretation of the absorption spectra.

2.2.3. p-n Junction Formation

The bilayer films were soaked for 5 minutes in ACN (1 mL) under a nitrogen environment. Bu_4NPSS/ACN (0.1M, 1.5mL) was then added to the ACN. Owing to some solubility of the PA_A layer in Bu_4NPSS / CH_3CN, the bilayer was initially cycled to positive potentials. This positive cycling rendered the PA_A layer insoluble presumably due to some small degree of cross-linking reactions. The bilayer was doped by first applying a negative potential step to -1.5V vs SCE for 60s. The sample was then held at open circuit for approximately 30s followed by applying a positive potential step of 0.6V vs SCE for 60s. The solvent was removed, and the sample washed with ACN (3x5mL), dried under N_2 for 5 minutes and then dried under vacuum for 12 hours before characterization.

2.2.4. Instrumentation and Characterization

Electrochemical doping was performed with a Cypress 66-CS1200 potentiostat using a standard three-electrode cell with a coiled platinum wire counter electrode and a nonaqueous Ag (s) /Ag^+ reference electrode. The reference electrode was prepared from a 3mm diameter glass tube with a Vycor frit (Bioanalytical Systems, Inc), filled with 0.075M $TMABF_4$ / 0.005 $AgNO_3$ / ACN, and it was calibrated with a commercial saturated calomel electrode. Spectroelectrochemistry was performed using an Ocean Optics USB 2000 diode array spectrometer connected via a fiber optic cable. Spectra were referenced against blanks prepared identically to the sample structures but without

the polymer layers. Current-voltage experiments on the dried bilayers were performed using an Agilent 4156C semiconductor parameter analyzer. Photoresponse measurements were performed using 50 mW illumination from a focused tungsten-halogen EHJ white light source and the parameter analyzer. EQCM measurements were performed using a Stanford Research QCM100 with AT-cut, 5 MHz, Au/Ti crystals. The resonant frequency was monitored via a Tektronix TM5003 frequency counter interfaced with the QCM control module. Simultaneous voltammetry measurements were conducted using a Solartron 1287. Measurements were carried out in a custom designed cell under an atmosphere of dry N_2. The EQCM measurements were conducted using a Pt counter electrode, Ag wire pseudo reference, and a grounded working electrode.

2.3. Results and Discussion

The PMEC approach to fabricating a conjugated polymer p-n junction was demonstrated using ion-functionalized polyacetylenes. The undoped bilayer structure shown in Figure 2.2A was used as the starting point. The bilayer was fabricated from anionic (PA_A) and cationic (PA_C) polyacetylenes with differing ion densities. Specifically, the ionic functional group densities of PA_A and PA_C were 1 per 4 and 1 per 30 double bonds, respectively. This difference was intentional so as to demonstrate the ability of PMEC to create structures not possible using trapping approaches. Note that the structure of PA_C also incorporates trimethylsilyl (TMS) functional groups for solubility. The bilayer shown in Figure 2.2 consists of a ~450 nm thick film of PA_A and a ~350 nm thick film of PA_C.

Junctions were fabricated using two sequential potential steps applied to the top porous electrode[18] (in contact with PA_A) of the undoped bilayer of Figure 2.2A and using the supporting electrolyte tetrabutylammonium polystyrenesulfonate (Bu_4NPSS) / CH_3CN. The two steps that were used are: Step I: a 60 s potential step to -1.5 V vs. SCE; Step II: a 60 s potential step to 0.6 V vs. SCE. The -1.5 and 0.6V vs. SCE potentials are sufficient to either n- or p-dope, respectively, single layer films in a conventional electrolyte.[16] It is noted that the doping chemistry is also affected by Donnan equilibria[19] that influence the potential driving force required for doping, as we have previously studied in single layer films of polyacetylene ionomers.[20]

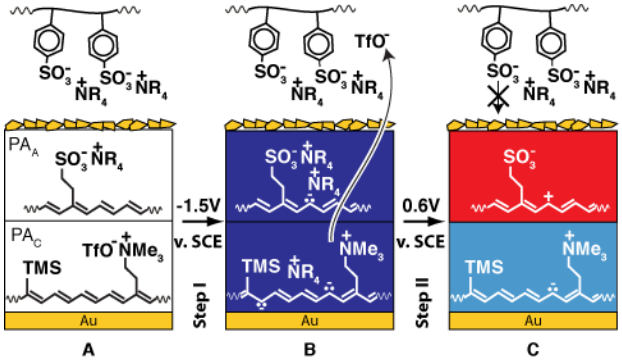

Figure 2.2. Schematic of the PMEC fabrication of a polyacetylene-based p-n junction using a Bu_4NPSS / CH_3CN supporting electrolyte. (A) Initial undoped bilayer of solid films of a polyacetylene anionomer (PA_A) and a polyacetylene cationomer (PA_C) sandwiched between gold electrodes (the top electrode in contact with PA_A is sufficiently thin so as to remain porous). (B) Structure following the application of -1.5 V vs. SCE to the top porous electode to n-dope the films. (C) Structure following the application of 0.6 V vs. SCE to the top porous electrode to p-dope the PA_A layer while preserving the PA_C layer in an IC n-type form. Complete reoxidation and p-doping of the PA_C layer is not possible because the original OTf^- anions were previously lost to the solution and PSS^- is too large to permeate the polymer film.

Our idealized picture of how the above potential step sequence yields a p-n junction is as follows. Step I n-dopes the structure as shown in Figure 2.2B. The

reduction of PA_A is supported by the incorporation of R_4N^+ ions from the electrolyte. The reduction of PA_C is supported by both such incorporation and the loss of triflate (OTf^-) anions. The result of oxidative Step II is shown in Figure 2.2C. As in conventional electrochemistry, the PA_A layer is oxidized first back to its undoped state and then to its p-type state, all supported by the expulsion of R_4N^+ ions. The reoxidation of PA_C, however, cannot fully occur. During Step I, the OTf^- anions are stripped from PA_C and lost to the electrolyte solution, much like in metal stripping. Consequently, the OTf^- anions are not available, and the PSS^- anion is too large to support the complete reoxidation of the n-type PA_C. A component of the n-type doping balanced by the loss of OTf^- anions remains, forming an internally compensated (IC) state where the density of injected charge is balanced by the covalently attached cations. The result is the selective p-doping of the PA_A layer while the PA_C layer remains n-doped.

The formation of a p-n junction was demonstrated by current density-voltage (J-V_{app}) characterization. All of the J-V_{app} data reported were collected on structures that were washed and then dried following electrochemical manipulation, and the bias was applied PA_A vs. PA_C. As shown in Figure 2.3a, diode behavior was clearly observed (solid line). Consistent with classic p-n junction theory,[1] much greater current was observed for positive bias. The J-V_{app} characteristics did not substantially depend on scan rate at least up to 100 V s^{-1}.

Figure 2.3 also shows the results of two control experiments. The dashed line shows the J-V_{app} behavior for Control 1: a bilayer subjected to only a positive potential step of 0.6 V vs SCE in Bu_4NPSS (Step II). The Control 1 sample was observed to be much less conductive than the junction subjected to the two-step electrochemical

sequence, consistent with oxidation of PA_A while preserving PA_C in its undoped or intrinsic (i) state to form a p-i junction. The PA_C remained undoped in the Control 1 sample and hence poorly conductive presumably because the PSS^- anion is too large to permeate the solid polymer film as would be required to p-dope PA_C.

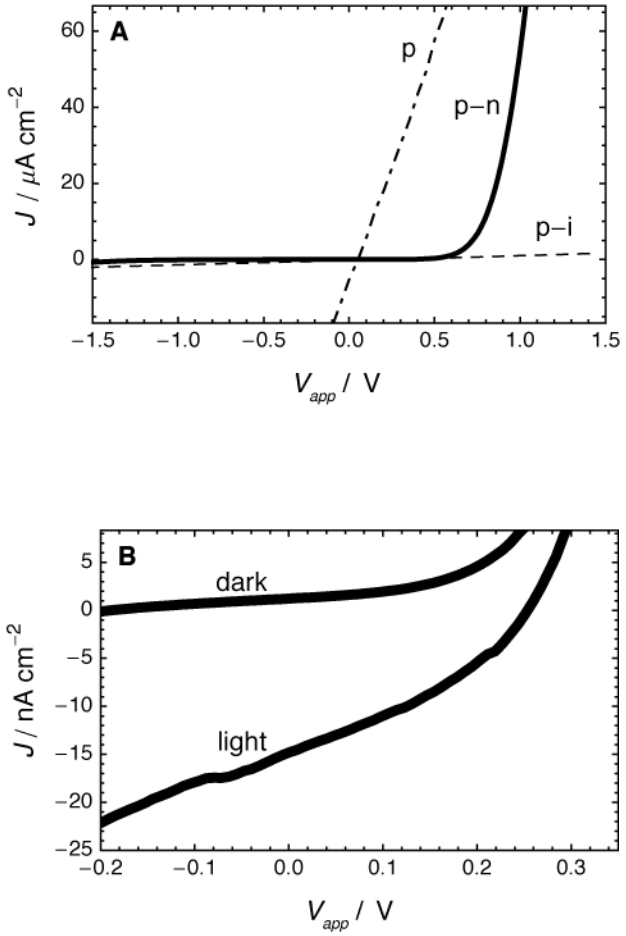

Figure 2.3. (A) Current density (J)-applied bias (V_{app}) behavior of dry PA_C / PA_A bilayers after the two step doping sequence illustrated in Figure 2.1 to form a p-n junction (solid line); Control 1 consisting of only Step II (0.6 V vs. SCE in Bu_4NPSS / CH_3CN) to form a p-i junction (dashed line); and Control 2 consisting of the same two-step doping sequence used to form the p-n junction but substituting $TMABF_4$ / CH_3CN as the electrolyte to form two p-doped layers (dot-dashed line). (B) Comparison of the J-V_{app} behavior for the same p-n junction as in part A in the dark and under illumination. The film thickness for the PA_A and PA_C layers were ~450 nm and ~350 nm thick, respectively.

The dot-dashed line shows the J-V_{app} behavior for Control 2: a bilayer subjected to the two-step electrochemical sequence used for p-n junction formation but in the conventional electrolyte tetramethylammonium tetrafluoroborate ($TMABF_4$) rather than in Bu_4NPSS. The Control 2 sample was observed to become conductive and exhibit a linear J-V_{app} relationship. The observed linearity is consistent with both layers becoming p-doped rather than p-n junction formation. Figure 2.3B expands the J-V_{app} curve and compares it to that under 50 mW illumination from a focused, tungsten-halogen, white light source. A photovoltaic effect, albeit small, was observed consistent with p-n junction formation.

Spectroelectrochemistry was also used to support p-n junction formation. An undoped bilayer was first subjected to a 60s potential step at 0.6V vs. SCE in Bu_4NPSS/CH_3CN (Step II) to provide an important reference point for later comparison. As discussed and supported with the J-V_{app} data of Control 1, this initial potential step selectively oxidizes the PA_A layer to its p-doped state while leaving the PA_C undoped to from a p-i junction. Figure 2.4 compares the absorption spectrum of the p-i junction (dashed line) with that of the undoped bilayer (dot-dashed line). As is characteristic for either the n- or p-doping of PA, the p-i junction exhibits a decrease in absorbance on the short wavelength side of the region shown (due to a bleach of the π- π *absorbance with λ_{max} = 600 nm) and an increase in absorbance on the long wavelength side (due to the tail of the broad NIR absorbance of the doped state with λ_{max} = ~1300 nm) relative to the undoped bilayer. The same bilayer that was used to fabricate the p-i reference junction was then subjected to the two-step sequence described above for p-n junction formation. The spectrum of the resulting structure is shown in Figure 2.4 (solid line), and it reveals a

higher level of doping than observed in the p-i reference. The difference between the spectra assigned to the p-i and p-n junctions illustrate that there is a memory of Step I in the latter case. This memory and the higher degree of doping are consistent with the PA_C layer remaining n-doped during Step II to form the p-n junction.

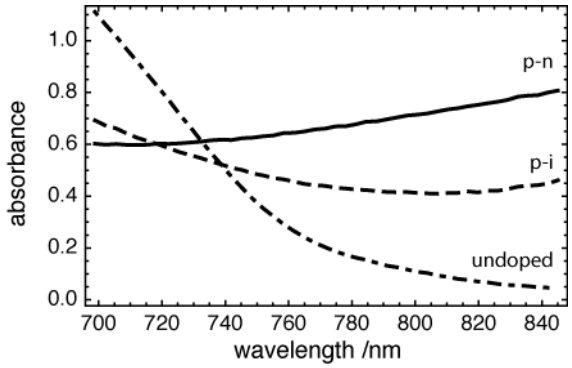

Figure 2.4. Absorption spectra of a 160 nm PA_C / 300nm PA_A bilayer in its undoped form (dot-dashed line); after only Step II (0.6 V vs. SCE in Bu_4NPSS / CH_3CN) to form a p-i junction (dashed line); and after the two step doping sequence illustrated in Figure 2.1 to form a p-n junction (solid line).

The assertion that the internally compensated n-type state of the PA_C layer does not undope in Bu_4NPSS / CH_3CN when driven to potentials that would undope or even p-dope PA_C in a conventional electrolyte is key to the formation of the p-n junction. That this is the case was demonstrated by spectroelectrochemical and electrochemical quartz crystal microbalance (EQCM) experiments on single layer PA_C films. Figure 2.5 shows the absorbance at 800 nm of a single layer PA_C film on a gold electrode while being subjected to the two-step doping protocol used to create the p-n junction, although with a slightly more negative Step I potential. The single layer PA_C film was first allowed to sit for 5 seconds to measure the undoped absorbance. A potential step of -1.6 V vs. SCE was then applied for 60s. During the -1.6 V vs. SCE potential step, the absorbance at

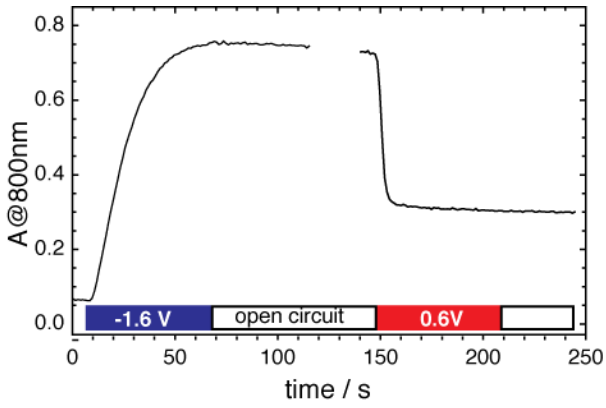

Figure 2.5. UV-vis absorption changes at 800nm of a 250nm thick PA_C monolayer cycled through the two-step doping process used for p-n junction formation. The bar at the bottom edge of the graph shows the potential vs. SCE at which the polymer was held during the experiment; the open regions indicate open circuit. The gap in the data is during a period when the software controlling the instruments was being reconfigured for the second potential step. During this gap, the cell was held at open circuit.

800nm was observed to increase and then level off. The observed increase corresponds to n-doping of the sample presumably with the loss of triflate anions and the incorporation of mobile cations from the electrolyte. After the potential step had finished, the sample was monitored at open circuit for 80s. A potential step of 0.6 V vs. SCE was then applied, and a drop in the absorbance was observed. The absorbance did not, however, return to its undoped value, but rather leveled off at an absorbance above the undoped state. This persistent absorbance supports the assertion that the film remains n-doped due to the formation of the internally compensated n-doped state of the PA_C. The persistent absorbance is not due to the film becoming p-doped, as if this were the case, the absorbance would be expected to drop to near that of the undoped film and then increase again due to p-doping.

Figure 2.6 shows EQCM results for a single layer film of PA_C deposited on a gold-coated quartz crystal cycled through n-doping potentials and then through positive

p-doping potentials. In the EQCM experiment, voltammetry data (current vs. electrode potential *E*) are collected simultaneously with changes in the resonant frequency (Δf) of the quartz crystal substrate as reflected by the content of Figure 2.6. In the simplest case, the Δf is sensitive to mass changes in the film with a positive frequency shift corresponding to mass loss. The voltammetry data in Figure 2.6 show a clear n-doping wave. The Δf upon sweeping to negative potentials and passing through this doping wave shows first a mass loss (positive frequency shift) and then a mass gain (negative frequency shift). The initial mass loss is consistent with doping supported first by the loss of triflate anions from the film, and the subsequent mass increase is consistent with further doping supported by the incorporation of cations from the electrolyte. Upon reversal of the potential sweep, the Δf trace does not return to its original value, but rather, it returns to the positive frequency maximum that occurred during initial n-doping. This positive difference is consistent with OTf^- anions being lost to the solution during n-doping and hence not being able to support the complete reoxidation to the undoped form. Those OTf^- anions that left the film during n-doping and that had sufficient opportunity to diffuse away from the electrode are not available to support the complete reoxidation of the film, and it remains partially n-doped. Analysis of the voltammetry data also supports the assertion that the polymer film remains n-doped as was previously reported.[20] A notable aspect is the complete absence of a p-doping wave, which would be clearly observed in the potential range studied had a conventional electrolyte been employed. It is noted that the interpretation of EQCM data can be clouded by viscoelastic effects.[21] Although these cannot be

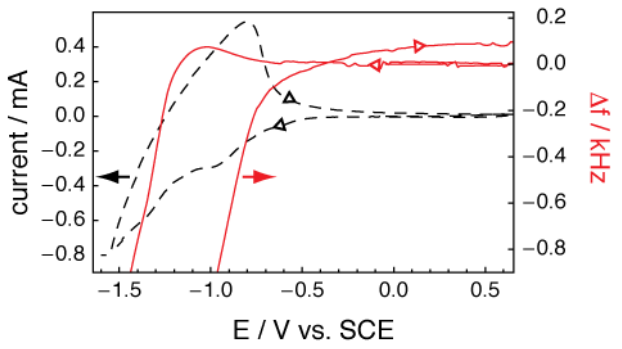

Figure 2.6. EQCM results collected in 0.1M Bu_4NPSS/CH_3CN at a scan rate of 30 mV/s for a 250nm thick film of PA_C. The dotted black line shows the cyclic voltammogram (left axis), and the solid red line shows the change in the resonant frequency (Δf, right axis) of the quartz crystal. The hollow triangles indicate the scan direction. The quartz crystal data are truncated to more clearly show the offset between the initial and final Δf. The ratio of the maximum frequency gain to the maximum frequency loss during the cycle was observed to be 1:16.

completely ruled out, our previous EQCM studies on related ion-functionalized polyacetylenes show a good correspondence between Coulometry and quartz crystal data in Bu_4NPSS / CH_3CN consistent with minimal contributions from viscoeleastic effects.[20]

Figure 2.7 compares a semilogarithmic representation of the J-V_{app} behavior of the PMEC fabricated p-n junction of Figure 2.3 to two other similarly fabricated junctions. The semilogarithmic representation reveals more detail about the J-V_{app} behavior than the linear representation of Figure 2.3. For an ideal diode, J is expected to increase exponentially with applied bias for $\beta V_{app} > 3$, where $\beta = q / (kT)$ in so-called strong forward bias, and J is expected to be a constant for $\beta V < -3$ in so-called strong reverse bias. The slope of the $\log(J)$ - V_{app} curve in strong forward bias is characterized by the ideality or quality factor $n \equiv \beta[d\ln(J) / dV_{app})]^{-1}$ with the minimum value of $n = 1$ indicating the strongest possible dependence of J on V_{app}.

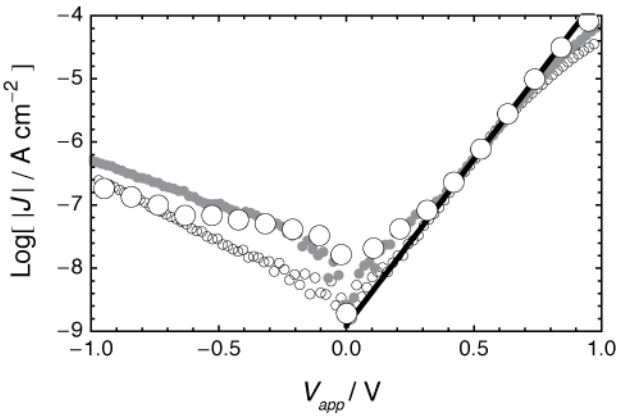

Figure 2.7. Current density (J) - applied bias (V_{app}) data for three separately fabricated PMEC p-n junctions. The large open circles are for the same junction as in Figure 2.3. The small open circles are for a junction with a 430 nm thick PA_A layer and 170 nm thick PA_C layer. The small solid circles are for a junction with a 360 nm thick PA_A layer and 400 nm thick PA_C layer. The solid line is an exponential fit with n = 3.1.

The solid line in Figure 2.7 is a fit to the data in the strong forward bias range of $0.35 < V_{app} < 0.75$V for the same diode as in Figure 2.3, and it is characterized by n = 3.1. The current density data for the three diodes are similar in this strong forward bias voltage range, and with the other two diodes being characterized by n= 3.1 and 3.5.

The J-V_{app} behavior of the p-n junctions exhibits two common deviations from ideal diode behavior. The first is the inevitable deviation from exponential at large forward bias due the finite resistance of the materials and leads; this series resistance results in the downward curvature of the log J - V_{app} data near V_{app} = 1V. The second is the presence of an apparent electrical shunt that prevents the reverse current from saturating and that is also consistent with the positive deviation in J from the exponential fit line in the forward bias voltage range $0.1 < V_{app} < 0.3$ V. The origin of this shunt

appears to be related to imperfections in fabrication, as the reverse bias behavior is not as reproducible as the forward bias behavior.

Comparison of diode quality to junctions fabricated using other trapping approaches is somewhat challenging because of differences in materials, electrode geometry, and electrode materials. Nearly all reports have focused on luminescent polymers with higher band gaps than the non-luminescent polyacetylene materials studied herein. Furthermore, often only limited information on the J-V_{app} behavior is reported due to the emphasis on light emission. A commonly reported figure of merit is the rectification ratio (R), which is the ratio of the forward to the reverse current at a particular voltage. The rectification ratio for the PMEC fabricated polyacetylene junctions herein was found to maximize in the range of V_{app} = 1-1.3 with values as high as 900 being observed. Yu *et al.*[5] report rectification ratios in the range 10^4-10^5 at 4V for a frozen junction based on a poly(phenylene vinylene) derivative and using dissimilar ITO/Al electrodes, which introduces an additional source of asymmetry. Due to series resistance, it was not possible to accurately characterize the rectification ratio of the p-n junction fabricated herein at comparably high voltages. In the ideal case, the rectification ratio increases exponentially with voltage ($R = \beta n^{-1}\mathrm{Exp}[V\beta n^{-1}]$), but it is often limited by either the series resistance or imperfections leading to electrical shunts. Inspection of the J-V_{app} data reported by Yu *et al.*[5] for the frozen junction based on the poly(phenylene vinylene) derivative shows nearly symmetric behavior ($R \approx 1$) out to 2V and $n \approx 5.5$ in the range of V_{app} = 2.5-3.5V where exponential behavior is observed. For junctions fabricated with the ion-pair monomer approach, rectification ratios in the range of 100-

900 at 4V have been reported for structures based on polyfluorene and/or poly(phenylene vinylene) using Au/ITO electrodes.[7]

The diode quality observed with the PMEC approach could not be achieved with the electrochemical disproportionation and trapping approach (EDAT) we previously reported.[12] In this previous report, EDAT was used to fabricated a p-n junction from ion-functionalized polyacetylenes with similar anionic and cationic functional group densities. The rectification ratio for the EDAT fabricated junctions near 1V was nearly a factor of 100 less than reported here. For more direct comparison, an undoped bilayer consisting of the same polymers used herein was subjected to the EDAT approach. The resulting junction was more poorly conductive than the PMEC fabricated junction and had a rectification ratio of less than 5 at 1V.

2.4. Conclusions

The use of the PMEC technique to fabricate internally compensated conjugated polymer p-n junctions was demonstrated. The PMEC fabricated p-n junctions exhibited diode behavior and a photovoltaic effect, with ideality factors in the range of 3-3.5 and rectification ratios as high as 900 near 1V. PMEC is an effective tool for selectively doping regions of an ion-functionalized conjugated polymer structure. It also allows for the n- and p-type sides of the junction to be doped to differing extents, which is not possible with previously developed trapping approaches. The control of doping chemistry in this manner expands the range of electronic and photonic device architectures possible with conjugated polymers.

2.5. Bridge to Chapter III

This chapter demonstrated the use of ionic functionality to create dissimilarly doped regions within a bilayer stucture to fabricate an organic p-n junction. The use of the PMEC technique in conjunction with bound ionic functionality allows for control over electrochemical charge injection processes in single films and composite structures. In this case, the expulsion of the included counterion to generate the internally compensated state allowed for the formation of spatially separated n- and p-type regions. In Chapter III, the role of the internally compensated state and counterion charge-density on chemical charge injection processes is demonstrated with respect to hole injection from molecular oxygen. It will be shown that the continued residence of the counterion within the film, and specifically its charge-density, has a dramatic impact on the rate of polymer degradation.

CHAPTER III

IONIC FUNCTIONALITY AND THE POLYACETYLENE-OXYGEN CHARGE-TRANSFER COMPLEX

3.1. Introduction

In recent years, considerable research has been focused on the use of conjugated polyelectrolytes (CPEs) for applications such as photovoltaics, polymer light-emitting electrochemical cells (PLECs), organic field-effect transistors, chemical sensors, and electrochromic devices.[1-5] Interest in CPEs stems in part from their solution processability, which facilitates thin-film fabrication through a variety of casting techniques such as spin coating, spray casting, layer-by-layer deposition, and ink jet printing.[6-9] It is also well established that the presence of mobile counter-ions has a dramatic impact on the electronic and optical properties of CPE-based devices. For example, mobile ions can impact charge injection through polarization at electrode boundaries,[10-12] and ionic centers can impact photoluminescence and electronic charge carrier mobilities by affecting film morphology and interchain interactions.[13,14]

Despite the emerging importance of CPEs, the influence of CPE ionic groups on the interaction of the conjugated backbone with molecular oxygen has been only marginally explored.[15] While the oxidation and degradation mechanisms of conjugated polymers have been extensively researched by various groups,[16-19] little or no work has been undertaken to investigate the corresponding mechanisms in their ionically functionalized analogues. Herein we report a study of the interaction of molecular oxygen, under ambient photo-oxidative conditions, with an anionically functionalized polyacetylene derivative and with respect to the chemical nature of the counter ion. It was hypothesized that the intermediate polymer-O_2 charge-transfer complex (CTC), common to the oxidation of most conjugated polymers (Scheme 3.1),[16,20] would be stabilized through ionic interactions with high-charge-density ions such as alkali metal cations. The bound anion should aid in this stabilization by compensating the positive charge on the polymer backbone resulting from doping by oxygen. The formation of such a stabilized intermediate would have direct implications to the fabrication of CPE-based devices as well as their conditions of operation. The presence of a CTC with oxygen can dramatically alter material properties such as absorbance, conductivity, photoluminescence, and solubility. Hence, substantial alteration in either the thermodynamics or kinetics of its formation could be critically important to the operation of CPE-based devices and their sensitivity to trace alkali metals and oxygen.

Scheme 3.1. Generalized Oxidation Mechanism of Polyacetylene.

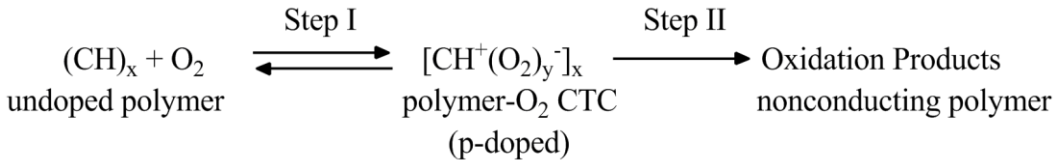

3.2. Experimental

To determine the effect of ionic functionality on the formation and stabilization of the oxygen CTC, thin films of the anionic polyacetylene derivative poly(2-cyclooctatetraenylethanesulfonate) with tetramethylammonium ($TMAPA_A$) or alkali metal (MPA_A, M=Na^+, Li^+) counter ions, and the nonionic derivative poly(trimethylsilylcyclooctatetraene) (PA_{TMS}) were fabricated. The $TMAPA_A$ and PA_{TMS} films were spray or spun cast from solutions of the corresponding polymers in methanol and chloroform, respectively. The syntheses for these polymers are described elsewhere.[21,22] The resulting films were typically 50-100nm in thickness as determined by stylus or optical profilometry. The MPA_A films were prepared using solid-state ion exchange: films of $TMAPA_A$ were submerged in an acetonitrile solution containing 0.1M sodium triflate (NaOTf), lithium triflate (LiOTf), or sodium tetrafluoroborate ($NaBF_4$) for 3 minutes followed by submersion in clean acetonitrile for 3 minutes, and then rinsed before drying under vacuum for ~12hrs. The ion exchange was confirmed using XPS analysis. To monitor the formation and subsequent degradation of the CTC, UV-vis-NIR and FTIR spectroscopy were used to monitor spectral changes associated with the doped intermediate state. These data were used as a metric to determine the

stabilizing effect of ions on the CTC based on the relative rates of formation and photobleaching of associated absorbances. Illuminated films were exposed to fluorescent lighting (~0.4 mw/cm^2) under ambient laboratory conditions. Unless otherwise specified, all experiments were performed in air. NaOTf (Aldrich, ≥98%) was recrystallized (4x) from ethyl acetate and dried under vacuum for 5 days at 80^{o}C. LiOTf (Aldrich, 99.99%) and $NaBF_4$ (Aldrich, ≥98%) were used as received. High purity acetonitrile (Burdick & Jackson) was distilled from molecular sieves (3Å) and stored under N_2 until used.

3.3. Results

A dramatic enhancement of the stability of the polyacetylene-O_2 CTC as the result of ionic functionality and, in particular, the chemical nature of the counter ion was observed. Figure 3.1 shows the UV-vis-NIR spectra of a $TMAPA_A$ thin film before and after ion exchange to the sodium salt. Each film had been exposed to ambient oxygen for approximately 10 min at this point, and further evolution of the spectral features was slow relative to this time scale. The broad spectral feature centered at ~1650nm results from a mid-gap soliton state associated with the doped polymer.[23] The minor presence of this feature in the case of the $TMAPA_A$ film is due to the doping effect of ambient oxygen resulting in the formation of a small amount of the O_2 CTC, and it is reversible when the sample is placed under vacuum, as has been demonstrated by various groups studying the air stability of polyacetylene.[16,24] No such change was observed for the non-ionically functionalized analogue PA_{TMS} after similar exposure to ambient O_2. A much

larger increase in the intensity of the NIR 1650nm absorbance and a decrease in the visible absorbance at ~600nm was observed following ion exchange with Na^+ and subsequent exposure to ambient O_2, occurring on the time scale of seconds to minutes. Control exchange experiments carried out using neat acetonitrile, or solutions containing alkylammonium cations showed no increase in the NIR. Sodium exchange experiments conducted under O_2-free conditions also showed no increase in the NIR. These controls indicate that the substantial doping in the $NaPA_A$ is due to the formation of the polymer-O_2 CTC influenced by the presence of the sodium cation. XPS analyses confirmed the exchange of the TMA ion for Na^+, as well as determined the lack of residual triflate anions, which could affect interpretation of the data (Appendix A).

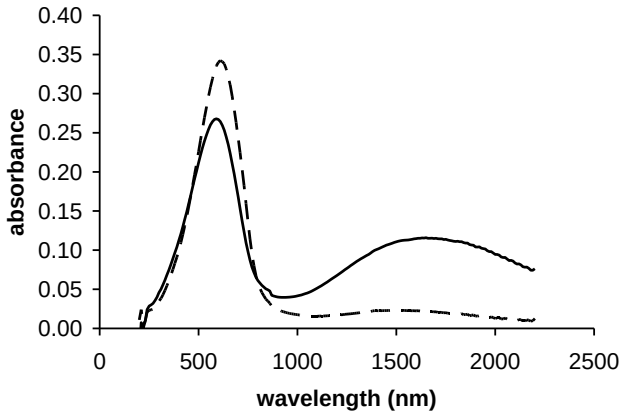

Figure 3.1. Change in absorbance of $TMAPA_A$ film before (dashed line) and after (solid line) ion exchange to the sodium salt.

To further confirm the formation of the CTC, FTIR spectroscopy was used to analyze films before and after ion exchange (Figure 3.2). The salient features seen are the intense, broad bands at ~1400 and 850 cm^{-1}, which are seen to grow substantially upon ion exchange and O_2 exposure. These bands are assigned to charge-coupled

molecular vibrations associated with the doped polymer backbone.[25-27] The appearance of a band at 1140 cm^{-1}, assigned to the C-O stretch, is further evidence of the formation of the CTC.[17]

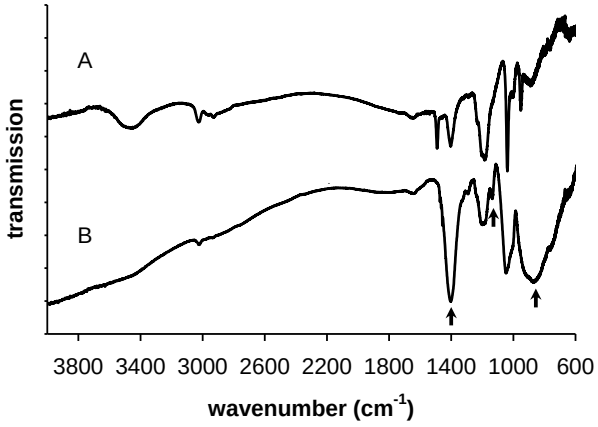

Figure 3.2. FTIR of a $TMAPA_A$ film: (A) as deposited and (B) following Na^+ exchange. The film had been exposed to air for ~10 min in both cases. The broad, intense bands at ~1400 and 850cm^{-1} correspond to the doped polymer backbone, while the band at ~1140cm^{-1} corresponds to the C-O stretch of the CTC.

It is important to note that the intensity of the spectral features in the NIR and IR regions of the non-exchanged polymer do not increase significantly with increased O_2 exposure, but rather they diminish as the polymer degrades. Furthermore, unlike the $TMAPA_A$ films and traditional polyacetylene, the $NaPA_A$ films display no reversibility of the polymer-O_2 complex even after weeks under vacuum. Concomitant with the changes in optical properties was a significant reduction in the film's electrical resistance consistent with oxygen doping.[16,17] Identical analyses of the non-ionic PA_{TMS}, as well as a cationic polyacetylene film displayed none of the spectral features associated with the stabilized formation of the CTC.

To determine the influence of the ion-stabilized CTC on the subsequent degradation of the polymer (Scheme 3.1, step II), films exposed to ambient photo-oxidative conditions were monitored via UV-vis-NIR spectroscopy over a prolonged period of time. The rate of photobleaching of the absorbance in the visible region was used as a metric to determine the influence of the stabilized CTC on the subsequent degradation of the film. Figure 3.3 shows the normalized absorbances at the initial wavelength of maximum absorbance (λ_{max}) for the three films. As can be seen, the PA_{TMS} films completely bleach in the visible region in a period of ~22hrs. This is expected as polyacetylene is known to rapidly degrade under photo-oxidative conditions. The $TMAPA_A$ films completely bleach in ~96hrs, while the $NaPA_A$ films displayed only ~19% loss in absorbance over the same period of time. Also associated with the reduction in absorbance is a blue shift of the λ_{max}, consistent with a reduction in conjugation length as the polymer degrades to carbonyl products. The magnitude of this shift with $NaPA_A$ films was minimal in comparison to that of $TMAPA_A$ (Appendix A). Thin films exchanged using $NaBF_4$ and LiOTf also displayed similar absorbance changes to the $NaPA_A$ films over the same period of time.

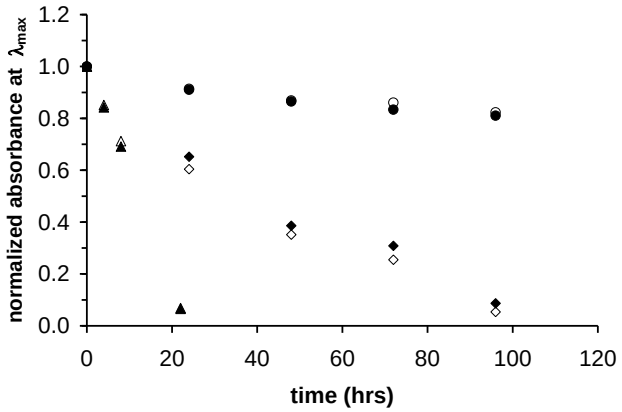

Figure 3.3. Normalized absorbance of thin films of PA_{TMS} (triangles), $TMAPA_A$ (diamonds), and $NaPA_A$ (circles) at the initial wavelength of maximum absorbance (530, 600, and 590nm respectively). The open and filled symbols represent 2 samples exposed to identical photo-oxidative conditions. Film thicknesses were 70nm ($TMAPA_A$ and $NaPA_A$) and 70 and 100nm (PA_{TMS}).

To highlight the observed visual changes associated with CTC formation and subsequent inhibited photobleaching, a simple experiment was conducted in which a paper mask (O shaped) saturated with NaOTf solution was placed atop a spun cast $TMAPA_A$ film (Figure 3.4). The ion exchanged region under the mask displayed a change in absorption (bleaching) in a manner analogous to the solution phase exchange upon CTC formation, resulting in the transfer of the mask pattern to the substrate. Subsequent exposure of the film to photo-oxidative conditions resulted in the inhibited bleaching of the patterned area relative to the non-exchanged region.

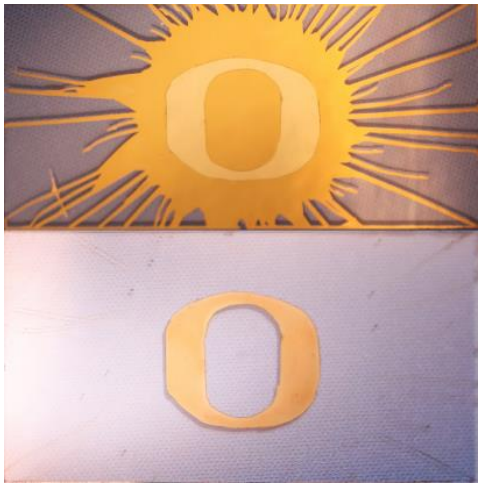

Figure 3.4. Patterned ion exchange of two $TMAPA_A$ films (~200nm) immediately after exchange (top) and after ~3 days exposure to photo-oxidative conditions (bottom). The O-shape is the area exchanged for Na^+.

In work by Arroyo-Villan et. al. on the photo-oxidative stability of sulfonate functionalized polythiophenes,[15] it has been suggested that polymer degradation is inhibited in the presence of alkali metal counter-ions due to an increase in the hydrophilicity of the polymer film. This results in a greater uptake of ambient water, which acts as a singlet oxygen quencher. A singlet oxygen degradation mechanism is believed to occur in solution as well as in amorphous polymer films. To address this possibility, $TMAPA_A$ and $NaPA_A$ films were prepared in quartz cuvettes and re-dissolved in nanopure H_2O (18.2MΩ). These solutions were then subjected to the same photo-oxidative conditions and analysis as the polymer films. Figure 3.5 shows a plot of the normalized absorbance at the initial λ_{max} as a function of time. As can be seen, the Na^+ exchanged polymer bleaches at a rate slower than that of the TMA polymer in a similar manner as seen in the solid films. These data suggest that singlet oxygen quenching due to the presence of water is not solely responsible for the inhibition of degradation, as this would be expected to result in both solutions bleaching at the same rate. Furthermore, as

seen in the IR spectra (Figure 3.2), the intensity of the O-H stretch in the $TMAPA_A$ film is greater than that of the film following Na^+ exchange, again, suggesting that H_2O is not the primary degradation inhibitor.

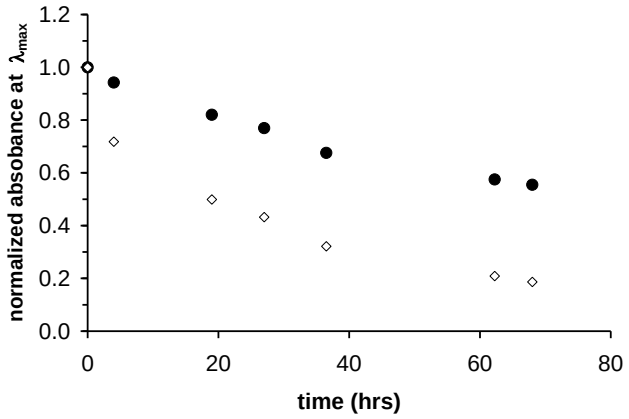

Figure 3.5. Normalized absorbance of aqueous solutions of $TMAPA_A$ (diamonds) and $NaPA_A$ (circles) at the initial wavelength of maximum absorbance (592 and 589nm respectively). Solutions have the same concentrations and were exposed to identical photo-oxidative conditions.

Other groups have found that morphological changes resulting from alteration of polymer packing can have an impact on the rate of photodegradation.[28] This change was attributed to decreases in oxygen permeability due to the formation of polymer aggregates. To address this possibility, AFM was performed on $TMAPA_A$ films before and after exchange to the sodium salt. The results showed no observable alteration of surface morphology or aggregate formation (Appendix A).

3.4. Discussion

The spectral data suggest that the presence of small alkali metal counter ions has a significant impact on the rate of formation of the CTC. Likewise, the slower rate of photobleaching of the visible absorbance of the ionically functionalized films suggests that the presence of ionic functionality has a significant impact on stabilization of the polymer-O_2 CTC. To rationalize the results, a mechanism is proposed in which sodium ion migration from the bound sulfonate stabilizes the negative charge of the CTC (Scheme 3.2). Likewise, the resulting positive charge on the polymer backbone is compensated by the bound sulfonate anion, as demonstrated by several groups in electrochemical doping experiments of CPEs.[22,29] The increase in stabilization of the CTC by the Na^+ (or Li^+) vs. TMA counter ion is not unexpected as the larger charge density of the alkali metal ion will more strongly associate with the negative charge on the oxygen. As this intermediate state is stabilized more effectively by alkali metal cations, subsequent reaction to form the carbonyl degradation products is inhibited. This stabilizing effect is also manifest in the lack of reversibility of the CTC. Extensive work has been reported on the oxidation of polyacetylene in which the formation of the CTC, via oxygen doping, has been shown to be reversible by placing the film under vacuum within a short period of time. Under these conditions, the spectral features associated with the CTC are reversed as the polymer reverts to the neutral state. The conductivity of the polymer also returns to that of the neutral state without significant degradation of the polymer. Research into the environmental stability of other polymer films, such as polythiophene, has shown a similar reversibility.[30] However, in the case of the MPA_A

films, the spectral features are not reversible even with extended time under vacuum. Whether CTC stabilization is kinetically or thermodynamically controlled is currently under investigation.

Scheme 3.2. CTC Stabilization by Sodium Ion Migration

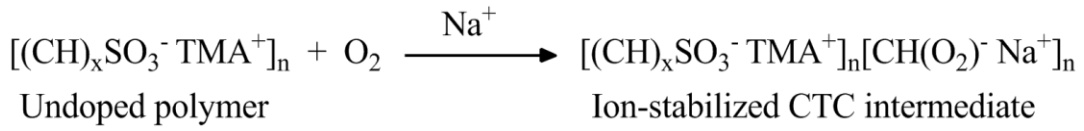

While alteration of polymer conformation cannot be completely discounted, the AFM and spectral data suggests that its impact is not significant. Following ion exchange, a small blue shift is observed in the λ_{max} in the visible region (~10-20nm), which can be attributed to chain twisting or kinking. However, a more likely cause is the reduction in conjugation length from the formation of the polymer-O_2 complex itself. Furthermore, the lack of any observable changes in surface morphology and given the very small values for polymer diffusion coefficients in the solid state,[31] it is unlikely that conformational changes are responsible for the reduction in the rate of photodegradation of the CTC intermediate. This is supported by solution phase experiments, which show only a minor blue shift of the λ_{max} of $NaPA_A$ relative to $TMAPA_A$ (~3nm).

The rapid formation of the CTC also appears to be unique to the anionically functionalized polymer. When analogous experiments were conducted using neutral PA_{TMS} or cationically functionalized polyacetylene derivatives, no spectral changes associated with CTC formation or inhibited degradation were observed. This can be

explained by the proposed mechanism through the synergistic effect of the ability of the bound sulfonate to compensate the net positive charge and the sodium stabilized negative charge associated with the CTC. While it has been reported that chemical or electrochemical p-doping of conjugated polymers will inhibit O_2 oxidation and degradation, no examples of the inhibition of conjugated polymer degradation resulting from an internally ion-stabilized polymer-O_2 complex in the solid state have been reported. In the former case, the doped state is compensated by an introduced dopant anion. In this case, XPS analysis confirmed that no triflate anions were present in the exchanged films, supporting the proposed mechanism. Preliminary results on sulfonate functionalized polythiophenes show an analogous effect as the result of alkali metal cation exchange, suggesting the CTC stabilization may be general with anionic CPEs.

3.5. Conclusion

We have demonstrated that in the presence of alkali metal cations and molecular oxygen, anionically functionalized polyacetylenes rapidly oxidize to form the intermediate CTC. This complex is stabilized by the alkali metal cations more effectively than with larger alkylammonium cations, resulting in decreased rates of photobleaching and the prevention of the reverse reaction to re-establish the neutral polymer. Comparison of polyacetylene CPEs to neutral TMS derivatives indicate that the presence of ionic functionality, in general, affects the stabilization of the CTC. These results have significant implications for the fabrication and operation of CPE-based devices such as light-emitting devices and photovoltaics. If extreme care is not taken to avoid the

introduction of oxygen in the presence of even trace amounts of alkali metal cations, the irreversible formation of the CTC complex will result in altered device performance or the possibility for misinterpreting results if its presence is not recognized. The effects of the CTC on device performance can manifest as decreased quantum efficiencies in devices such as PLECs or reduction in photovoltaic efficiencies, as the result of exciton quenching by the CTC. The preliminary observation of a similar counter-ion effect in sulfonate functionalized polythiophenes suggests that this phenomenon may be a general effect with anionic CPEs. These results suggest that the interaction of CPEs with molecular oxygen may be far more complex than has been seen in the studies of neutral conjugated polymers, requiring

3.6. Bridge to Chapter IV

This chapter demonstrated the significant effect of ionic functionality on chemical charge injection processes in polyacetylene thin films. The stabilization of the intermediate charge-transfer complex through ionic interactions demonstrates how ionic functionality influences the fundamental chemistry associated with conjugated polymer oxidation. In Chapter IV it will be shown that this phenomenon is not isolated to polyacetylene but rather appears to be general to conjugated polymers. It will be demonstrated how the charge density of the ionic group counterion affects, not only the stability of the intermediate CTC, but also the general oxidation reaction pathway in polythiophene thin films.

CHAPTER IV

IONIC STABILIZATION OF THE POLYTHIOPHENE-OXYGEN CHARGE-TRANSFER COMPLEX

The application of conjugated polymers in practical photonic and electronic devices continues to be strongly inhibited by the inherent vulnerability of these materials to photooxidation.[1-7] Of particular interest among this class of materials are poly(3-alkyl) thiophenes and other polythiophene derivatives, which are used as donor materials in bulk heterojunction organic photovoltaics (OPVs). Although much debate remains over the precise mechanisms which lead to irreversible polymer photodegradation, the formation of metastable charge-transfer complexes (CTCs) resulting from photoinduced electron transfer from the polymer to molecular oxygen ($P^{+}O_2^{-}$) are common to many of the proposed mechanisms.[8-14] The significance of these CTCs is that their presence is believed to reduce the rate of overall irreversible polymer degradation through the prevention or inhibition of follow-on reactions or alternate degradation pathways.[3,10,11,14] The inhibition of irreversible polymer degradation through the formation of a polymer-acceptor CTC has previously been demonstrated by incorporating stable electron

acceptors, such as fullerenes or other small molecules such as 2,4,7-trinitrofluorenone;[15-17] however, efforts to reduce the rate of irreversible polymer photodegradation through the stabilization of the *polymer-O_2 CTC* have only recently been explored by our group.[18]

In this letter, we report the substantial influence of ionic interactions on the stability of the polythiophene-O_2 CTC and the corresponding inhibition of irreversible polymer degradation in amorphous polythiophene thin films. Through the incorporation of anionic functional groups containing mobile cations, we demonstrate that electrostatic stabilization of the polythiophene-O_2 CTC is directly correlated to the charge density of the mobile cation. By further elucidating the role of ionic functionality, we provide insight into the chemistry directing mechanistic pathways of photooxidation in conjugated polymers and provide a mechanistic explanation of the unusual photooxidative behavior observed in thin films of similar ionically functionalized polythiophenes as demonstrated by Arroyo-Villan et al. and others.[19,20]

To demonstrate the effect of ionic interactions on the photooxidation of polythiophene thin films, we utilized the conjugated polyelectrolyte (CPE) poly(6-(3-2,2'-bithienyl)-hexanesulfonate) with tetramethylammonium (TMAPT) or alkali metal (MPT, M=Li^+, Na^+, K^+) counterions (Scheme 4.1). Thin films (30 nm) were exposed to long-term photooxidation (~8 days) under ambient laboratory conditions or to short-term accelerated photooxidation (40 min) using a high intensity tungsten light source (700-800 mW/cm^2) under low or high humidity oxygen (1atm). FTIR spectroscopy of thick films (1-3 μm) was utilized to determine the identity of photooxidation intermediates and products in humidified oxygen using the same tungsten light source.

Scheme 4.1. Chemical structure of poly(6-(3-2,2'- bithienyl)-hexanesulfonate).

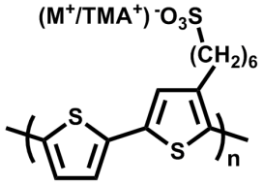

The effect of counterion charge density on overall polymer photooxidation under ambient conditions is shown in Figure 4.1. The rate of photobleaching of the π–π^* absorption at the initial λ_{max} is a commonly used metric for polymer photooxidation.[1,9,15,19] In this case the rate is determined by the slope of the linear portion of the λ_{max} absorption as a function of time. A clear trend is observed between the rate of photobleaching and the charge density of the mobile counterion, with the overall rate increasing with decreasing counterion charge density. The salient feature of the photobleaching data is the large disparity of rates between the TMAPT and MPT films. The ratios of the ionic radii Li^+/K^+ and K^+/TMA^+ are both ~0.6; however, the rate of photobleaching increases by 50% between LiPT and KPT, and by 320% between KPT and TMAPT films. Extensive blue shifting of the λ_{max} of TMAPT films is also observed on this time scale. The large disparity in rates suggests that counterion size alone is not the primary factor affecting the rate of photobleaching, but rather two different photooxidation mechanisms may exist, one dominating in the case of MPT films and another for TMAPT films. It is important to note that poly(3-hexylthiophene) (P3HT) thin films show an increase in photobleaching rate of 30% relative to TMAPT films.

This suggests that anionic functionality, in general, has a stabilizing effect on polythiophene photooxidation.

To account for possible changes in film morphology due to counterion identity, atomic force microscopy (AFM) was used to verify that ion exchange does not alter the nanoscale morphology of the films (Appendix B). This, along with the lack of any significant differences in the initial absorbance spectra of the films, suggests that changes in polymer conformation are not the primary factor in the observed rates. Oxygen permeability is not believed to be a significant factor based on the reported oxygen diffusion coefficient for regiorandom P3HT thin films (1.2×10^{-8} cm^2 s^{-1}).[8] This results in an oxygen diffusion time of <1 ms for these film thicknesses.

Figure 4.2 shows the results of photooxidation of TMAPT and LiPT thin films under accelerated photooxidative conditions. The data show that the predominant photooxidative pathway differs based on the identity of the counterion. In the case of LiPT films, the decrease in the π–π^* absorbance at 440 nm is accompanied by

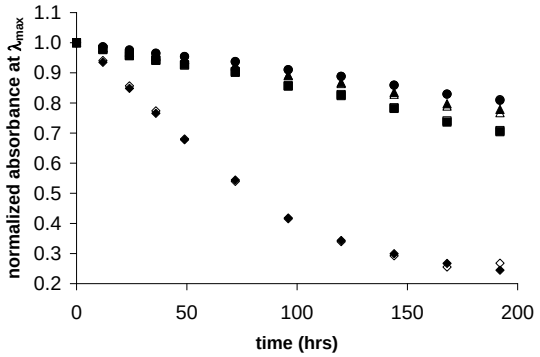

Figure 4.1. Normalized absorbance of thin films of LiPT(●), NaPT(▲), KPT(■), and TMAPT(♦) at 440nm. The open and filled symbols represent 2 samples exposed to identical photooxidative conditions (~0.4 mW/cm^2). Film thicknesses were 30nm.

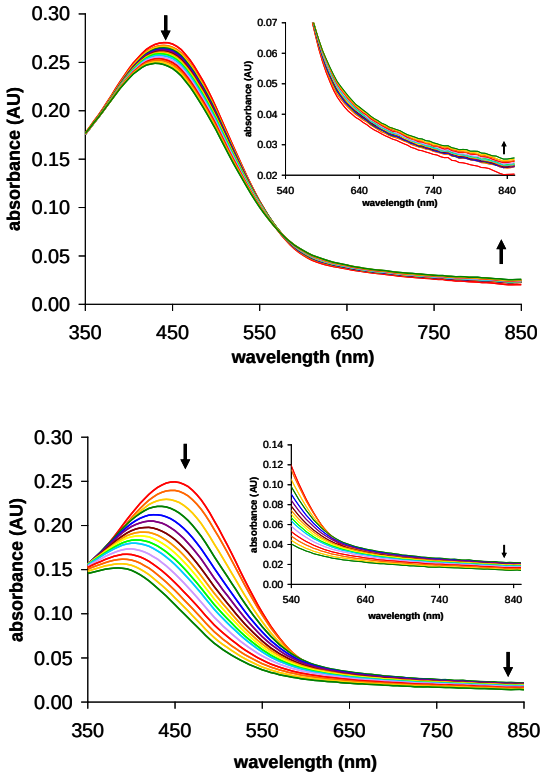

Figure 4.2. UV-vis spectra of initial photooxidation of LiPT (top) and TMAPT (bottom) films under oxygen atmosphere at 90% and 60% relative humidity respectively (800 mW/cm^2). Spectra were collected every 2 min for the first 20, then every 4 min until 40 min total. Insets show the region between 540 and 850nm. Arrows indicate the direction of the absorbance change in each region.

an increase in the vis-NIR absorbance between 600-850 nm, with a clear isosbestic point at ~550 nm. The decrease in the visible range and increase in the NIR are due to the formation of polaron (polymer radical cation) species on the polymer backbone resulting from electron transfer to oxygen (i.e., the formation of the polythiophene-O_2 CTC).[3,19,21,22] KPT films show the same behavior as LiPT films; however, the overall rate of photobleaching is greater than LiPT consistent with the data in Figure 4.1. In the case of TMAPT films, only a decrease of the π–π^* absorbance and significant blue shifting of the visible transition is observed.

It has been suggested by Arroyo-Villan et al. in early studies of polythiophene CPE thin films that an increase in photooxidative stability may result from the increase in hydrophilicity imparted by ionic groups.[19] It was postulated that the increase in water content acted as a singlet oxygen ($^1O_2$) quencher based on the short $^1O_2$ lifetime in aqueous solution; however, the role played by $^1O_2$ in the solid state remains uncertain.[9] Our data show that the rate of photobleaching increases in all films with increasing humidity (Appendix B). It is important to note that in the case of MPT films, both the increase in the vis-NIR and decrease in the visible region are marginally accelerated in the presence of increased humidity; whereas, in the case of TMAPT films, only a dramatic decrease of the visible transition (with extensive blue shifting) is observed.

Figure 4.3 shows the FTIR spectra before and after photooxidation of a TMAPT film in the range of 1850-400 cm^{-1} (full spectra and intermediate times are shown in Appendix B). The FTIR transmission (*T*) spectra of photooxidation products of TMAPT films are found to be in very good agreement with literature reports of the photooxidation

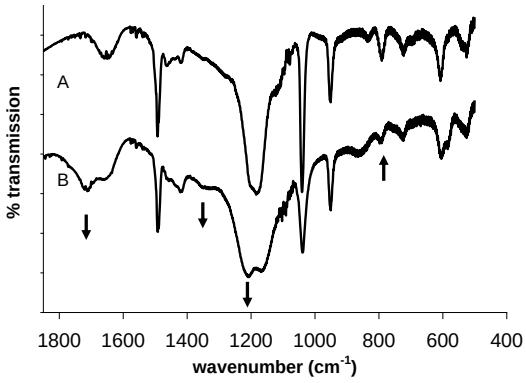

Figure 4.3. (A) Initial and (B) final (165 min) FTIR spectra of photooxidation of TMAPT film (2-3 μm thick) under oxygen atmosphere at 90% relative humidity (700 mW/cm^2). Arrows indicate direction of change and are discussed in the text. Spectra offset for clarity.

of polythiophenes by a $^1O_2$ photooxidation mechanism.[23,24] The prominent bands at 1722, 1360, and 1213 cm^{-1} are assigned to C=O stretching, OH bending, and $C=S^+O^-$ or C=S=O stretching modes, respectively. Concomitant with the appearance of these bands is the decrease in C-H stretching modes in the range of 2800-3000 cm^{-1}, the aromatic C-H stretch at 3050 cm^{-1}, and C-H deformations at 800 cm^{-1}. The small initial band at 836 cm^{-1} is assigned to the O-O stretch of peroxide species and shifts to higher wavenumbers with time and broadens significantly. This broadening and shifting is likely due to the formation of various hydroperoxide and peroxide species in different chemical environments. Following photooxidation, TMAPT samples were placed in the dark under vacuum. No further spectral changes were observed after 2 days in vacuo indicating the formation of irreversible degradation products.

The difference spectra ($\Delta T = T(t)-T(t_{initial})$) for KPT and LiPT films in the range of 1850-400 cm^{-1} are shown in Figure 4.4 (full spectra shown in Supporting Information). The difference spectra allow for the resolution of specific bands that partially overlap with bands due to sulfonate stretches in the 1000-1250 cm^{-1} region. During photooxidation, several prominent bands appear in the FTIR difference spectra. These bands, located at 1333, 1140, 1060, and 1030 cm^{-1}, are assigned to oxygen doping (CTC formation) induced molecular vibrations associated with polarons on the polymer backbone, which are well documented.[25-27] Control doping experiments using I_2 vapor result in the appearance of identical bands (Appendix B). A broad absorbance tail in the region of 4000 cm^{-1} is also observed corresponding to the $D_1 \leftarrow D_0$ transition of the polymer radical cation.[3] The 1060 cm^{-1} band is not resolved in the case of LiPT due to the direct overlap with the SO_3^- symmetric stretch, which is shifted to higher energy due

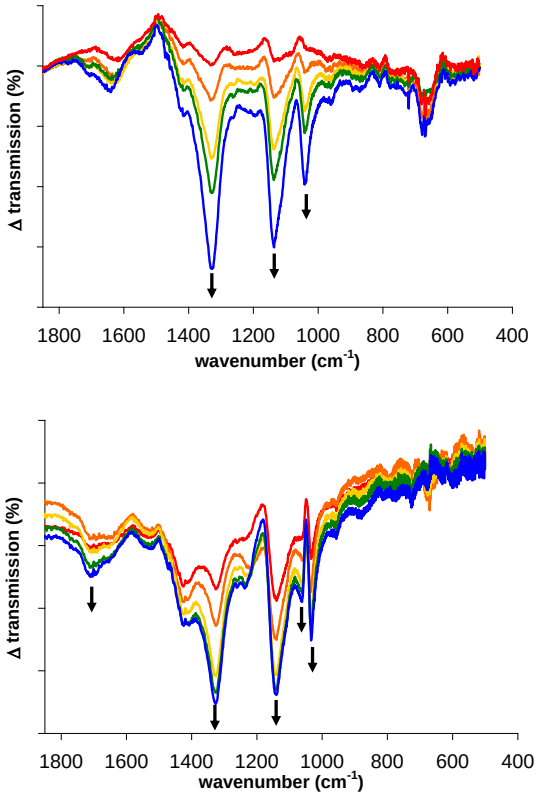

Figure 4.4. Difference FTIR spectra of LiPT (top) and KPT (bottom) films (1-2μm thick) photooxidized under an oxygen atmosphere at 90% relative humidity (700 mW/cm^2). Plots represent 30 min increments from 45 min (red) to 165 min (blue). Arrows indicate direction of change and are discussed in the text.

to the presence of the higher charge density Li^+ ion.[37] The prominent difference between the two films is the emergence of the 1722 cm^{-1} carbonyl band in the KPT films at 105 min. No resolvable peak at this wavenumber is seen in the LiPT spectra on this timescale. In fact, it takes more than 24 hr of continuous irradiation for a small feature at 1722 cm^{-1} to be resolvable (see Supporting Information). Similar long-term photooxidations of KPT and LiPT reveal that the polaron band at 1333 cm^{-1} reaches a maximum at ~2 hr and does not decrease as the 1722 cm^{-1} carbonyl band grows into the spectrum. These data suggest that both irreversible degradation and electron transfer exist in parallel as suggested by other groups.[10,15,21] With continued irradiation (>48 hr),

the 1333 cm^{-1} band does begin to decrease in intensity possibly due to CTC dissociation as suggested in the literature.[8,11,28] The peroxide O-O stretching mode at 836 cm^{-1} is observed in both KPT and LiPT films and does not broaden or shift as observed in the TMAPT films.

To ensure that oxygen permeability was not a factor using these thicker films, control experiments were conducted in which samples were exposed to wet oxygen overnight prior to illumination to allow full saturation of oxygen in the film. No effect on the rate of band formation is observed indicating rapid oxygen diffusion as estimated from the reported diffusion coefficient.

Following photooxidation, MPT samples were placed in the dark in either ambient conditions or in humid oxygen. Surprisingly, the doping induced infrared active bands all completely reverse within ~1 hr with no spectral changes associated with degradation observed (see Supporting Information). This is in stark contrast to reported photooxidations of P3HT thin films, which require vacuum, and often heating, to rapidly reverse oxygen doping.[3,13] Control experiments using regioregular P3HT were performed, and the oxygen doping induced IR bands remain observable for >1 week when stored under identical dark conditions. The mechanism of the rapid reversibility in MPT films is currently under investigation.

The data show the presence of two competing photooxidation mechanisms, the predominance of which depends upon the identity of the mobile counterion. At one extreme is the photosensitization and reaction of $^1O_2$. It is generally accepted that this is the dominant photooxidation mechanism in polythiophene solutions and likely in amorphous films as well,[9,21,23,29,30] although the latter has been questioned in recent work

by Dupuis et al.[38] The formation of irreversible oxidation products observed in the FTIR spectra suggest that this is the dominant mechanism in the case of TMAPT films. The rapid rate of blue shifting and photobleaching observed in the UV-vis spectra of TMAPT films is also characteristic of the $^1O_2$ mechanism as reported by other groups studying the photooxidation of regiorandom P3HT films.[9] At the other extreme is the electron transfer mechanism forming a polythiophene-O_2 CTC. The observation of polaron infrared active vibrations and the lack of carbonyl oxidation products indicate that this is the dominant mechanism in LiPT films. The presence of both mechanisms seen in the KPT films by the appearance of both carbonyl degradation products and polarons in the FTIR spectra, as well as the increased rate of photobleaching relative to LiPT, suggests that a continuum exists in which the rate of electron transfer to oxygen, relative to photosensitization of $^1O_2$, can be correlated to the charge density of the mobile counterion. It is postulated that the rate of CTC formation is increased by the ability of the mobile high-charge-density cation and sulfonate group to effectively stabilize the negative and positive charges on the oxygen and polymer backbone, respectively, via Coulombic interactions. This synergistic ion stabilization of the polymer-O_2 CTC has also been seen in oxidation studies of anionically functionalized polyacetylenes.[18]

While it has been suggested that the presence of excess water acts to quench $^1O_2$,[19] the data presented here do not support this assertion. Zhou et al. has suggested that the presence of water in the photooxidation of P3HT films serves to solvate oxygen, effectively increasing its work function, facilitating electron transfer.[31] The results from the MPT photooxidation experiments in humid and dry conditions support this hypothesis, however due to the hydrophilic nature of the films, it is possible that the

presence of water also increases the mobility of both the polymer chains and mobile counterions as seen in hydration studies of Nafion and other ionically functionalized polymer films.[32,33] This increased mobility would aid in the ability of the ion to take up the most advantageous position for ionic stabilization. This dependence of ion position on CTC stabilization has been demonstrated by numerous groups studying the photosensitization and reaction of $^1O_2$ with alkenes in NaY zeolite pores.[34-36] Our current work is focused on elucidating the molecular structure of the polythiophene-O_2 CTC and how specific ion interactions affect the rate of photooxidation.

We have demonstrated that ionic stabilization of the polythiophene-O_2 CTC in polythiophene films can dramatically affect the dominant photooxidation mechanism and substantially lower the rate of irreversible polymer degradation. The charge density of the mobile counterion has a direct influence on the rate of CTC formation with high-charge-density cations leading to increased rates of electron transfer to oxygen and lower rates of irreversible degradation due to $^1O_2$ photosensitization or other possible competing photodegradation mechanisms. The ability to inhibit degradation of conjugated polymers by incorporating electron acceptors of high electron affinity, such as fullerenes, has been demonstrated in the literature.[15] However, the ability to modulate the effective rates of photoinduced electron and energy transfer through the use of ionic functionality has not been previously explored. The results presented here have a direct impact on the ongoing debate regarding the precise photooxidation mechanism of P3HT films and devices. While several proposed mechanisms exist, including free radical mechanisms,[9,29] $^1O_2$ mechanisms,[10,21,23] and newer mechanisms involving polymer excited state reactions with ground state oxygen,[11] the common factor in these

mechanisms is the formation of the polythiophene-O_2 CTC. Thus, the ability to stabilize the polythiophene-O_2 CTC results in increased inhibition of follow-on degradation reactions or alternate pathways. Inhibiting the rate of photooxidation of polythiophenes and other conjugated polymers is essential for their eventual use in practical devices such as OPVs. The ability to direct photochemical pathways through the use of ion stabilized intermediates opens new and exciting opportunities for the rational design of new materials with applications such as photocatalysis and oxygen reduction reactions.

4.1. Experimental Methods

Polymer synthesis and characterization is described in the Supporting Information. Thin films of TMAPT were spun cast onto glass substrates from methanol solutions (~20 mg/mL). Solid-state ion exchange was performed as described previously to prepare MPT films (M=Li^+, Na^+, K^+).[18] Thick films for FTIR analysis were drop cast onto silicon substrates from methanol or water for TMAPT and MPT (M=Li^+, K^+) respectively. All films were dried under vacuum for >12 hrs prior to analysis. For the long-term photooxidation studies, thin films were exposed to fluorescent lighting (~0.4 mW/cm^2) under ambient laboratory conditions. For short-term accelerated photooxidation experiments, samples were placed in a custom designed chamber under vacuum. The chamber was backfilled with low or high humidity oxygen (1atm). Humidity was determined using a Picotech humidity probe. Photooxidation was conducted using a tungsten light source at a distance of 12 in (~800 mW/cm^2). UV-vis spectra were collected via optical windows on the chamber, which was mounted in the

spectrometer using a custom mount. Photooxidations of thick films (1-3 μm) for FTIR were conducted in wet (RH 90%) oxygen in the same chamber at 1atm and exposed to a tungsten light source at a distance of 10 in (~700 mW/cm^2) for the specified time increments. Samples were removed briefly (5-10 min) to collect spectra.

4.2. Bridge to Chapter V

Chapters III and IV have demonstrated the significant impact of ionic functionality on chemical charge injection processes and reaction mechanisms in conjugated polymer thin films. Chapter V will explore how a third charge injection process, interfacial charge injection in organic photovoltaic devices, is affected by the presence of ionic functionality. In this case, the ionic functionality is associated with another conjugated molecule, the fullerene, which is commonly employed in high efficiency organic electronic devices.

CHAPTER V

INCREASED PERFORMANCE OF INVERTED ORGANIC PHOTOVOLTAIC CELLS USING A CATIONICALLY FUNCTIONALIZED FULLERENE INTERFACIAL LAYER

Reproduced with permission from Weber, C. D.; Bradley, C.; Walker, E. M.; Robinson, S. G.; Lonergan, M. C. (manuscript submitted for publication)

5.1. Introduction

Electrode modification using interfacial layers (IFLs) to enhance the performance of inverted organic photovoltaic cells (i-OPVs) has attracted increased research interest in recent years.[1-3] Modification of electrodes using IFLs has been shown to have a significant impact on the magnitude of the cell's open-circuit voltage (V_{oc}).[2-4] This enhancement of V_{oc} can result from the modification of the electrode work function to increase the built-in potential, as well as enhanced alignment of the electrode work function with the active layer quasi Fermi level for electrons or holes. IFL modification of electrodes can also provide charge selectivity by introducing an energy barrier to a specific sign of charge. This charge selectivity reduces interfacial recombination at the collecting electrode resulting in an increase in V_{oc}.[5] To maximize performance of

devices, it is also important to ensure a low series resistance (R_s) to maximize charge extraction and enhance the fill factor (FF).[6]

Numerous IFLs have been investigated to modify the transparent electron collecting electrode, typically indium tin oxide (ITO), in i-OPVs. These include n-type wide bandgap semiconductors such as TiO_2[7] and ZnO,[8] graphene,[9] fullerene films[10,11] and self-assembled monolayers (SAMs),[12,13] conjugated polymers,[1] and conjugated polyelectrolytes (CPEs).[14] The use of ion-containing IFL materials, such as CPEs, are particularly attractive as they posses orthogonal solubility to most active layer bulk heterojunction (BHJ) blends which facilitates solution processability. Furthermore, CPEs containing cationic functional groups have been shown to effectively reduce the ITO work function which defines the ITO polarity and promotes Fermi level alignment with the acceptor phase in the inverted structure.[15-17]

Fullerene based IFLs have recently gained interest as efficient electron collecting electrode interfacial layers (n-IFLs) in inverted and conventional BHJ solar cells. Fullerene derivatives are advantageous as n-IFLs due to their energy-level alignment with the PCBM acceptor phase, resulting in efficient charge transfer with minimal voltage loss. In addition, the low-lying HOMO level of fullerenes enhances carrier selectivity by inhibiting hole transfer from the donor polymer. Cationically functionalized fullerene n-IFLs have been demonstrated by Jen *et al*. in conventional OPVs;[18] however, due to poor solvent resistance, fullerene n-IFLs in the inverted geometry have often required chemical cross-linking or the use of fullerene SAMs which are chemically bound to the substrate.[19,20] The relatively low conductivity of fullerene n-IFLs has also often required the use of an underlying n-type IFL such as TiO_2 to reduce R_s.[2,12] To overcome this

shortcoming, chemical n-doping of fullerene IFLs by co-evaporation with Cs_2Co_3 or incorporation of n-dopants, such as decamethylcobaltacene or alkali carbonates have been reported.[10,20,21]

Herein we demonstrate the use of the highly conductive, alcohol-soluble, cationically functionalized fullerene derivative N,N,N-trimethyl-5-(N-methyl-3,4-[60]fulleropyrrolidin-2-yl)pentan-1-aminium bromide (NMFP-Br) as an efficient electron collecting electrode interfacial layer in poly(3-hexylthiophene):[6,6]-phenyl-C_{61}-butyric acid methyl ester (P3HT:PCBM) inverted organic photovoltaic cells. The incorporation of NMFP-Br as an n-IFL results in a substantial increase of the V_{oc} from 0.41V to 0.60V and the overall power conversion efficiency (PCE) from 2.1% to 3.5% under AM 1.5G illumination. The unusually high conductivity of this material results in a significant decrease in the series resistance, relative to control devices, even when the n-IFL thickness is increased fivefold.

5.2. Experimental

5.2.1. Synthesis of N,N,N-trimethyl-5-(N-methyl-3,4-[60]fulleropyrrolidin-2-yl)pentan-1-aminium bromide (NMFP-Br)

Sarcosine (0.3g, 3.4 mmol) and 6-bromo-hexanal (240 mg, l.34 mmol) were added to a solution of C_{60} (654 mg, 0.91 mmol) in deoxygenated toluene (600 mL). The solution was heated to a reflux for 2 hours turning from purple to a dark brown at which point it was cooled to room temperature, concentrated to ~100 mL and then purified by

silica gel column chromatography using toluene as eluent. Eluting first was unreacted purple starting material, followed by the mono-adduct (300 mg) followed by multiple addition products (240 mg). Trimethylamine (3 mL) was added to a solution of the mono adduct (170 mg, 0.18 mmol) in $CHCl_3$ (200 mL) at 0°C, the flask was sealed and the solution was allowed to warm to room temperature. After stirring for 5 days, N_2 was bubbled through the solution for 1 hour with the gas afterwards being passed through an HCl column (removes the NMe_3 as the hydrochloride salt). The solvent was evaporated and the solid was washed with a small amount of methanol to give the product as a brown powder (142 mg, 0.14 mmol, 78%).

^{1}H NMR (600 MHz, $CDCl_3$) δ 4.82 (d, 1H, J =9.7 Hz), 4.17 (d, IH, J =9.6 Hz), 3.91 (t, 1H, J = 5.3 Hz), 3.43 (t, 2H, J =6.5 Hz), 2.99 (s, 3H), 2.57-2.52 (m, 1H), 2.43-2.38 (m, 1H), 2.0-1.91 (m, 4H), 1.64 (quin, 2H, J = 7.5 Hz)

^{13}C NMR (151 MHz, $CDCl_3$) δ 156.60, 154.64, 154.47, 153.47, 147.44, 147.40, 146.86, 146.58, 146.52, 146.49, 146.45, 146.37, 146.35, 146.29, 146.24, 146.17, 146.14, 145.98, 145.75, 145.65, 145.61, 145.58, 145.54, 145.50, 145.48, 145.42, 145.38, 144.93, 144.76, 144.61, 144.54, 143.38, 143.26, 143.34, 142.89, 142.85, 142.82, 142.80, 142.39, 142.35, 142.33, 142.27, 142.25, 142.23, 142.03, 141.92, 141.88, 140.47, 140.39, 139.98, 139.85, 137.38, 136.39, 136.05, 135.66, 129.19, 128.38, 78.20, 76.40, 70.60, 70.31, 40.21, 33.87, 32.65, 31.04, 28.94, 26.72.

5.2.2. Device Fabrication

Inverted devices were fabricated using patterned ITO coated slides (R_s ~5-15 Ohm/□) sequentially cleaned with detergent solution (Micro-90), acetone, and isopropyl alcohol in a sonicator for 15 min each. NMFP-Br was spin cast from dilute methanol solution (<0.5 mg/mL) or DMSO:1% H_2O (5 mg/mL) solution at 1000 and 500 rpm for 60 s and 16 min respectively. Devices were annealed in vacuo for 90 min at 110°C. NMFP-Br coated and control substrates were transferred to a nitrogen filled glovebox for further fabrication. An active layer blend (1:0.8 wt% / conc. 43 mg/mL) of P3HT (Sigma Aldrich) and PCBM (SRS Research) was prepared in deoxygenated ortho-dichlorobenzene (Sigma Aldrich). The active layer was spin cast at 900 rpm for 20 s and allowed to slow dry for 10 min followed by annealing at 110°C for 5 min resulting in an active layer thickness of 160 nm. PEDOT:PSS (Sigma Aldrich) was then spin cast from a 1:5 dilution in isopropyl alcohol at 4000 rpm for 60 s followed by a 10 min anneal at 120°C. A second PEDOT:PSS layer was then applied and annealed following the same parameters. Gold (45 nm) was deposited at a pressure $<10^{-6}$ mTorr through a shadow mask to define a device area of 0.03 cm^2 (device architecture shown in Figure 5.1a).

5.2.3. Measurements

Device layer thicknesses were determined using a Dektak stylus profilometer. Current density-voltage (*J-V*) measurements were taken using a Keithley 2400 or 236 source measure unit. Photocurrent density-voltage measurements were performed using

an AM 1.5G solar simulator (Oriel) calibrated to 97 mW/cm^2 with a thermopile power meter. External quantum efficiencies (EQE) were determined using a custom designed spectrometer and an Agilent 4156C source measure unit.

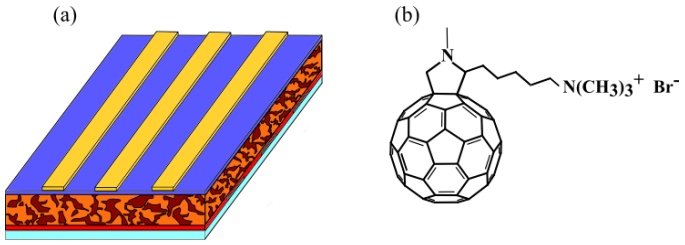

Figure 5.1. (a)Architecture of inverted device: glass substrate/ITO/NMFP-Br/P3HT:PCBM/PEDOT:PSS/Au with an ITO and Au electrode overlap area of 0.03cm^2 and (b) the chemical structure of NMFP-Br.

5.3. Results and Discussion

The average *J-V* curves of inverted devices with and without NMFP-Br n-IFLs are shown in Figure 5.2 and properties tabulated in Table 5.1. The devices containing NMFP-Br n-IFLs show a significant V_{oc} increase of ~190 mV relative to control devices containing no IFL. This increase in V_{oc} results in an average PCE increase of from 2.0% to 3.2%. The small decrease in V_{oc} observed between the 4 nm and 20 nm NMFP-Br devices is likely the result of increased interfacial roughness observed with the thicker n-IFL layer. Such roughness may result in an increased number of interface traps resulting in enhanced carrier recombination. Devices with and without n-IFLs have external quantum efficiencies of 55% at 545 nm and a value of 60% for the best device with a 20 nm n-IFL (Figure 5.3).

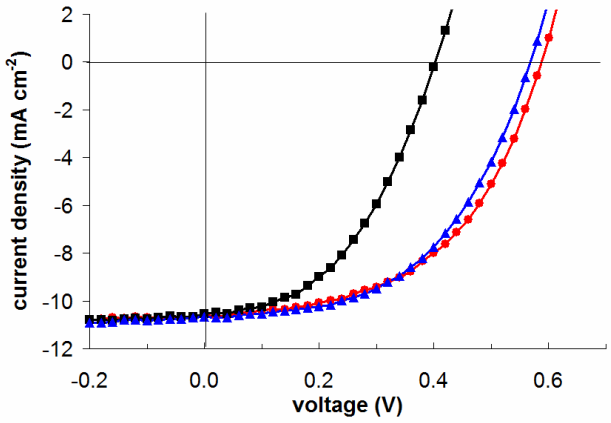

Figure 5.2. *J-V* curves of devices under AM 1.5G illumination with 4 nm (red circles) and 20 nm (blue triangles) NMFP-Br n-IFLs, and no n-IFL (black squares). Illumination intensity is 97 mW/cm^2.

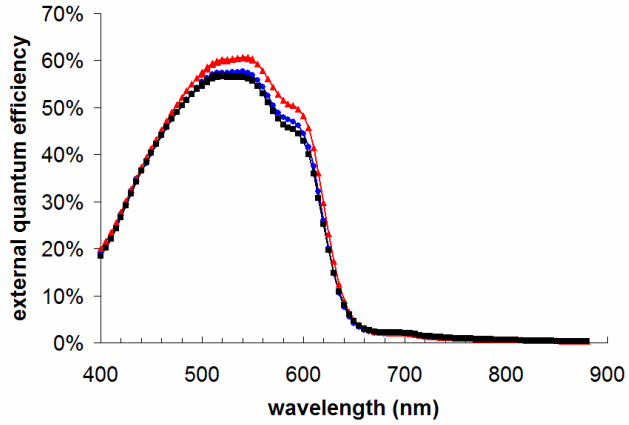

Figure 5.3. External quantum efficiencies of i-OPVs with 20 nm NMFP-Br n-IFL(red triangles) interlayer (best device, PCE 3.5%), 4 nm n-IFL (blue diamonds) and no n-IFL (black squares).

Table 5.1. Summary of average (5-10 devices) device properties with different n-IFL thicknesses. Values in parentheses are from the device with the highest PCE value from each data set.

NMFP-Br layer thickness (nm)	V_{oc} (V)	J_{sc} (mA/cm^2)	FF (%)	PCE (%)	R_s[a] (Ohm cm^2)
0	0.40	10.5	46	2.0	8.4
	(0.41)	(10.6)	(46)	(2.1)	(8.1)
4	0.59	10.6	51	3.3	3.3
	(0.60)	(10.6)	(52)	(3.4)	(3.9)
20	0.57	10.7	50	3.2	2.4
	(0.59)	(11.5)	(50)	(3.5)	(3.6)

[a] R_s determined utilizing an equivalent circuit description detailed in ref 22 and device area of 0.03 cm^2.

The effect of the NMFP-Br n-IFL on the dark *J-V* curves is shown in Figure 5.4. A significant reduction of the dark current is observed in devices containing NMFP-Br. The correlation between reduced dark current and increased V_{oc} has been well documented in OPVs,[23] although the precise mechanism by which IFLs reduce the dark current is still debated. Both work function alteration due to dipole interactions and increased selectivity have been cited as causes of this reduction.[5,15] In this case, due to the presence of ionic groups and the n-type character of the fullerene molecule, both mechanisms likely contribute to the reduction in dark current and concomitant increase in V_{oc}. However, the work function of the NMFP-Br layer itself may also contribute to the observed change (vida infra).

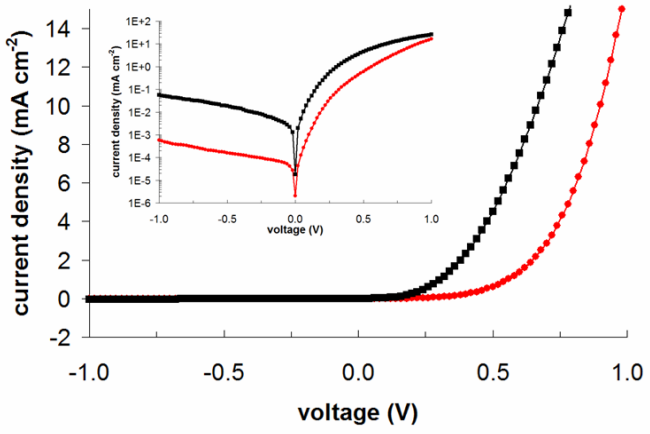

Figure 5.4. Dark *J-V* curves for device containing a 4 nm NMFP-Br n-IFL (red circles) and no n-IFL (black squares). Logarithmic scale plot shown in inset.

i-OPVs have often displayed poor fill factors relative to conventional devices, in large part due to the series resistance associated with the ITO-active layer interface.[3] Thus, efforts to increase performance have focused on n-IFLs which not only provide an enhancement of V_{oc}, but also reduce R_s. As seen in Table 1, the R_s of devices containing NMFP-Br n-IFLs are significantly lower than that of control devices, by a factor of 250% in devices containing a 20 nm n-IFL. This also contributes to an increase in FF of 11%, although alteration of the nanoscale BHJ morphology due to NMFP-Br cannot be discounted. It should be noted that the R_s of devices containing the 20 nm n-IFL are lower than that of the 4 nm devices. This is possibly due to pinholes in the thinner layer through which the active layer can come in contact with the ITO electrode, contributing to an increase in R_s.

Due to the low conductivity of many n-IFL materials demonstrated in the literature, electrically thin layers are often required to facilitate electron tunneling.[15] As layer thickness is increased, the bulk conductivity of the IFL material can inhibit charge extraction resulting in increased R_s and lower J_{sc} and FF.[15,24] The low R_s of devices

containing NMFP-Br n-IFLs with increased thickness (20 nm) suggests a relatively high conductivity. To examine this possibility, conductivity measurements were performed using interdigitated Au electrodes. Samples were heated under vacuum to remove any residual oxygen which is known to act as an electron trap.[25] Figure 5.5 shows the change in conductivity while heating at 120°C, and the final conductivity after the sample was cooled to room temperature. Surprisingly, the NMFP-Br film shows a conductivity ~3 orders of magnitude higher than that of PCBM, which was used as a control. This behavior was reversible upon exposure to oxygen. Jen *et al.* recently reported the unusually high conductivity of a similar cationically functionalized fulleropyrrolidinium derivative, and ascribed the increased conductivity to doping of the fullerene core by the iodide counterion.[26] Counter anion doping of cationically functionalized conjugated molecules and polymers has also been proposed by other groups.[27,28] UV-vis-NIR analysis of NMFP-Br films, however, did not reveal any evidence of characteristic n-doping peaks in the near IR region,[29] however, this may simply suggest the film is not heavily n-doped. Large conductivity changes with low levels of n-doping have been demonstrated for fullerene films.[21] Counterion n-doping would result in a decrease of the NMFP-Br work function. This decrease may contribute to the observed reduction in dark current and V_{oc} increase observed in devices containing n-IFLs. The lack of significant change in *J-V* characteristics under illumination with increasing n-IFL thickness supports this assertion as bulk properties become more relevant with increasing thickness.

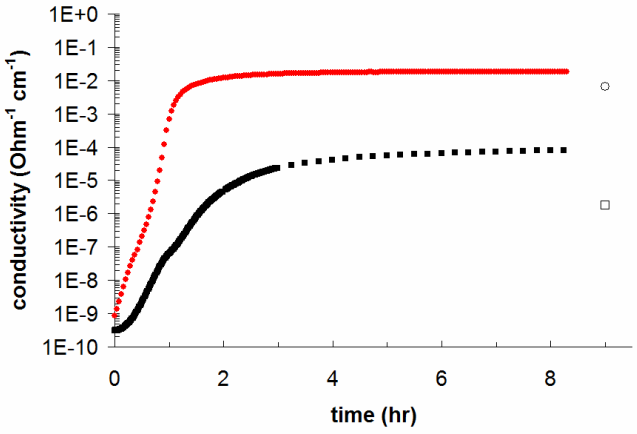

Figure 5.5. Conductivity as a function of annealing time at 120°C under vacuum using interdigitated Au electrodes. Films were drop cast from DMSO/1%H_2O solution. NMFP-Br films (red circles) and PCBM control (black squares). Data point at 9 hr (open symbols) is the final conductivity at room temperature.

5.4. Conclusion

In conclusion, we have demonstrated a significant power conversion efficiency increase in inverted P3HT:PCBM bulk heterojunction photovoltaic cells though the use of a cationically functionalized fullerene derivative NMFP-Br. The PCE increased an average of 60%, from 2.0% to 3.2%, with a maximum PCE value of 3.5% observed. An increase in device V_{oc} of up to 200 mV is observed upon incorporation of NMFP-Br n-IFLs, resulting from a substantial decrease of the dark current density. The high conductivity of NMFP-Br, which has been shown possess a conductivity of ~3 orders of magnitude greater than PCBM, results in a 250% decrease in the series resistance and 11% increase in the fill factor when incorporated into the device structure.

5.5. Bridge to Chapter VI

This chapter demonstrated the phenomenological effect of incorporating ionically functionalized fullerenes as an interfacial layer in operation OPV devices. However, the underlying mechanism of the observed increase in conductivity and other device parameters remains uncertain. In Chapter VI it will be demonstrated that chemical reactions between anions, specifically F^-, and fullerenes and PCBM readily occur in solution. This work sheds insight onto the possible underlying chemical reactions which result in the observed enhancement in device performance.

CHAPTER VI

SOLUTION PHASE n-DOPING OF C_{60} AND PCBM USING TETRABUTYLAMMONIUM FLUORIDE

The use of ionically functionalized polymers and molecules as electron-selective interfacial layers in organic photovoltaic cells (OPVs) has attracted significant research interest in recent years.[1-5] Devices fabricated using these materials, such as ionically functionalized polyfluorenes and fullerenes, have displayed power conversion efficiencies up to ~9%, largely due to an increase in the cell open-circuit voltage (V_{oc}).[1-5] Despite these advances, the mechanism by which these materials affect device performance remains uncertain. [1-8] The observed increase in V_{oc} is typically attributed to electrode work function reduction from preferential orientation of ionic pendant groups and associated counterions, resulting in a net dipole.[1-7] While it is likely that interfacial dipoles are present, the role of potential chemical reactions between the ionically functionalized material and active layer has received relatively little attention.[7,9,10]

Recently, Li et al. reported unusually high conductivities (up to 3.2 S/m) in PCBM / fulleropyrolidinium iodide blend thin films.[11] It was shown subsequently that

films deposited from solutions of tetrabutylammonium salts (TBAX: X = F, Br, I, OH, AcO) and PCBM also resulted in highly conducting films.[12] Based on solution phase studies using C_{60}, it was postulated that direct electron transfer from anion (OH^- or F^-) to fullerene results in the n-doped C_{60} radical anion ($C_{60}^{\bullet -}$) and donor radical ($OH^\bullet$ or $F^\bullet$). These studies suggest that redox reactions between the interfacial material anions and PCBM in the active layer results in interfacial n-doping which would have significant effects on interfacial energetics and charge extraction. However, given the electrophilicity of the fullerene molecule and nucleophilicity of anions studied, particularly F^- and OH-,[13] the possibility of chemical reactions is significant in both solution and solid state. Based on this, as well as the large mismatch in standard reduction potentials between OH^- / F^- and C_{60},[14] we hypothesized that the reported observation of radical species resulted from an initial chemical reaction between the nucleophile and C_{60} followed by electron transfer to a second C_{60} molecule (Scheme 6.1). Similar reactions have been demonstrated previously in both solution and the solid state[15-18] Such reaction chemistry would result in the generation of numerous potential products. The understanding of such chemistry is essential for elucidation of a mechanistic description of interface energetics and charge extraction processes towards the rational design of highly efficient OPVs.

UV-vis-NIR spectroscopy was used to monitor the reaction between TBAF (utilizing the trihydrate salt) and C_{60} in deoxygenated ortho-dichlorobenzene (o-DCB). Upon the addition of TBAF to C_{60} , the solution color changed from purple to dark green. The spectra of 0.5 mM C_{60} solutions with increasing equivalents (eq) of TBAF are shown in Figure 6.1. The spectra show two superimposed features in the NIR range, one broad

feature centered at 933 nm and a sharper feature at 1077 nm. An increase in the high energy portion of the spectrum (400-600 nm) occurs due to a decrease in fullerene symmetry.[19]

Scheme 6.1. Proposed reaction scheme for generation of $C_{60}^{\bullet -}$ via reaction of F^- and C_{60}.

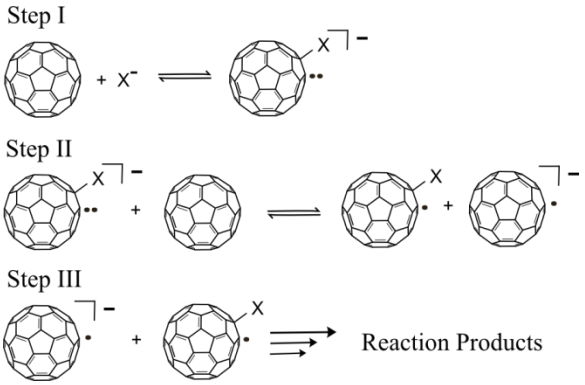

A new small feature at 490 nm is also observed as the concentration of F^- increases. The sharp 1077 nm feature, which contains higher energy vibronic structure, is characteristic of $C_{60}^{\bullet -}$, which has been extensively characterized.[19-24] The broad feature at 933 nm is likely that of the $(C_{60}\text{-}F)^-$ (or $(C_{60}\text{-}OH)^-$, vida infra) formed from the initial reaction in step I of Scheme 6.1, as has been reported by groups studying analogous oxygen nucleophile / C_{60} reactions.[15,16] Similar NIR spectroscopic signatures of C_{60} radical adducts have also been reported in this range.[25-27] It is noteworthy that only a broad NIR feature centered at ~930 nm was reported by Li et al.[12] To confirm that these peaks belong to unique chemical species, the reaction was monitored over time at each F^- equivalent value. Figure 6.2 shows the UV-vis-NIR feature progression for 1 and 6 equivalents of TBAF in 0.5 mM C_{60} solution. At 1 eq, the two NIR features increase at

roughly the same rate. These features also appear simultaneously at early timescales (~3 s). The spectra at 6 eq show a decrease of the 1077 nm feature with little change to the 933 nm feature, indicating the peaks are of distinct chemical origin. Over longer periods of time the 933 nm feature decreases in intensity. Intermediate F^- eq values show a transition at ~4 eq where the 1077 nm peak initially increases, then decreases with time (Appendix C). The disappearance of the 1077 nm peak is likely due to follow-on radical reactions such as dimerization and polymerization, or possible reactions with water in solution.[25,28] The small peak at 490 nm observed at 6 eq continues to increase as the 1077 nm peak decreases suggesting the formation of a new species.

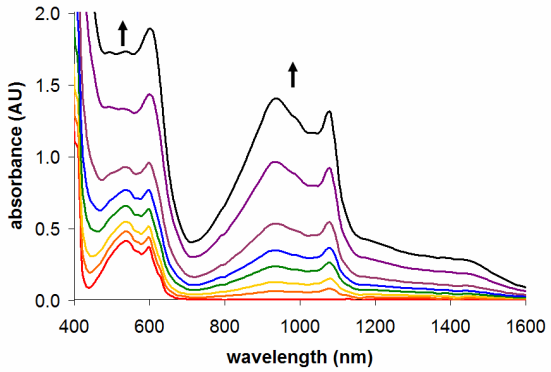

Figure 6.1. Spectra of C_{60} solutions with 0, 0.5, 1, 1.5, 1.75, 2, 4, and 6 eq TBAF (bottom to top) measured at 180 s from start of reaction in deoxygenated o-DCB.

To confirm the presence of new chemical species in solution, cyclic voltammetry (CV) was performed on 0.5 mM solutions (0.1 M tetrabutylammonium tetrafluoroborate in o-DCB) of C_{60} with increasing equivalents of TBAF. Figure 6.3 shows the results of the CV for 0, 1.3, 5, and 10 eq TBAF. The voltammogram of C_{60} with no TBAF present

shows a 1 electron reversible process at -1.1 V vs. Fc/Fc^{+}, very close to literature values for C_{60} / $C_{60}^{\bullet-}$ in other solvent systems.[14]

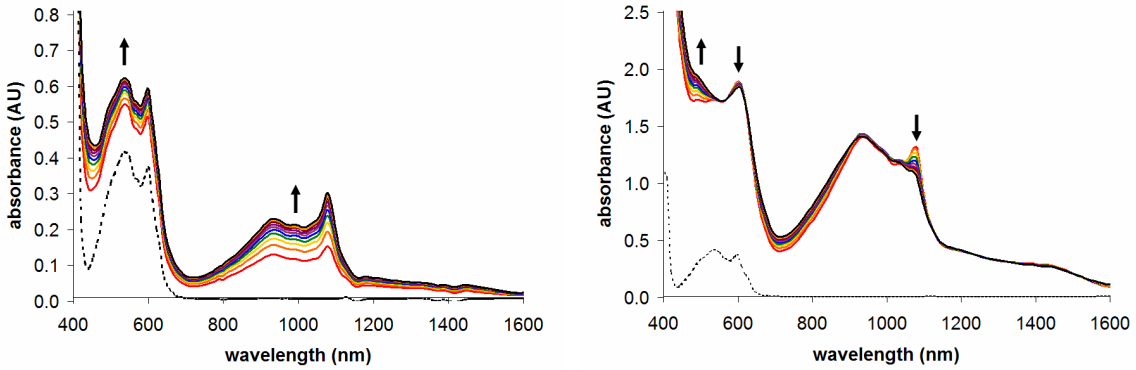

Figure 6.2. Time progression of 0.5 mM C_{60} reaction solutions with 1 eq TBAF (top) and 6 eq TBAF (bottom). The dashed line is that of the C_{60} solution with no TBAF. The time increment between each plot is 180 s. Arrows indicate the direction of change of the indicated spectral features.

The voltammograms shows a chemically irreversible oxidation feature with an onset at ~ -0.5 V vs. Fc/Fc^{+}. Control voltammograms using only TBAF showed no oxidation feature in the potential range studied. This oxidation feature is attributed to oxidation of $(C_{60}\text{-}F)^{-}$. A similar oxidation was reported by Fukuzumi et al. in studies of methoxylated C_{60} species.[16] Concomitant with the oxidation feature is a decrease in current of the C_{60} / $C_{60}^{\bullet-}$ process, indicating a decrease of C_{60} concentration as the equilibrium in step I shifts to the right. When numerous cycles were recorded, the oxidation feature current continued to increase as the C_{60} / $C_{60}^{\bullet-}$ current decreased with time, similar to the spectroscopic observations, indicating the consumption of C_{60} via a chemical reaction.

The data suggests that the solution phase reduction of C_{60} results from the initial chemical reaction of F^{-} with C_{60} to form the $C_{60}\text{-}F^{-}$ anion adduct, rather than a direct electron transfer from F^{-}. The formation of the $C_{60}\text{-}F^{-}$ anion adduct in step I of Scheme

6.1 is slow relative to electron transfer to a second C_{60}, in step II. Oxidations of this type have been observed by numerous groups and have been utilized in the synthesis of various fullerene derivatives.[15,17] The observation of fast electron transfer kinetics in step II is supported by studies of self-exchange rate constants for fullerene adduct anions (1.9×10^8 M^{-1} s^{-1}).[29] However, ^{19}F NMR analysis of deoxygenated reaction solutions did not indicate the presence of C-F bonding. It is likely that the presence of water (due to the hydrated salt) results in exchange reactions resulting in F^- being replaced by OH^- and the generation of the hydroxylated fullerene and HF as reported in substitution reactions with fluorinated fullerenes.[30] Dehydration of TBAF is difficult due to the unstable nature of the anhydrous salt.[31] It is also possible that, due to the basic nature of F^- and the presence of water from the hydrated salt, that OH^- is generated initially and the resultant OH^- ion reacts with C_{60}. However, as demonstrated by Albanese et al., F^- still behaves as a strongly nucleophilic agent even when TBAF is in a highly hydrated state (up to 10 eq H_2O). In either case, the net result is the consumption of C_{60} via a chemical reaction, and not a 1 electron reduction as suggested by Li et al.

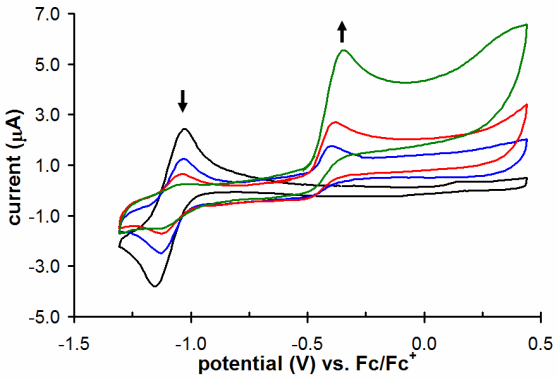

Figure 6.3. Cyclic voltammetry of 0.5 mM C_{60} in 0.1 M $TBABF_4$ in o-DCB with 0 (black), 1.3 (blue), 5 (red), and 10 (green) eq of TBAF. Scan rate was 50 mV/s.

The reaction of TBAF with PCBM in solution was explored by Li et al. with no reaction being observed. However, upon removal of the solvent via spin casting of thin films, an EPR signal was observed.[12] It was proposed that the close proximity of the anion and fullerene in the solid state lowered the barrier for electron transfer. To probe this mechanism, analogous experiments to that of the C_{60} system were performed using PCBM. No reaction with TBAF was observed, in various solvents, even after stored for extended periods of time as monitored by UV-vis-NIR spectroscopy and ^{13}C NMR, similar to that reported by Li et al. In an attempt to mimic the conditions of spin casting, a PCBM / TBAF (5eq) solution (5 mg/mL in deoxygenated CH_2Cl_2) was prepared and the solvent removed via vacuum at room temperature. Upon reduction of volume by ~1/2, the solution color changed from maroon to dark brown. An aliquot of this reaction solution was diluted in deoxygenated CH_2Cl_2 and analyzed via UV-vis-NIR spectroscopy (Figure 6.4). The spectrum shows extensive broadening of the visible region as well as a similar NIR absorbance to that seen with the TBAF / C_{60} reaction. In this case, the broad peak is centered at 900 nm and a shoulder is seen at 1020 nm, the latter being assigned to $PCBM^{\bullet-}$.[21,32] The process was not reversible upon an addition of excess solvent. A similar result was observed when using more dilute solutions, evaporating the solvent, and re-dissolving the resulting solid. The re-dissolved solid was a bright orange color and soluble in acetonitrile. The CV of the crude product in acetonitrile showed an electrochemically irreversible voltammetric wave near -0.4V vs. Fc/Fc^+ indicating an increase in electron affinity relative to pristine PCBM (Appendix C).

The PCBM / TBAF results are quite intriguing as a reaction is only observed when the PCBM solution is brought near its solubility limit (with respect to PCBM). This was verified by adding acetonitrile to CH_2Cl_2 solutions of PCBM until the solution became turbid. TBAF was then added and the solution turned clear and orange in color. A similar NIR absorption was observed. These results suggest that clustering of PCBM molecules may increase reactivity with F^- and subsequent electron transfer, possibly due to increased charge delocalization.[33]

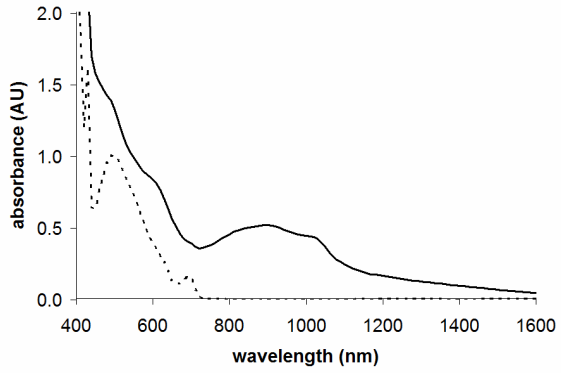

Figure 6.4. Spectrum of PCBM / TBAF reaction solution (solid) following dilution in in deoxygenated CH_2Cl_2. The dashed spectrum is that of a reference PCBM in CH_2Cl_2 solution to show location of spectral features.

As opposed to the reaction solutions of C_{60} / TBAF, the PCBM solutions contained a new ^{19}F NMR singlet at ~ -157 ppm (Appendix C). Separation of reaction products and a detailed structural characterization is on-going.

The production of nucleophilic anionic fullerene derivatives and radical species in solution through the reaction of F^- with PCBM (or C_{60}) would result in a variety of new chemical species in deposited thin films. As has been shown in mechanochemical reactions of fullerenes in the solid state, anionic C_{60} species formed via reactions with nucleophiles are highly reactive and can form numerous products such as dimers and

cross-linked fullerene films.[18,28] To explore this, the PCBM / TBAF reaction solution was condensed and extracted with tetrachloroethylene to isolate crude products from the TBAF salt. Thin films were drop cast onto KBr substrates and analyzed via FTIR under airfree conditions. Figure 6.5 shows the PCBM / TBAF reaction products as compared to pristine PCBM. Most notable is the appearance of two large peaks at ~1662 cm^{-1} and 1632 cm^{-1} and a smaller peak at 1550 cm^{-1}. Two new peaks are also observed at ~3365 cm^{-1} and ~3200 cm^{-1}. FTIR spectra were also taken of the reaction mixtures of C_{60} / TBAF, PCBM / TBAF, as well as a TBAF control (Appendix C). Interestingly, the C_{60} / TBAF mixture shows the same new features as PCBM despite the observed difference in reactivity.

While it is difficult to positively identify reaction products from such a mixture, the 3365 cm^{-1} and 3200 cm^{-1} peaks are characteristic of hydrogen bonded OH functional groups. The 1665 cm^{-1}, 1632 cm^{-1}, and 1550 cm^{-1} peaks are in the range of C=O / C=N and C=C bond stretching. It has been observed by Wrzyszczynski et al. that photogenerated radical anions in the presence of tetrabutylammonium cations can undergo a 'Hofmann-like' elimination reaction resulting in tributylamine and 1-butene.[34] Such elimination reactions are also well documented for TBAF near room temperature.[31,35] The presence of such species in solution or the solid state can lead to numerous free radical reactions with fullerenes.[28] Wang et al. has also reported on the unusual C-N bond cleavage when C_{60} is reacted with triethylamine.[36] The formation of numerous reaction products would potentially result in the formation of sources of free radicals or charge carrier traps as observed by Duan et al. when analyzing interactions of amine functionalized fullerenes and polymers with an OPV active layer.[10]

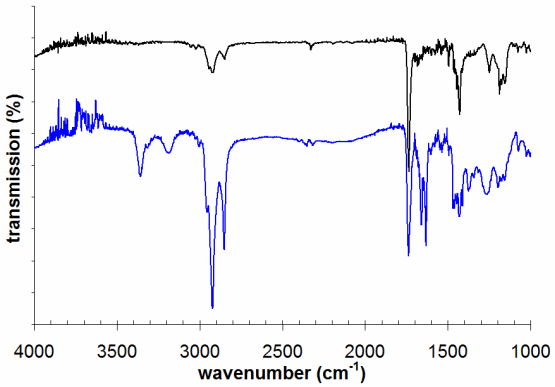

Figure 6.5. FTIR spectra of PCBM film (top) and PCBM / TBAF crude product film (bottom) cast on KBr and measured under airfree conditions. Spectra are offset for clarity.

6.1. Conclusions

In summary, we have demonstrated that the formation of C_{60} radical anions ($C_{60}^{\bullet -}$) is the result of an initial chemical reaction between the nucleophile (F^- or OH^-) with C_{60}, followed by electron transfer to a second fullerene molecule. This is opposed to the direct electron transfer mechanism proposed by Li et al. While other anions reported by Li et al. (i.e. Br^-, I^-, AcO^-) were not studied in this report, it is possible that similar reaction chemistry is occurring, as has been reported elsewhere for the reaction of OH^- with C_{60}.[15,17,18] Although anions such as I^- and Br^- do not display significant nucleophilic character, the extremely exergonic nature of direct electron transfer makes such a process extremely unlikely. The formation of nucleophilic and radical reaction intermediates has significant implications for carrier transport properties and energetics of deposited thin films, as well as exciting new possibilities for the rational design of n-doped materials and interfaces. The unusual reactivity observed upon condensation of

PCBM with TBAF provides valuable insight into potential reaction chemistry occurring during deposition of ionically functionalized fullerenes and polymers when utilized as electron-selective interlayers.

CHAPTER VII

CONCLUDING SUMMARY

In conclusion, this work has demonstrated the significant impact of ionic functionality on the charge injection processes in conjugated polymers and fullerenes. In particular, it has been shown that:

1. Ionic functionality can be used to control the spatial doping profile in bilayer structures of polyacteylene CPEs to fabricate an organic p-n junction. The ability to create n- and p-type regions via the formation of internally compensated states through the selective charge injection and counterion expulsion sequence presented in Chapter II has not been presented previously in the literature and provides a method to control the doping of CPE layers in more complicated device structures.
2. Ionic functionality has a dramatic effect on the photooxidative stability of polyacetylene and polythiophene CPE thin films as well as specific reaction pathways with respect to chemical charge injection from molecular oxygen. The work presented in Chapters III and IV also provides significant insight into the photooxidation mechanisms at work in neutral conjugated polymers, as ionic intermediates, such as the polymer-oxygen CTC, are common to many proposed oxidation schemes in the literature. Furthermore, the ability to control oxygen reaction pathways using ionically stabilized intermediates offers new possibilities

for other applications such as oxygen reduction reactions or photosensitization of singlet oxygen, both of which are areas of intense current research.

3. Ionic functionality has a significant impact on the interfacial charge injection properties of functional OPVs, in particular, leading to an increase in the cell open-circuit voltage and decrease in series resistance. As was shown in Chapter V, the increase in cell open-circuit voltage is likely the result of the work function decrease of the cationically functionalized fullerene interlayer. It is postulated that this decrease in work function is the result of the n-doping of the NMFP-Br layer by Br^- counterions as suggested by other groups. To further explore this doping mechanism, Chapter VI presented a study of the chemical reaction of tetrabutylammonium fluoride with C_{60} and PCBM in solution. It was shown that the source of the C_{60} radical anion (n-doped fullerene) was the result of an initial chemical reaction between the F^- or OH^- anion followed by electron transfer to a second C_{60} molecule, and not a simple 1-electron reduction. Based on these results, it is likely that similar solid state reactions are occurring in the case of NMFP-Br thin films, resulting in the generation of excess charge carriers and the observed high conductivity and increased device performance.

The work presented in this dissertation provides some initial insight into the fundamental chemistry occurring in ionically functionalized conjugated polymers and fullerenes, however, further research is required to elucidate the precise reaction mechanisms and interactions toward the rational design of functional organic electronic devices. This work provides a stepping stone for further research based on the

understanding of the general mechanistic schemes associated with the charge injection processes in the particular conditions presented. As the specific chemical reaction mechanism and kinetics will be dependant on the nature of the application and device structure, the data and conclusions presented here provide a general framework toward the further understanding of charge injection processes in conjugated materials and organic electronic devices.

APPENDIX A

SUPPORTING INFORMATION TO CHAPTER III

A.1. XPS Analysis

XPS analysis was performed using a ThermoScientific ESCALAB 250 spectrometer at a pass energy of 150eV for survey scans, using a monochromatized Al x-ray source with a 500□m spot size. Analyses were conducted on $TMAPA_A$ and $NaPA_A$ films drop cast from solution onto glass substrates. Three random sample spots were analyzed per sample and showed nearly identical results. The lack of any detectable fluoride peak was used to determine the lack of residual triflate anions in the $NaPA_A$ film.

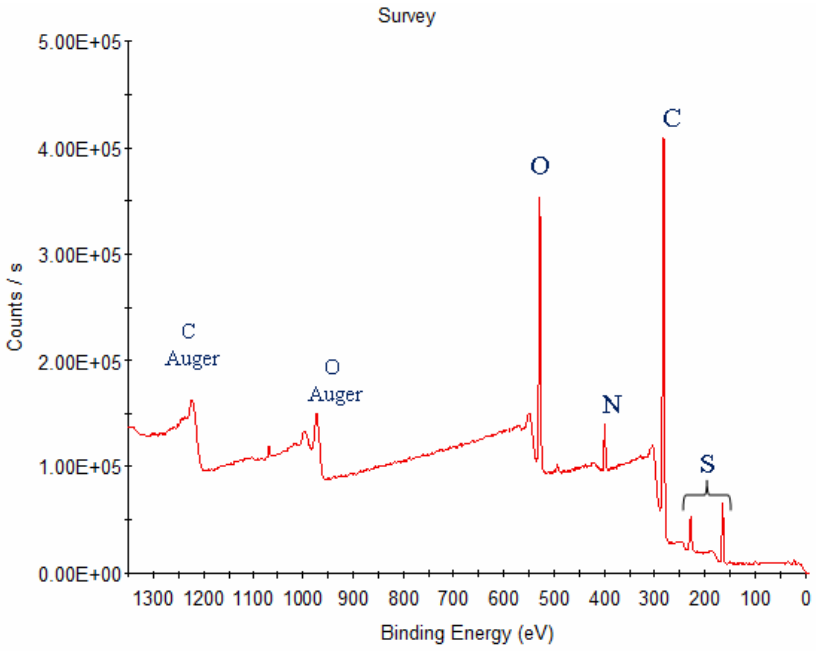

Figure A.1. XPS spectrum of $TMAPA_A$ film.

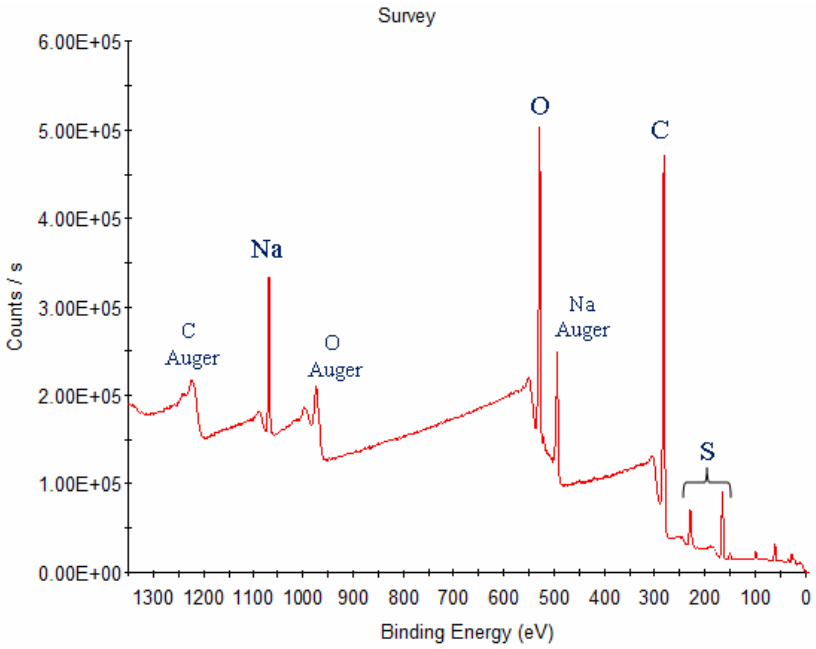

Figure A.2. XPS spectrum of $NaPA_A$ film

A.2. AFM Analysis

AFM analyses were performed using a Digital Instruments Multimode AFM in tapping mode. Samples were spray cast onto glass substrates with a thickness of ~75nm. The sample was analyzed before and after ion exchange to the sodium salt. Three random locations on were analyzed and displayed consistent feature sizes and roughness.

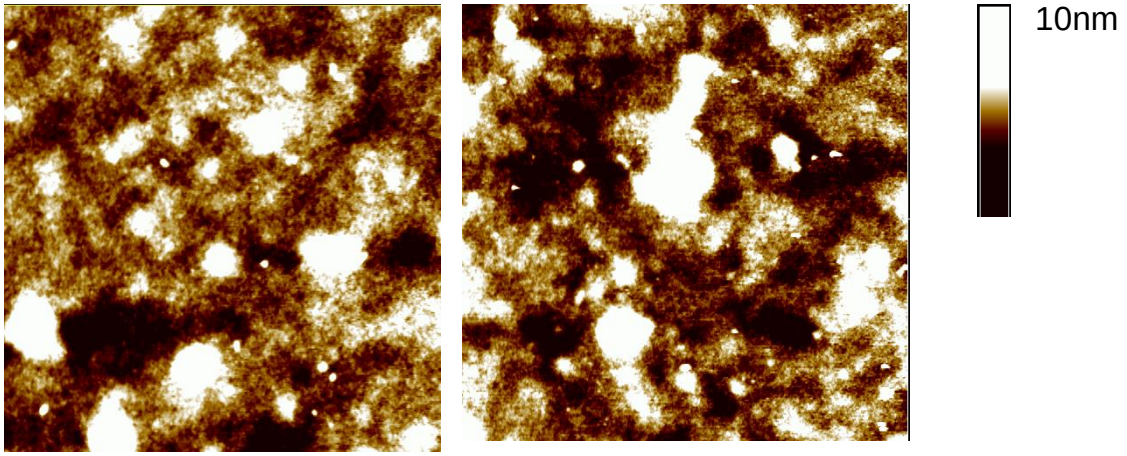

Figure A.3. AFM images of $TMAPA_A$ film before ion exchange (left) and after exchange to the sodium salt (right). Both films had a RMS roughness value of ~1.2nm.

A.3. UV-vis-NIR Spectroscopy

UV-vis-NIR spectroscopy was performed using a Perkin Elmer Lambda 1050 spectrometer. Samples were cast onto glass substrates via spray casting or spin coating with a thickness of ~50-100nm as determined by stylus profilometry. The absorbance in the visual range was used to monitor the degradation of the CTC to degradation products.

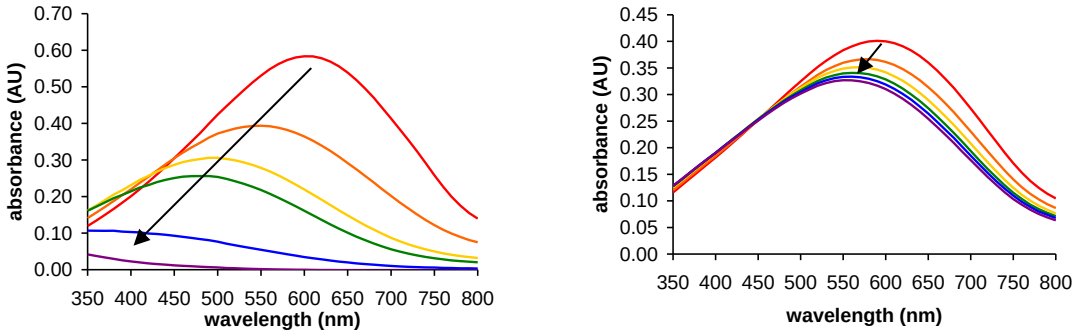

Figure A.4. Visual absorbance changes of $TMAPA_A$ (left) and $NaPA_A$ (right) films monitored over a period of 5 days. Each plot represents a period of 24hrs. Samples were continuously exposed to photo-oxidative conditions.

A.4. FTIR Spectroscopy

FTIR spectra were recorded using a Nicolet Magna-IR 560 spectrometer at 16 scans with a 2 cm^{-1} resolution.

A.5. Thin Film Preparation

$TMAPA_A$ thin films were cast via spray casting using a commercial airbrush (Badger) with an N_2 propellant at ~15psi. 5□L of polymer solution was inserted into the brush and sprayed at a distance of ~5cm from the substrate using ~0.5s pulse. Substrates were cleaned by soaking in conc HCl for 24hrs followed by rinsing with copious amounts of H_2O, MeOH, IPA, acetone and dried under a N_2 stream. Films were placed in vacuum for ~12hrs before ion exchange followed by another ~12 hrs under vacuum to remove

residual solvent. Film thicknesses were determined via stylus or optical profilometry using a Veeco Dektak 6M stylus Profiler or Zygo NewView 7300 optical profilometer.

A.6. Photo-oxidation Experiments

Photo-oxidation of thin films and aqueous solutions was performed by placing samples under a fluorescent light fixture composed of 2, 20W full spectrum grow lamps (Agrobrite) at a distance of ~22 inches. Room temperature was maintained at ~22^{o}C and humidity was not controlled. Light intensity was determined using a ThorLabs PM100D thermopile power meter positioned at the level of the samples.

APPENDIX B

SUPPORTING INFORMATION TO CHAPTER IV

B.1. Polymer Synthesis

B.1.1. Experimental Details

All reactions were carried out under an atmosphere of nitrogen unless otherwise stated. ^{1}H NMR and ^{13}C NMR were recorded on a Varian-600 MHz NMR spectrometer. The compounds 3-(6-bromohexyl)thiophene and 2,5-bis(4,4,5,5-tetramethyl-1,3,2-dioxaborolan-2-yl)thiophene were synthesized as describe previously.[1,2] GPC analysis was conducted with a Waters GPC containing a refractive index detector using a Waters Styragel HR4 column calibrated with sodium polystyrene sulfonate standards with a molecular weight range of 5000 to 60000 Da. GPC mobile phase was 75%DMSO / 25% H_2O / 0.1M $LiNO_3$.

B.1.2. Synthesis of tetramethylammonium 6-(2,5-dibromo-3-thienyl)hexanesulfonate

3-(6-Bromohexyl)thiophene (8.4g, 21 mmol) and sodium sulfite (5.2g, 41 mmol) in a water (40 mL) acetone (40 mL) solution was heated to a vigorous reflux for 65 hours turning from a cloudy to a clear and colorless solution. The solvent was removed *in*

vacuo giving a white solid. The solid was dissolved in a minimum of hot water, and on cooling a sticky white solid precipitated. The water layer was removed and the product washed with a small amount of cold water. The product was then ion exchanged to the tetramethylammonium salt using a cation exchange column. After drying the solid was dissolved in $CHCl_3$, filtered and then precipitated out by addition of hexanes, giving after drying a white solid (7.75g, 17 mmol, 78%).

^{1}H NMR (600 MHz, $CDCl_3$) δ 6.94 (s, 1H), 3.20 (s, 12H), 2.78 (2H, m), 2.55 (2H, t, *J* = *8* Hz), 1.79 (2H, m), 1.59 (2H, quin, *J* = 7Hz), 1.46 (2H, quin, *J* = 8 Hz), 1.36 (2H, quin, *J* = 8 Hz). ^{13}C NMR (151 MHz, $CDCl_3$) δ142.95, 131.05, 110.43, 108.06, 55.63, 52.23, 29.50, 29.48, 28.92, 28.78, 25.46.

B.1.3. Synthesis of Poly(6-(2,5-dibromo-3-thienyl)hexanesulfonate)

$Pd(PPh_3)_4$ (340 mg, 0.29 mmol) was added to a solution of tetramethylammonium 6-(2,5-dibromo-3-thienyl)hexanesulfonate (2.85g, 5.9 mmol), 2,5-bis(4,4,5,5-tetramethyl-1,3,2-dioxaborolan-2-yl)thiophene (1.99g, 5.9 mmol) and K_2CO_3 (3.27g, 23.7 mmol) in a nitrogen purged toluene (20 mL) water (30 mL) mixture, and the solution was heated to a reflux for 65 hours. The reaction solution changed from a light yellow to a dark red. The solution was extracted between toluene and water (3x) till the aqueous wash was colorless. The combined aqueous layers were extracted with toluene (2x) until the toluene layer was colorless. The aqueous layer was then concentrated giving a reddish solid. The product was dissolved in a minimum of water and re-precipitated with methanol (10x) giving after drying a reddish powder (1.42g, 66%). A portion was ion-

exchanged to give the tetramethylammonium salt. This was washed by dissolving in methanol and re-precipitating with acetonitrile (3x). The product was then washed with acetonitrile (3x), and dried giving a red powder.

Potassium salt

^{1}H NMR (600 MHz, D_2O) δ 8.0-6.5 (brs, 3H), 3.2-2 (brs, 4H), 2.0-0.5 (brs, 8H).

Tetramethylammonium salt.

^{1}H NMR (600 MHz, MeOD) δ 8.0-6.5 (brs, 3H), 3.18 (s, 12H), 2.9-2.3 (brs, 4H), 2.0-1.5 (brs, 4H), 1.5-1.1 (brs, 4H).

GPC(75%DMSO, 25% 0.1M $LiNO_3$(aq)): M_w=27000 Da.

B.2. Supplementary Figures

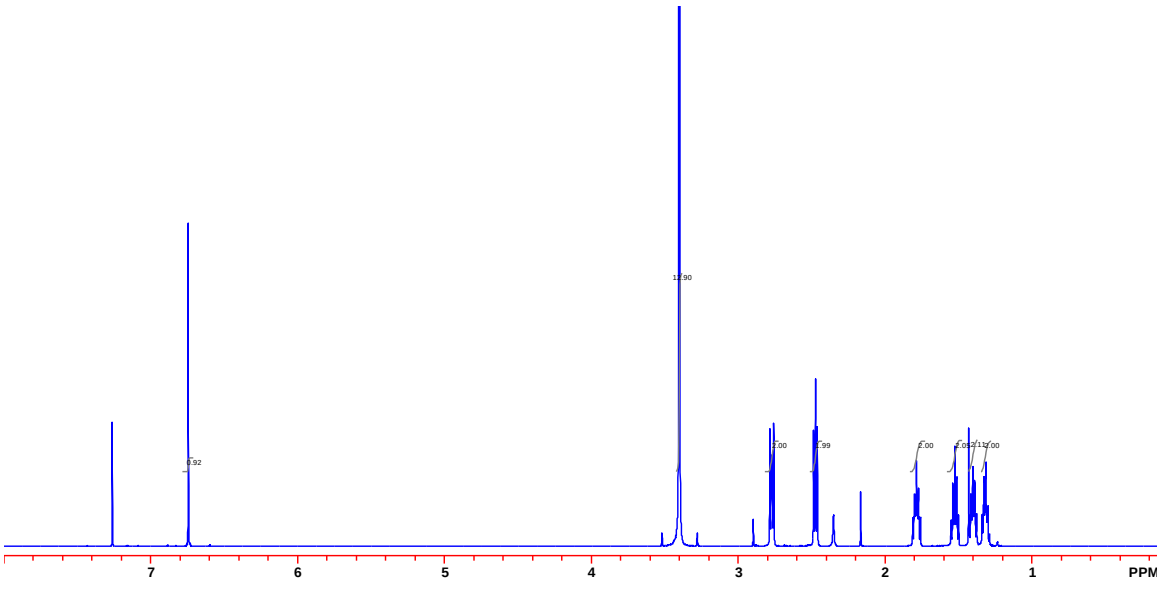

Figure B.1. ^{1}H NMR Tetramethylammonium 6-(2,5-dibromo-3-thienyl)hexanesulfonate

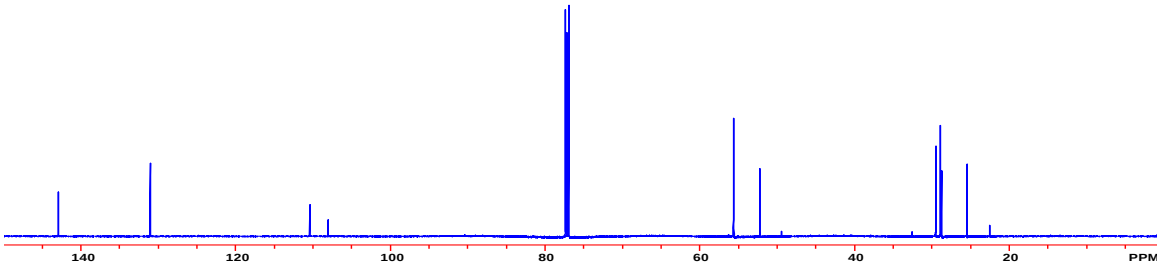

Figure B.2. ^{13}C NMR Tetramethylammonium 6-(2,5-dibromo-3-thienyl)hexanesulfonate

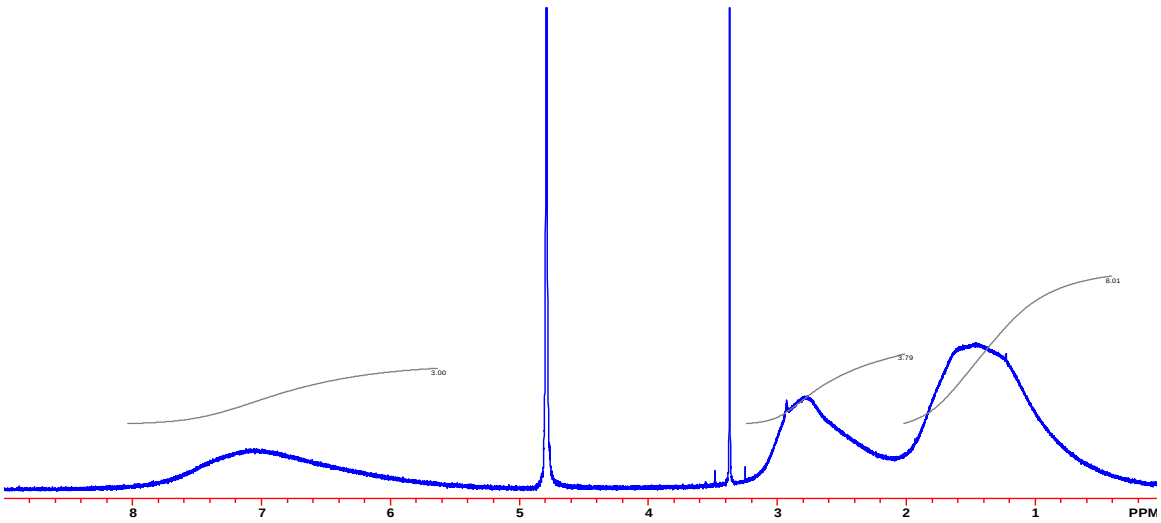

Figure B.3. ^{1}H NMR Potassium poly(6-(2,5-dibromo-3-thienyl)hexanesulfonate)

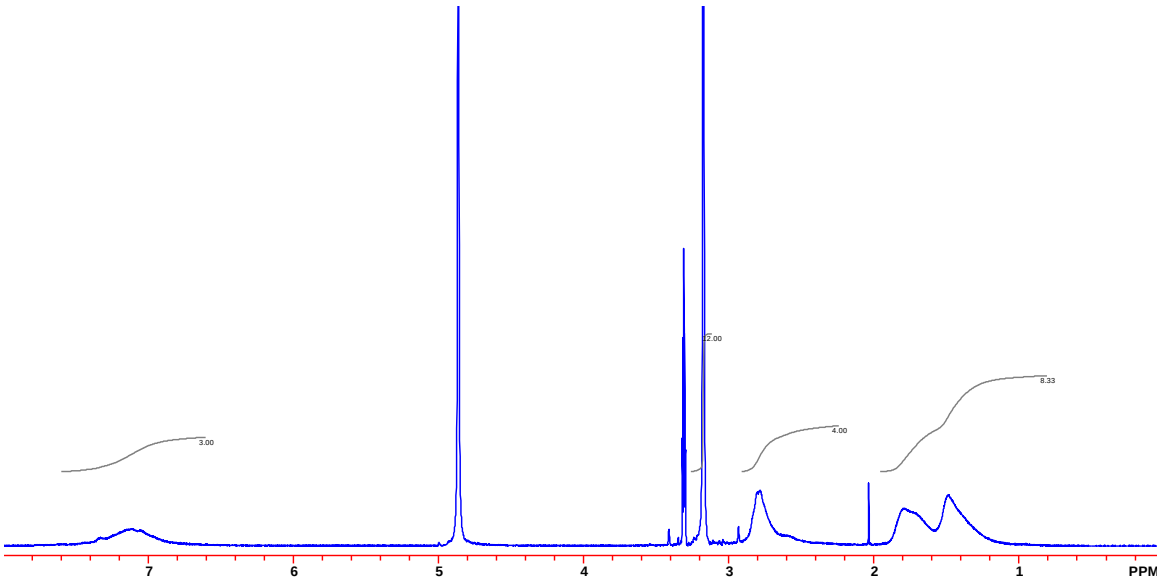

Figure B.4. ^{1}H NMR Tetramethylammonium poly(6-(2,5-dibromo-3-thienyl)hexanesulfonate)

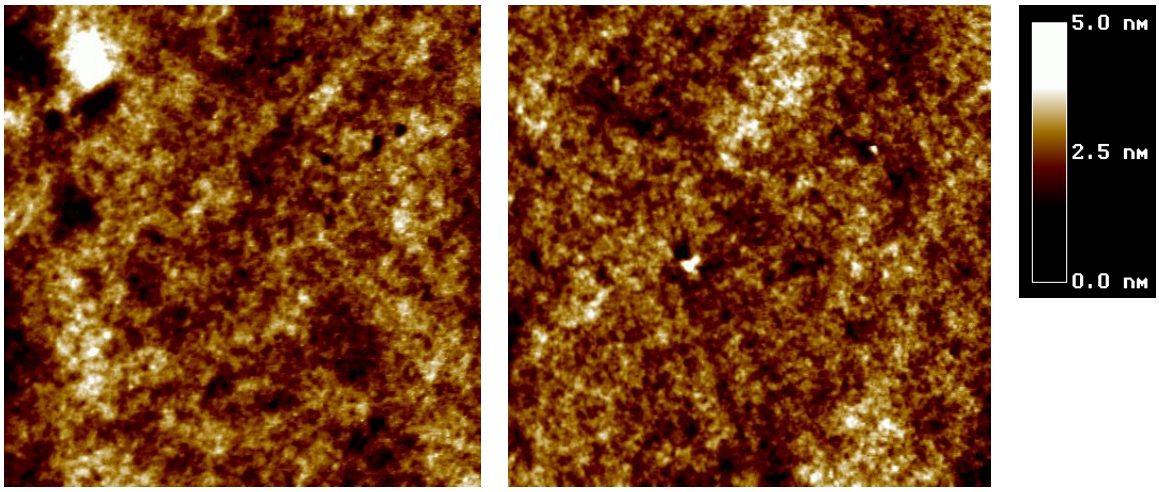

Figure B.5. AFM images of TMAPT film before (left) and after ion exchange to LiPT (right)

B.2.1. XPS Analysis

XPS analysis was performed using a ThermoScientific ESCALAB 250 spectrometer at a pass energy of 150eV for survey scans, using a monochromatized Al x-ray source with a 500μm spot size. Analyses were conducted on TMAPT films spun cast from solution onto glass substrates before and after exchange to LiPT. Three random sample spots were analyzed per sample and showed nearly identical results. The lack of any detectable fluoride peak was used to determine the lack of residual triflate anions in the LiPT film.

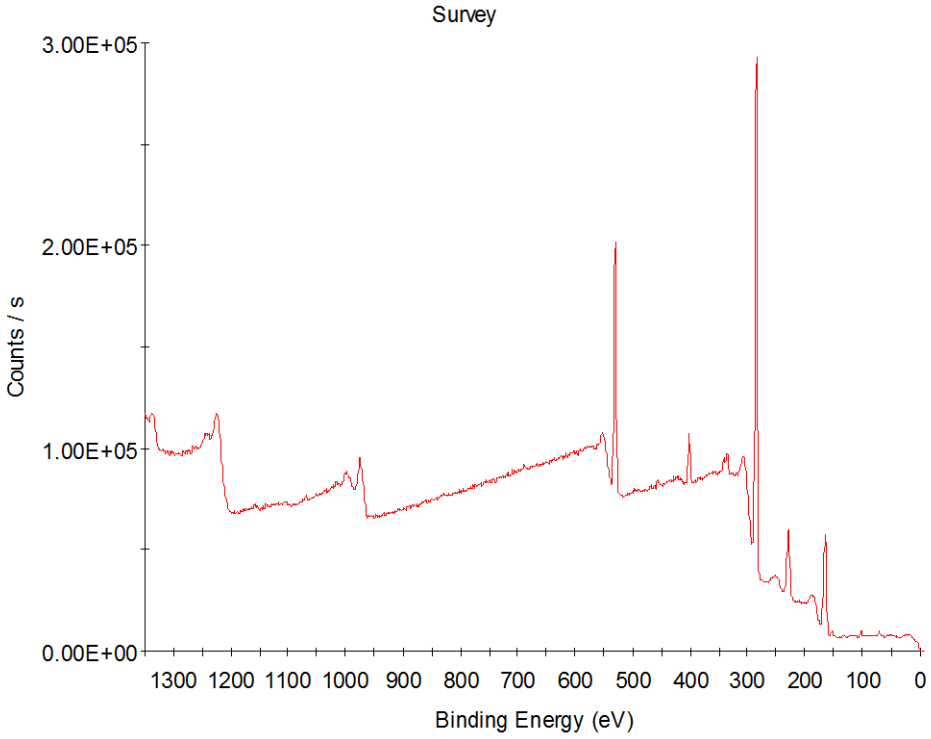

Figure B.6. XPS spectrum of TMAPT film before ion exchange. Note the N Peak at ~400eV.

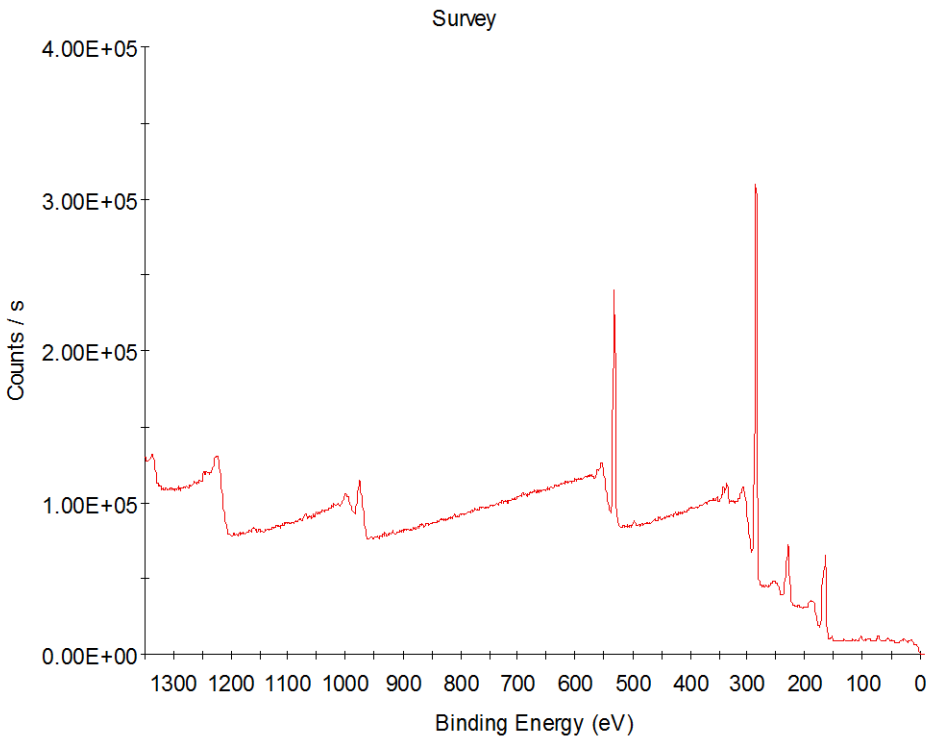

Figure B.7. XPS spectrum of LiPT film after ion exchange.

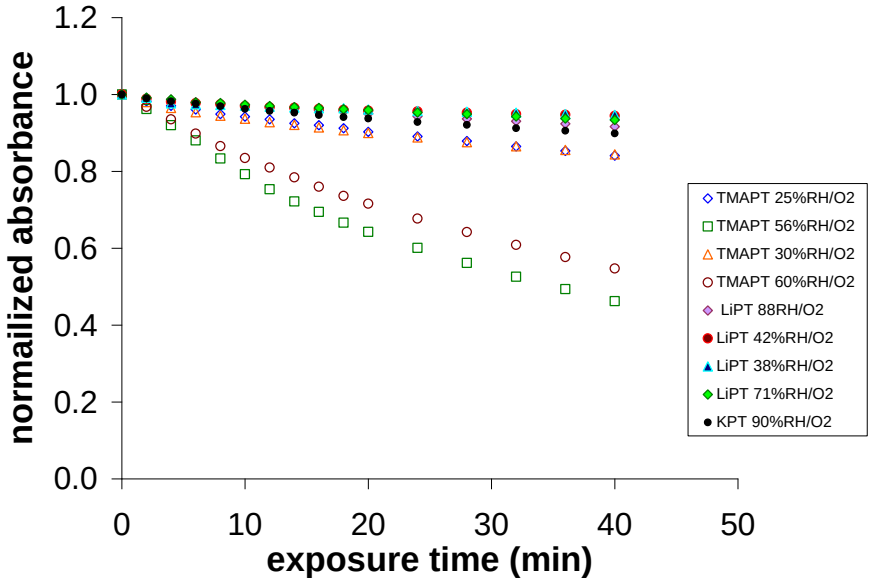

Figure B.8. Photobleaching of the initial λ_{max} (440nm) of TMA and MPT films under accelerated photooxidative conditions in low and high humidity oxygen (1atm).

B.2.2. FTIR Analysis

FTIR spectra were recorded using a Nicolet Magna-IR 560 spectrometer at 16 scans with a 2 cm^{-1} resolution.

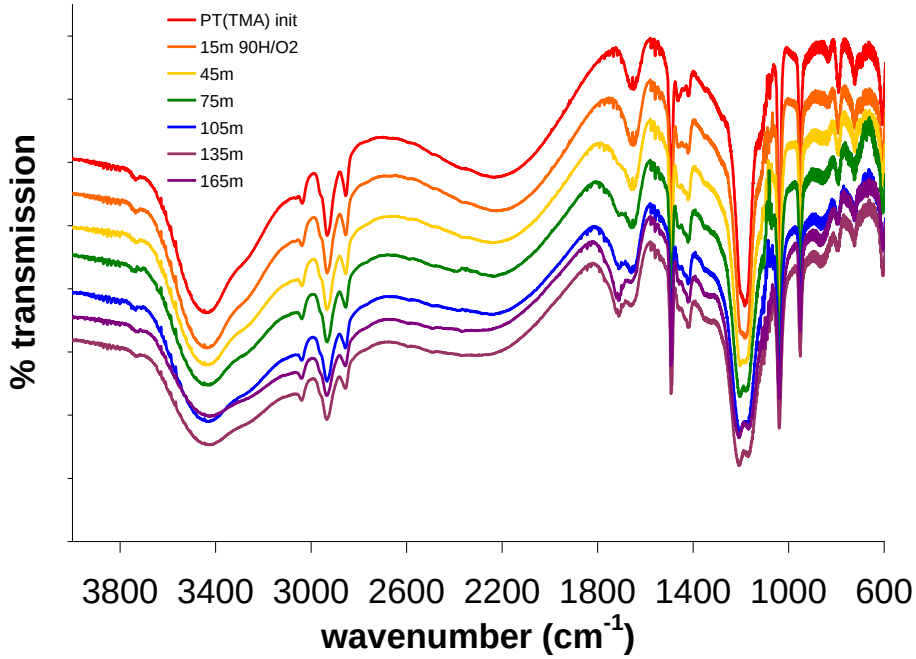

Figure B.9. FTIR spectra of TMAPT film under 90% RH oxygen (1atm) during photooxidation under accelrated conditions

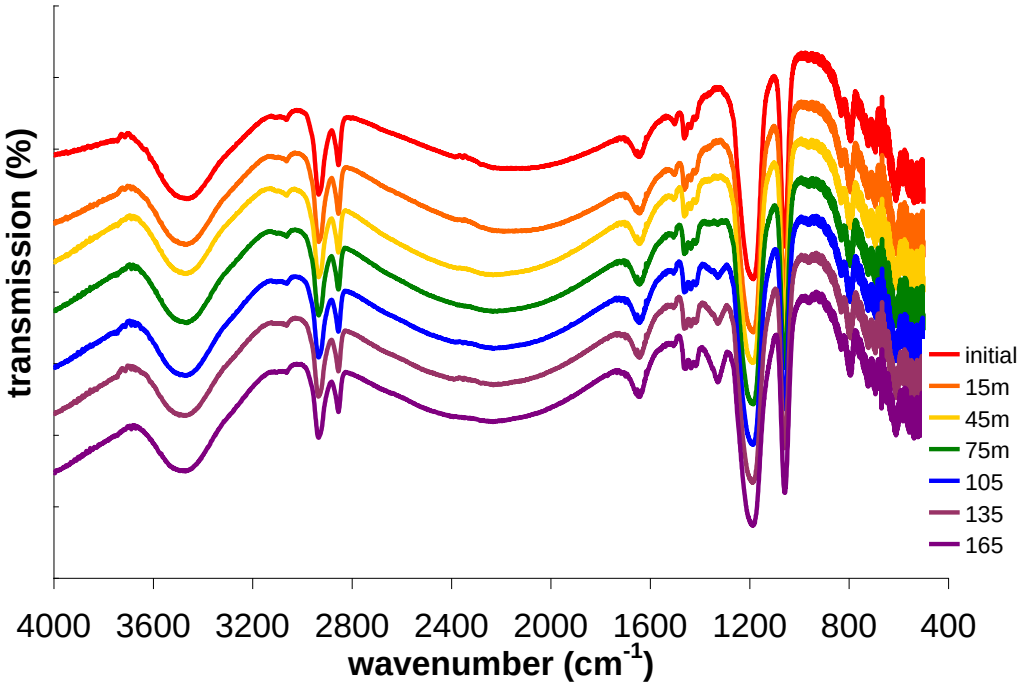

Figure B.10. FTIR spectra of LiPT film under 90% RH oxygen (1atm) during photooxidation under accelrated conditions

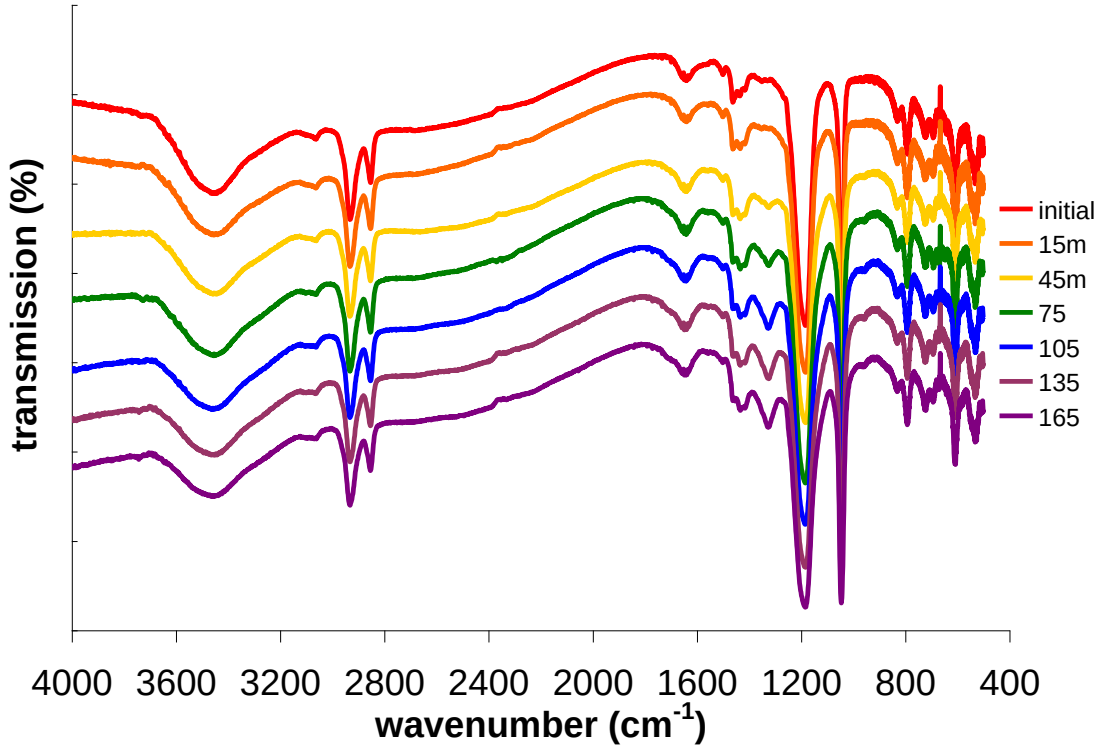

Figure B.11. FTIR spectra of KPT film under 90% RH oxygen (1atm) during photooxidation under accelrated conditions

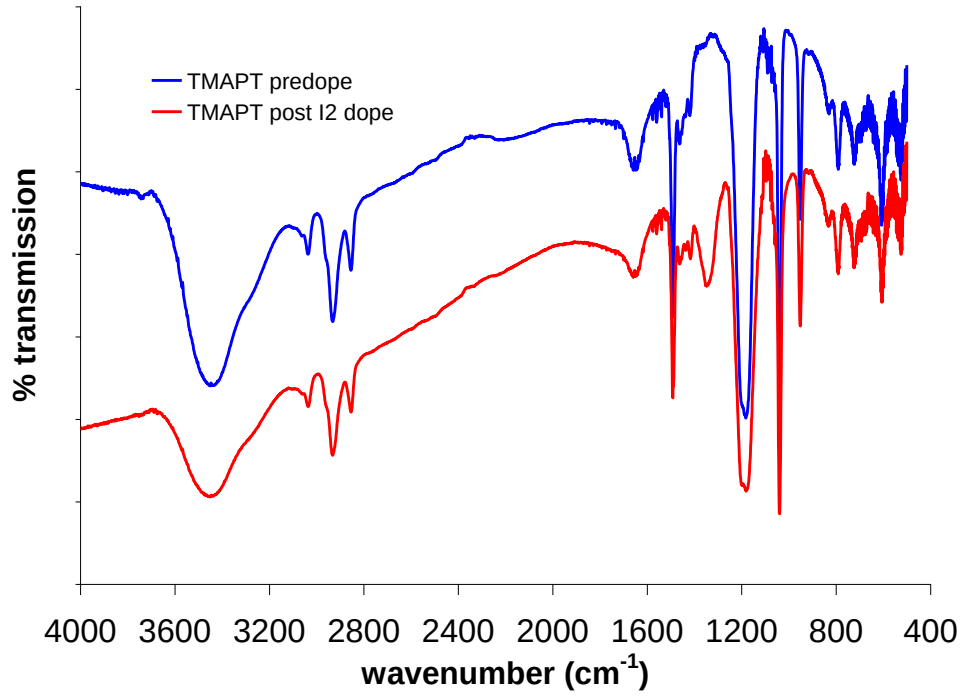

Figure B.12. FTIR spectra of TMAPT film before and after p-doping via exposure to iodine vapor (30m).

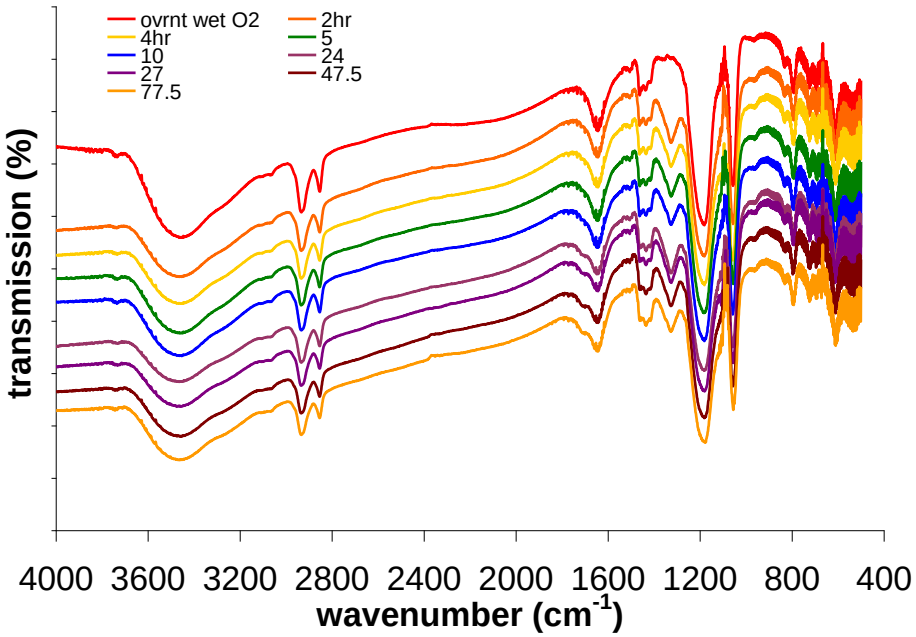

Figure B.13. FTIR spectra of long term photooxidation (90%RH O_2) of LiPT film using high intensity tungsten light source.

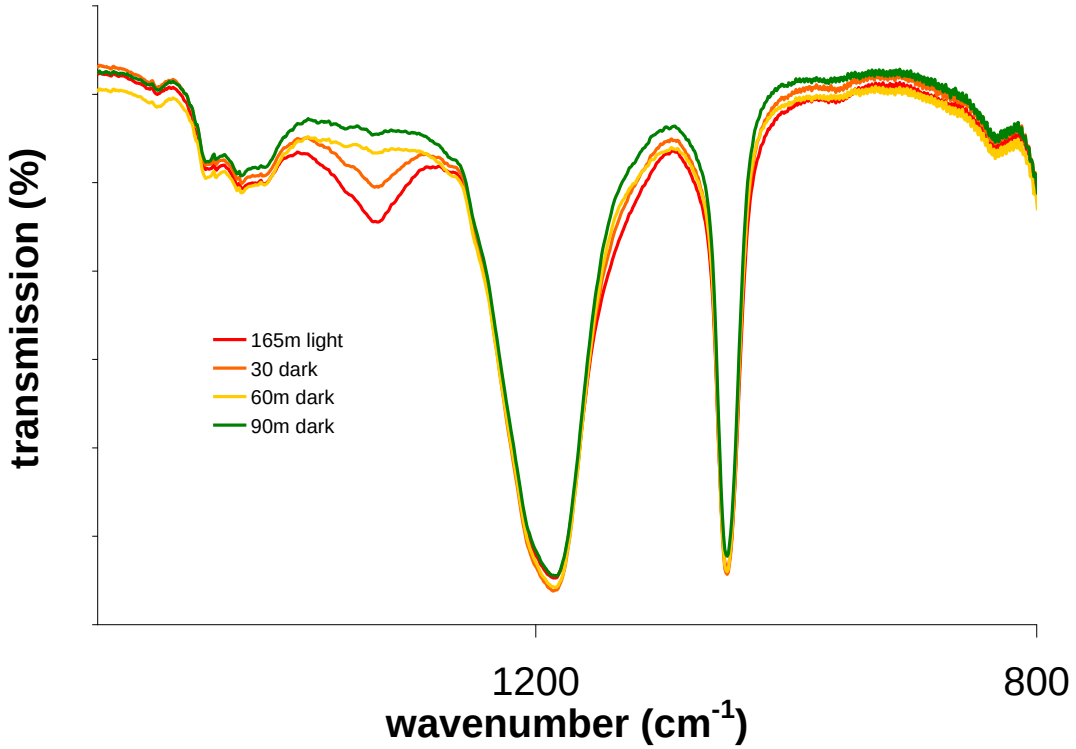

Figure B.14. FTIR spectra showing the reversal of the doping peak at 1333 cm^{-1} when stored in humid oxygen (90%RH) in the dark.

APPENDIX C

SUPPORTING INFORMATION TO CHAPTER VI

C.1. Materials and experimental procedures

C.1.1. UV-vis-NIR spectroscopy

Spectroscopic experiments were performed on a Perkin Elmer Lambda 1050 spectrometer. Ortho-dichlorobenzene (o-DCB) solutions were prepared from 99 % anhydrous o-DCB (Sigma Aldrich) and deoxygenated via freeze-pump-thaw method. 0.5 mM solutions of C_{60} were prepared from C_{60} (99.5 %, SES Research) and deoxygenated o-DCB. Solutions were subsequently deoxygenated to remove any O_2 introduced during transfer. Spectroscopy of solutions was carried out using a custom designed airfree cuvette. Equivalents of tetrabutylammonium fluoride trihydrate (Fluka) were added to the cell as solid prior to introduction of C_{60} solution under N_2. PCBM (99%, SES Research) solutions were prepared using deoxygenated CH_2Cl_2 (Omnisolv spectroscopic grade) under airfree conditions.

C.1.2. Electrochemistry

Electrochemical measurements were performed using a standard 3-electrode geometry with a glassy carbon working electrode, platinum coil counter electrode, and silver wire pseudo reference separated from the analyte solution via a vycor frit. Subsequent to experiments, the reference was calibrated versus ferrocene under identical conditions. Electrolyte solution was 0.1 M tetrabutylammonium tetrafluoroborate (Sigma

Aldrich) in deoxygenated o-DCB. All experiments were performed under airfree conditions (active N_2 atmosphere) and data collected using a custom designed potentiostat.

C.1.3. ^{19}F NMR

The ^{19}F NMR spectra were collected on a Bruker-Advance-III-HD 600MHz NMR spectrometer equipped with a 5mm Prodigy CryoProbe. The samples were prepared in 99.8% $CDCl_3$ (Cambridge Isotope Laboratories).

C.1.4. FTIR

FTIR experiments were performed using a Nicolet FTIR spectrometer. Thin films were cast onto KBr substrates under airfree conditions and measurements conducted under airfree conditions utilizing a custom design chamber equipped with CaF optical windows. Spectra were recorded at 2 cm^{-1} resolution for 16 scans.

C.2. Supplementary Figures

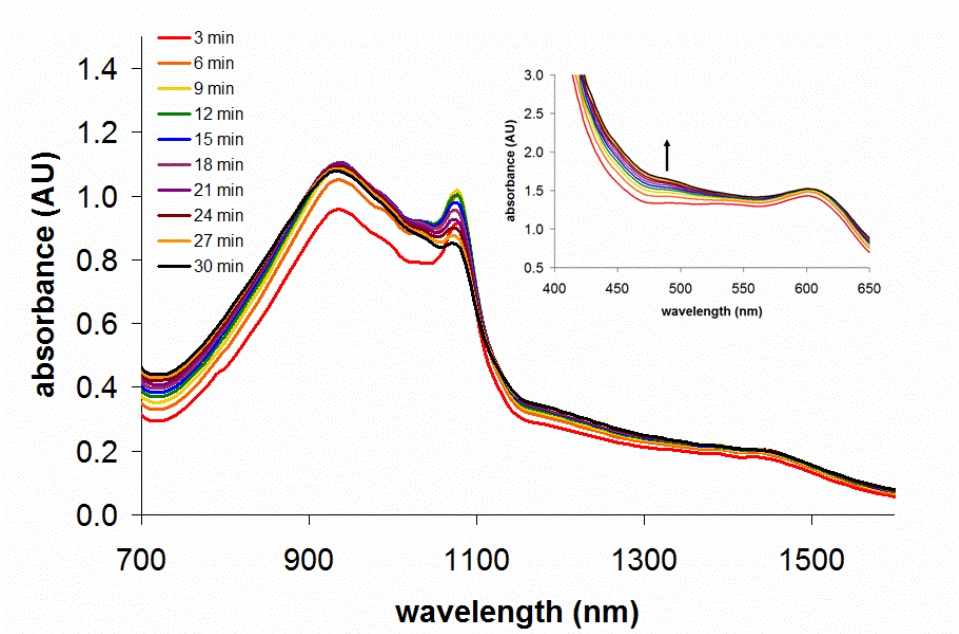

Figure C1. UV-vis-NIR time progression (180 s intervals) of 0.5 mM C_{60} solution with 4 eq TBAF. Inset shows high energy portion of the spectrum.

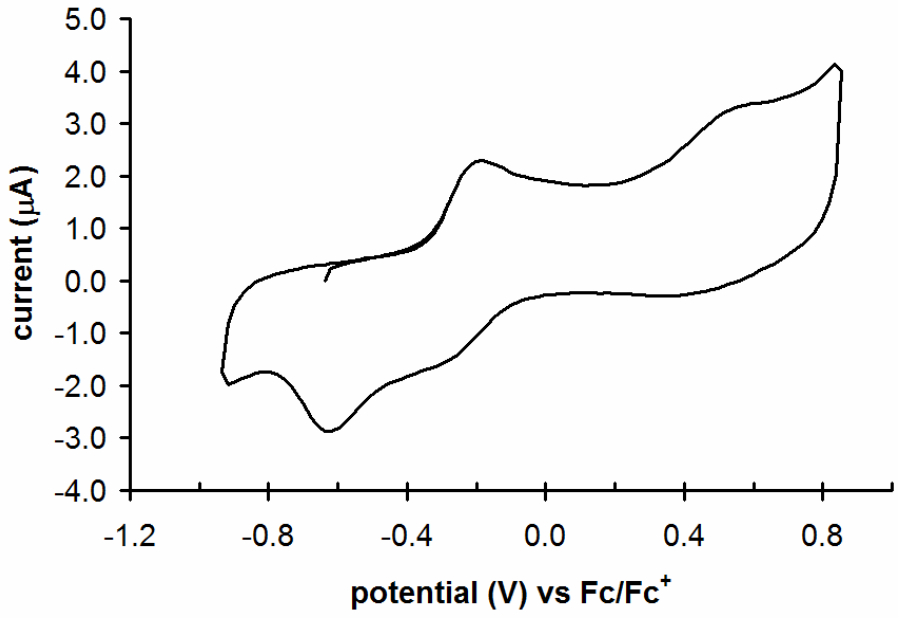

Figure C2. CV of crude product of PCBM / TBAF mixture after evaporation of solvent and re-dissolving in acetonitrile (0.1M $TBABF_4$).

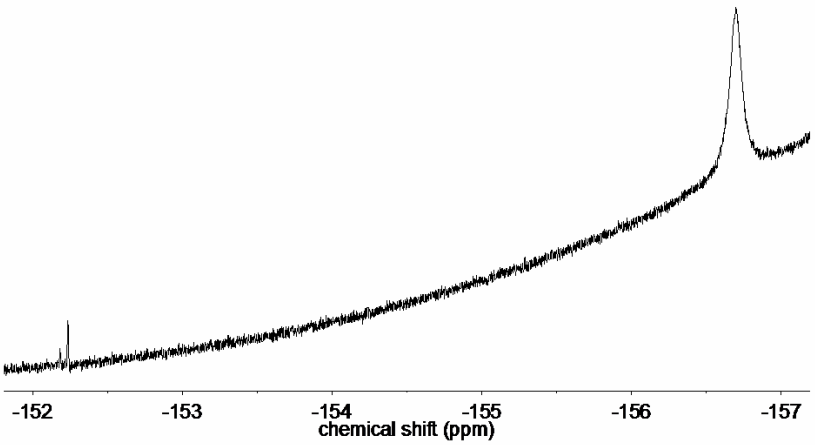

Figure C3. ^{19}F NMR of PCBM / TBAF (5 eq) solution after reaction by condensing solvent. The small peaks at ~152 ppm are assigned to FHF^- impurities detected in control spectra.

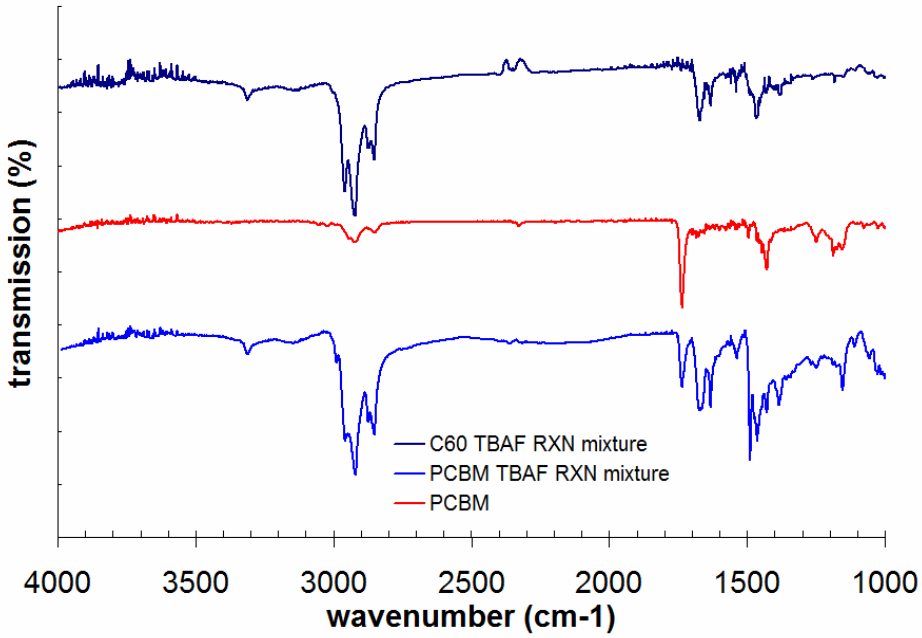

Figure C4. FTIR of C_{60} / TBAF (7 eq TBAF) reaction solution (top), PCBM control (middle), and PCBM / TBAF (5 eq TBAF) reaction solution (bottom).

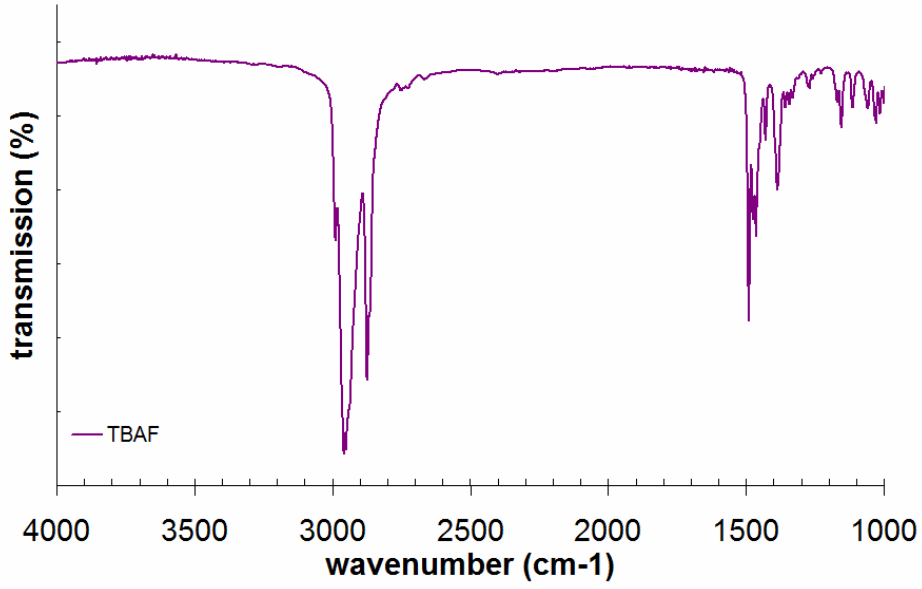

Figure C5. FTIR of TBAF film cast from CH_2Cl_2 onto KBR.

REFERENCES CITED

Chapter I

(1) Edman, L. *Electrichimica Acta,* **2005**, 50, 3878-3885.

(2) Newman, C. R.; Frisbie, C. B.; da Silva Filho, D. A.; Bredas, J. -L.; Ewbank, P. C.; Mann, K. R. *Chem. Mater.*, **2004**, 16, 4436-4451.

(3) McQuade, D. T.; Pullen, A. E.; Swager, T. M. *Chem. Rev.*, **2000**, 2537-2574.

(4) Li, G.; Zhu, R.; Yang, Y. *Nat. Photonics*, **2012**, 6, 153-161.

(5) Dennlen, G.; Scharber, M. C.; Brabec, C. J. *Adv. Mater*., **2009**, 21, 1323-1338.

(6) Zhou, H.; Yang, L.; You, W. *Macromolecules*, **2012**, 45, 607-632.

(7) Thompson, B. C.; Frechet, J. M. J. *Agnew. Chem. Int. Ed.*, **2008**, 47, 58-77.

(8) Bredas, J. -L.; Norton, J. E.; Cornil, J.; Coropceau, V. *Acc. Chem. Res.*, **2009**, 42, 1691-1699.

(9) Carle, J.E.; Krebs, F. C. *Sol. Eng. Mater. Sol. Cells*, **2013**, 119, 309-310.

(10) Jorgensen, M.; Carle, J. E.; Sondergaard, R. R.; Lauritzen, M.; Dagnaes-Hansen, N. A.; Byskov, S. L.; Andersen, T. R.; Larsen-Olsen, T. T.; Bottiger, A. P. L.; Andreasen, B.; Fu, L.; Zuo, L.; Liu, Y.; Bundgaard, E.; Zhan, X.; Chen, H.; Krebs, F. C. *Sol. Eng. Mater. Sol. Cells*, **2013**, 119, 84-93.

(11) http://www.nrel.gov/ncpv/images/efficiency_chart.jpg.

(12) L. Echegoyen, F. Diederich and L. E. Echegoyen, in *Fullerenes: Chemistry,Physics, and Technology*, ed. K. M. Kadish and R. S. Ruoff, Wiley-Interscience, USA, 2000.

(13) W. R. Salaneck, I. Lundstrom, and B. Ranby, in *Conjugated Polymers and Related Materials: The Interconnection of Chemical and Electronic Structure*, Oxford Press, Oxford, 1993.

(14) Yip, H. -L.; Jen, A. K.-Y. *Energy Environ. Sci*., **2012**, 2, 5994-6011.

(15) Yang, T.; Wang, M.; Duan, C.; Hu, X.; Huang, L.; Peng, J.; Huang, F.; Gong, X. *Energy Environ. Sci*., **2012**, 5, 8202-8214.

(16) Li, C. -Z.; Chueh, C. -C.; Yip, H. -L.; O'Malley, K. M.; Chen, W. -C.; Jen, A. K. -Y. *J. Mater . Chem*., **2012**, 22, 8574-8577.

(17) He, Z.; Zhong, C.; Su, S.; Xu, M.; Cao, Y. *Nat. Photonics*, **2012**, 6, 591-595.

(18) Na, S. -I.; Kim, T. -S.; Oh, S. -S.; Kim, J.; Kim, D. -Y. *Appl. Phys. Lett.*, **2010**, 223305.

(19) Li, S. -S.; Chen, C. -W. *J. Mater. Chem. A.*, **2013**, 1, 10574-10591.

(20) Peet, J.; Heeger, A. J.; Bazan, G. C. *Acc. Chem. Res.*, **2009**, 42, 1700-1708.

(21) Clarke, T. M.; Durrant, J. R. *Chem. Rev.*, **2010**, 110, 6736-6767.

(22) C. Brabec, V. Dyakonov, J. Parisi, and N. S. Sariciftci, in *Organic Photovoltaics: Concepts and Realization*, Springer, Berlin, 2003.

(23) Brabec, C. J. *Sol. Eng. Mater. Sol. Cells*, **2004**, 83, 273-292.

(24) Qi, B.; Wang, J. *J. Mater. Chem.*, **2012**, 22, 24315-24325.

(25) Ratcliff, E. L.; Garcia, A.; Paniagua, S. A.; Cowen, S. R.; Giordano, A. J.; Ginley, D. S.; Marder, S. R.; Berry, J. J.; Olsen, D. C. *Adv. Energy Mater.*, **2013**, 3, 647-656.

(26) Cowan, S. R.; Roy, A.; Heeger, A. J.; *Phys. Rev. B.*, **2010**, 82, 245207.

(27) Credgington, D.; Hamilton, R.; Atienzar, P.; Nelson, J.; Durrant, J. *Adv. Func. Mater.*, **2011**, 21, 2744-2753.

(28) Garcia-Belmonte, G.; Munar, A.; Barea, E. M.; Bisquert, J.; Ugarte, I.; Pacios, R. *Org. Electronics*, **2008**, 9, 847-851.

(29) Qi, B.; Wang, J. *Phys. Chem. Chem. Phys.*, **2013**, 15, 8972-8982.

(30) MacDiarmid, A. G. *Reviews of Modern Physics*, **2001**, 73, 701-712.

(31) Bredas, J. -L.; Street, G. B. *Acc. Chem. Res.*, **1985**, 18, 309-315.

(32) Etemad, S.; Heeger, A. J.; MacDiarmid, A. G. *Ann. Rev. Phys. Chem.*, **1982**, 33, 443-469.

(33) M. S. Freund and B. Deore, in *Self-Doped Conducting Polymers*, John Wiley and Sons, England, 2007.

(34) Duarte, A.; Pu, K. -Y.; Liu, B.; Bazan, G. C. *Chem. Mater.*, **2011**, 23, 501-515.

(35) Frohne, H.; Shaheen, S. E.; Brabec, C. J.; Muller, D. C.; Sariciftci, S.; Meerholz, K. *ChemPhysChem*, **2002**, 9, 795-799.

(36) Brabec, C. J.; Shaheen, S. E.; Winder, C.; Sariciftci, N. S. *Appl. Phys. Lett.*, **2002**, 80, 1288.

(37) Gu, C.; Zhang, Z.; Sun, S.; Pan, Y.; Zhong, C.; Lu, Y.; Li, M.; Ariga, K.; Huang, F.; Ma, Y. *Adv. Mater.*, **2012**, 24, 5727-5731.

(38) Wang, D.; Hasegawa, S.; Shimizu, M.; Tanaka, S. J. *Synth. Met.*, **1992**, 46, 85-91.

(39) Pochan, J. M.; Pochan, D. F.; Rommelmann, H.; Gibson, H. W. *Macromolecules* **1981**, *14*, 110.

(40) Gibson, H. W.; Pochan, J. M. *Macromolecules* **1982**, *15*, 242.

(41) Sarkas, H. W.; Kwan, W.; Flom, S. R.; Merritt, C. D.; Kafafi, Z. H. *J. Phys. Chem.* **1996**, *100*, 5169.

(42) Hintz, H.; Egelhaaf, H. J.; Luer, L.; Hauch, J.; Peisert, H.; Chasse, T. *Chem. Mater.* **2011**, *23*, 145.

(43) Lee, J. U.; Jung, J. W.; Jo, J. W.; Jo, W. H. *J. Mater. Chem.*, **2012**, 22, 24265-24283.

(44) Toumebize, A.; Bussiere, P. -O.; Rivaton, A.; Gardette, J. -L.; Medlej, H.; Hiorns, R. C.; Dagron-Larigau, C.; Krebs, F. C.; Norman, K. *Chem. Mater.*, **2013**, ASAP.

(45) Xing, K. Z.; Johansson, N.; Beamson, G.; Clark, D. T.; Bredas, J. -L.; Salaneck, W. R. *Adv. Mater.*, **1997**, 9, 1027-1031.

(46) Dupuis, A.; Wong-Wah-Chung, P.; Rivaton, A.; Gardette, J. -L. *Polymer Degradation and Stability*, **2012**, 97, 366-374.

(47) Scurlock, R. D.; Wang, B.; Ogilby, P. R.; Sheats, J. R.; Clough, R. L. *J. Am. Chem. Soc.*, **1995**, 117, 10194-10202.

(48) Zhuo, J. M.; Zhao, L. H.; Png, R. Q.; Wong, L. Y.; Chia, P. J.; Tang, J. C.; Sivaramakrishnan, S.; Zhou, M.; Ou, E. C. W.; Chua, S. J.; Sim, W. S.; Chua, L. L.; Ho, P. K. H. *Adv. Mater.*, **2009,** *21*, 4747-4752.

(49) Arroyo-Villan, M. I.; Diazquijada, G. A.; Abdou, M. S. A.; Holdcroft, S. *Macromolecules*, **1995,** *28*, 975-984.

(50) Tran-Van, F.; Carrier, M.; Chevrot, C. *Synth. Met.*, **2004,** *142*, 251-258.

(51) Park, S. -J.; Gesquiere, A. J.; Yu, J.; Barbara, P. F. *J. Am. Chem. Soc.*, **2004**, 126, 4116.

(52) Walker, E. M.; Lonergan, M. C. *J. Phys. Chem. C.*, **2013**, 117, 14929-14938.

(53) Xu, Z.; Chen, L. -M.; Chen, M.. -H.; Li, G.; Yang, Y. *Appl. Phys. Lett.*, **2009**, 95, 013301.

(54) Hsieh, C. -H.; Cheng, Y. -J.; Li, P. -J.; Dubosc, M.; Liang, R. -M.; Hsu, C. -S. *J. Am. Chem. Soc.*, **2010**, 132, 4887-4893.

(55) Cho, N.; Yip, H. -L.; Hau, S. K.; Chen, K. -S.; Kim, T. -W.; Davies, J. A.; Ziegler, D. F.; Jen, A. K. -Y. *J. Mater. Chem.*, **2011**, 21, 6956-6961.

(56) Barbot, A.; Lucas, B.; Bin, C. D.; Ratier, B.; Aldissi, M. *Appl. Phys. Lett.*, **2013**, 102, 193305.

(57) Li, C. -Z.; Chueh, C. -C.; Yip, H. -L.; Liang, P. -W.; Li, X.; Jen, A. K. -Y. *Adv. Mater.*, **2013**, 25, 4425-4430.

Chapter II

(1) Sze, S. M. *Semiconductor Devices Physics and Technology*; 2nd ed.; Wiley: New York, 2002.

(2) Buck, R. P.; Surridge, N. A.; Murray, R. W. *J. Electrochem. Soc.* **1992**, *139*, 136-144.

(3) Gao, J.; Yu, G.; Heeger, A. J. *Appl. Phys. Lett.* **1997**, *71*, 1293-1295.

(4) Gao, J.; Li, Y.; Yu, G.; Heeger, A. J. *J. Appl. Phys.* **1999**, *86*, 4594-4599.

(5) Yu, G.; Cao, Y.; Andersson, M.; Gao, J.; Heeger, A. J. *Adv. Mater.* **1998**, *10*, 385-388.

(6) Shin, J. H.; Xiao, S.; Fransson, A.; Edman, L. *Appl. Phys. Lett.* **2005**, *87*, 043506/1-043506/3.

(7) Leger, J. M.; Rodovsky, D. B.; Bartholomew, G. P. *Adv. Mater.* **2006**, *18*, 3130-3134.

(8) Leger, J. M.; Patel, D. G.; Rodovsky, D. B.; Bartholomew, G. P. *Adv. Funct. Mater* **2007**, *18*, 1212-1219.

(9) Nguyen, T. Q.; Schwartz, B. J. *Journal of Chemical Physics* **2002**, *116*, 8198-8208.

(10) Langsdorf, B. L.; Zhou, X.; Adler, D. H.; Lonergan, M. C. *Macromolecules* **1999**, *32*, 2796-2798.

(11) Jiang, H.; Taranekar, P.; Reynolds, J. R.; Schanze, K. S. *Angew. Chem. Int. Ed.* **2009**, *48*, 4300-4316.

(12) Cheng, C. H. W.; Lonergan, M. C. *J. Am. Chem. Soc.* **2004**, *126*, 10536-10537.

(13) Elliott, C. M.; Redepenning, J. G.; Balk, E. M. *J. Am. Chem. Soc.* **1985**, *107*, 8302-8304.

(14) Bauerle, P.; Gaudl, K. U.; Wurthner, F.; Sariciftci, N. S.; Neugebauer, H.; Mehring, M.; Zhong, C. J.; Doblhofer, K. *Adv. Mater.* **1990**, *2*, 490-494.

(15) Freund, M. S.; Deore, B. *Self-Doped Conducting Polymers*; Wiley: Hoboken, NJ., 2007.

(16) Gao, L.; Johnston, D.; Lonergan, M. C. *Macromolecules* **2008**, *41*, 4071-4080.

(17) Johnson, L. K.; Virgil, S. C.; Grubbs, R. H.; Ziller, J. W. *J. Am. Chem. Soc.* **1990**, *112*, 5384-5385.

(18) Dalton, E. F.; Surridge, N. A.; Jernigan, J. C.; Wilbourn, K. O.; Facci, J. S.; Murray, R. W. *Chem. Phys.* **1990**, *141*, 143-157.

(19) Doblhofer, K.; Rajeshwar, K. In *Handbook of Conducting Polymers*; 2nd ed.; Skotheim, T. A., Elsenbaumer, R. L., Reynolds, J. R., Eds.; Marcel Dekker: New York, 1998, p 531-588.

(20) Lonergan, M. C.; Cheng, C. H.; Langsdorf, B. L.; Zhou, X. *J. Am. Chem. Soc.* **2002**, *124*, 691-701.

(21) Buttry, D. A.; Ward, M. D. *Chemical Reviews* **1992**, *92*, 1355-1379.

Chapter III

(1) Jiang, H.; Taranekar, P.; Reynolds, J. R.; Schanze, K. S. *Angew. Chem., Int. Ed.* **2009**, *48*, 4300.

(2) Hoven, C. V.; Garcia, A.; Bazan, G. C.; Nguyen, T.-Q. *Adv. Mater.* **2008**, *20*, 3793.

(3) Duarte, A.; Pu, K. Y.; Liu, B.; Bazan, G. C. *Chem. Mater.* **2011**, *23*, 501.

(4) *Iontronics*; Leger, J. M.; Berggren, M.; Carter, S., Eds.; CRC Press: Boco, Raton, 2011.

(5) Pu, K. Y.; Liu, B. *Adv. Funct. Mater.* **2009**, *19*, 1371.

(6) Recksiedler, C. L.; Deore, B. A.; Freund, M. S. *Langmuir* **2006**, *22*, 2811.

(7) Boudou, T.; Crouzier, T.; Ren, K. F.; Blin, G.; Picart, C. *Adv. Mater.* **2010**, *22*, 441.

(8) Vak, D. J.; Kim, S. S.; Jo, J.; Oh, S. H.; Na, S. I.; Kim, J. W.; Kim, D. Y. *Appl. Phys. Lett.* **2007**, *91*.

(9) Sirringhaus, H.; Kawase, T.; Friend, R. H.; Shimoda, T.; Inbasekaran, M.; Wu, W.; Woo, E. P. *Science* **2000**, *290*, 2123.

(10) Cimrova, V.; Schmidt, W.; Rulkens, R.; Schulze, M.; Meyer, W.; Neher, D. *Adv. Mater.* **1996**, *8*, 585.

(11) Neher, D.; Gruner, J.; Cimrova, V.; Schmidt, W.; Rulkens, R.; Lauter, U. *Polym. Adv. Tech.* **1998**, *9*, 461.

(12) Seo, J. H.; Yang, R. Q.; Brzezinski, J. Z.; Walker, B.; Bazan, G. C.; Nguyen, T. Q. *Adv. Mater.* **2009**, *21*, 1006.

(13) Leger, J. M. *Adv. Mater.* **2008**, *20*, 837.

(14) Yang, R.; Garcia, A.; Korystov, D.; Mikhailovsky, A.; Bazan, G. C.; Nguyen, T.-Q. *J. Am. Chem. Soc.* **2006**, *128*, 16532.

(15) Arroyo-Villan, M. I.; Diaz-Quijada, G. A.; Abdou, M. S. A.; Holdcroft, S. *Macromolecules* **1995**, *28*, 975.

(16) Pochan, J. M.; Pochan, D. F.; Rommelmann, H.; Gibson, H. W. *Macromolecules* **1981**, *14*, 110.

(17) Gibson, H. W.; Pochan, J. M. *Macromolecules* **1982**, *15*, 242.

(18) Sarkas, H. W.; Kwan, W.; Flom, S. R.; Merritt, C. D.; Kafafi, Z. H. *J. Phys. Chem.* **1996**, *100*, 5169.

(19) Hintz, H.; Egelhaaf, H. J.; Luer, L.; Hauch, J.; Peisert, H.; Chasse, T. *Chem. Mater.* **2011**, *23*, 145.

(20) Abdou, M. S. A.; Orfino, F. P.; Son, Y.; Holdcroft, S. *J. Am. Chem. Soc.* **1997**, *119*, 4518.

(21) Gorman, C. B.; Ginsburg, E. J.; Grubbs, R. H. *J. Am. Chem. Soc.* **1993**, *115*, 1397.

(22) Gao, L.; Johnston, D.; Lonergan, M. C. *Macromolecules* **2008**, *41*, 4071.

(23) Bredas, J. L.; Street, G. B. *Acc. Chem. Res.* **1985**, *18*, 309.

(24) Kojima, M.; Nagasaka, K.; Ishii, T. *Infrared Phys.* **1986**, *26*, 299.

(25) Rabolt, J. F.; Clarke, T. C.; Street, G. B. *J. Chem. Phys.* **1979**, *71*, 4614.

(26) Rabolt, J. F.; Clarke, T. C.; Street, G. B. *J. Chem. Phys.* **1982**, *76*, 5781.

(27) Piaggio, P.; Dellepiane, G.; Mulazzi, E.; Tubino, R. *Polymer* **1987**, *28*, 563.

(28) Nguyen, T. Q.; Martini, I. B.; Liu, J.; Schwartz, B. J. *J. Phys. Chem. B* **2000**, *104*, 237.

(29) Ikenoue, Y.; Chiang, J.; Patil, A. O.; Wudl, F.; Heeger, A. J. *J. Am. Chem. Soc.* **1988**, *110*, 2983.

(30) Liao, H. H.; Yang, C. M.; Liu, C. C.; Horng, S. F.; Meng, H. F.; Shy, J. T. *J Appl Phys* **2008**, *103*.

(31) Inzelt, G. Conducting polymers : a new era in electrochemistry; Springer: Berlin, 2008.

Chapter IV

(1) Jorgensen, M.; Norrman, K.; Krebs, F. C. *Sol. Energ. Mat. Sol. C.*, **2008,** *92*, 686-714.

(2) Reese, M. O.; Nardes, A. M.; Rupert, B. L.; Larsen, R. E.; Olson, D. C.; Lloyd, M. T.; Shaheen, S. E.; Ginley, D. S.; Rumbles, G.; Kopidakis, N. *Adv. Funct. Mater.*, **2010,** *20*, 3476-3483.

(3) Aguirre, A.; Meskers, S. C. J.; Janssen, R. A. J.; Egelhaaf, H. J. *Org. Electron.*, **2011,** *12*, 1657-1662.

(4) Seemann, A.; Egelhaaf, H. J.; Brabec, C. J.; Hauch, J. A. *Org. Electron.*, **2009,** *10*, 1424-1428.

(5) Lipson, S. M.; O'Brien, D. F.; Byrne, H. J.; Davey, A. P.; Blau, W. J. *Synth. Met.*, **2000,** *111*, 553-557.

(6) Manceau, M.; Bundgaard, E.; Carle, J. E.; Hagemann, O.; Helgesen, M.; Sondergaard, R.; Jorgensen, M.; Krebs, F. C. *J. Mater. Chem.*, **2011,** *21*, 4132-4141.

(7) Chandross, E. A. *Science,* **2011,** *333*, 35-36.

(8) Abdou, M. S. A.; Orfino, F. P.; Son, Y.; Holdcroft, S. *J. Am. Chem. Soc.*, **1997,** *119*, 4518-4524.

(9) Hintz, H.; Egelhaaf, H. J.; Luer, L.; Hauch, J.; Peisert, H.; Chasse, T. *Chem. Mater.*, **2011,** *23*, 145-154.

(10) Sperlich, A.; Kraus, H.; Deibel, C.; Blok, H.; Schmidt, J.; Dyakonov, V. *J. Phys. Chem. B*, **2011,** *115*, 13513-13532.

(11) Cook, S.; Furube, A.; Katoh, R. *J. Mater. Chem.*, **2012,** Advance Article.

(12) Hintz, H.; Peisert, H.; Egelhaaf, H. J.; Chasse, T. *J. Phys. Chem. C*, **2011,** *115*, 13373-13376.

(13) Liao, H. H.; Yang, C. M.; Liu, C. C.; Horng, S. F.; Meng, H. F.; Shy, J. T. *J. Appl. Phys.*, **2008,** *103, 104506*.

(14) Luer, L.; Egelhaaf, H. J.; Oelkrug, D.; Cerullo, G.; Lanzani, G.; Huisman, B. H.; de Leeuw, D. *Org. Electron.*, **2004,** *5*, 83-89.

(15) Sarkas, H. W.; Kwan, W.; Flom, S. R.; Merritt, C. D.; Kafafi, Z. H. *J. Phys. Chem.*, **1996,** *100*, 5169-5171.

(16) Golovnin, I. V.; Bakulin, A. A.; Zapunidy, S. A.; Nechvolodova, E. M.; Paraschuk, D. Y. *Appl. Phys. Lett.*, **2008,** *92, 243311*.

(17) Chambon, S.; Rivaton, A.; Gardette, J.-L.; Firon, M. *Sol. Energ. Mat. Sol*., **2007,** 91, 394-398.

(18) Weber, C. D.; Robinson, S. G.; Lonergan, M. C. *Macromolecules*, **2011,** *44*, 4600-4604.

(19) Arroyo-Villan, M. I.; Diazquijada, G. A.; Abdou, M. S. A.; Holdcroft, S. *Macromolecules*, **1995,** *28*, 975-984.

(20) Tran-Van, F.; Carrier, M.; Chevrot, C. *Synth. Met.*, **2004,** *142*, 251-258.

(21) Koch, M.; Nicolaescu, R.; Kamat, P. V. *J. Phys. Chem. C*, **2009,** *113*, 11507-11513.

(22) Yamamoto, T. *Chem. Lett.*, **2003,** *32*, 334-335.

(23) Abdou, M. S. A.; Holdcroft, S. *Macromolecules*, **1993,** *26*, 2954-2962.

(24) Holdcroft, S. *Macromolecules*, **1991,** *24*, 4834-4838.

(25) Navarrete, J. T. L.; Zerbi, G. *J. Chem. Phys.*, **1991,** *94*, 965-970.

(26) Moraes, F.; Schaffer, H.; Kobayashi, M.; Heeger, A. J.; Wudl, F. *Phys. Rev. B*, **1984,** *30*, 2948-2950.

(27) Ivaska, A.; Osterholm, J. E.; Passiniemi, P.; Kuivalainen, P.; Isotalo, H.; Stubb, H. *Synth. Met.*, **1987,** *21*, 215-221.

(28) Ogilby, P. R.; Kristiansen, M.; Clough, R. L. *Macromolecules*, **1990,** *23*, 2698-2704.

(29) Manceau, M.; Rivaton, A.; Gardette, J. L.; Guillerez, S.; Lemaitre, N. *Polym. Degrad. Stabil.*, **2009,** *94*, 898-907.

(30) Osterbacka, R.; An, C. P.; Jiang, X. M.; Vardeny, Z. V. *Science*, **2000,** *287*, 839-842.

(31) Zhuo, J. M.; Zhao, L. H.; Png, R. Q.; Wong, L. Y.; Chia, P. J.; Tang, J. C.; Sivaramakrishnan, S.; Zhou, M.; Ou, E. C. W.; Chua, S. J.; Sim, W. S.; Chua, L. L.; Ho, P. K. H. *Adv. Mater.*, **2009,** *21*, 4747-4752.

(32) Kusoglu, A.; Modestino, M. A.; Hexemer, A.; Segalman, R. A.; Weber, A. Z. *ACS Macro Lett.*, **2012,** *1*, 33-36.

(33) Freund, M. S.; Deore, B. *Self-doped conductiong polymers*; Wiley: West Sussex, England ; Hoboken, NJ, 2006.

(34) Blatter, F.; Frei, H. *J. Am. Chem. Soc.*, **1993,** *115*, 7501-7502.

(35) Robbins, R. J.; Ramamurthy, V. *Chem. Commun.*, **1997,** 1071-1072.

(36) Clennan, E. L.; Pace, A. *Tetrahedron*, **2005,** *61*, 6665-6691.

(37) Lowry, S.R.; Maurritz, K.A. *J. Am. Chem. Soc.*, **1980,** 102, 4665-4667.

(38) Dupuis, A.; Wong-Wah-Chung, P.; Rivaton, A.; Gardette, J.-L. *Polym. Degrad. Stabil.*, **2012,** 97, 366-374.

Chapter V

(1) Z. He, C. Zhoung, S. Su, M. Xu, H. Wu, Y. Cao, Enhanced power-conversion efficiency in polymer solar cells using an inverted geometry, Nat. Photonics 6 (2012) 591-595.

(2) H.-L. Yip, A. K.-Y. Jen, Recent advances in solution-processed interfacial layers for efficient and stable polymer solar cells, Environ. Sci. 5 (2012) 5994-6011 .

(3) F. Zhang, X. Xu, W. Tang, J. Zhang, Z. Zhou, J. Wang, J. Wang, Z. Xu, Y. Wang, Recent development of the inverted configuration organic solar cells, Sol. Energy Mater. Sol. Cells 95 (2011) 1785-1799.

(4) R. Po, C. Carbonera, A. Bernardi, N. Camaioni, The role of buffer layers in polymer solar cells, Energy Environ. Sci. 4 (2011) 285-310.

(5) E. L. Ratcliff, A. Garcia, S. A. Paniagua, S. R. Cowen, A. J. Giordano, D. S. Ginley, S. R. Marder, J. J. Berry, D. C. Olsen, Investigating the influence of interfacial contact properties on open circuit voltages in organic photovoltaic performance: work function versus selectivity, Adv. Eng. Mater. 3 (2013) 647-656.

(6) C. Brabec, V. Dyakonov, J. Parisi, and N.S. Sariciftci, Organic Photovoltaics: Concepts and Realization, Springer, Berlin, 2003.

(7) C. Waldauf, M. Morana, P. Denk, P. Schilinsky, K. Coakley, S. A. Choulis, C. J. Brabec, Highly efficient inverted organic photovoltaics using solution based titanium oxide as electron selective contact, Appl. Phys. Lett. 89 (2006) 233517.

(8) A. K. Kyaw, X. W. Sun, C. Y. Jiang, G. Q. Lo, D. W. Zhao, D. L. Kwong, An inverted organic solar cell employing a sol-gel derived ZnO electron selective layer and thermal evaporated MoO_3 hole selective layer, Appl. Phys. Lett 93 (2008) 221107.

(9) G. Jo, S.-I. Na, S.-H. Oh, S. Lee, T.-S. Kim, G. Wang, M. Choe, W. Park, J. Yoon, D.-Y. Kim, Y. H. Kahng, T. Lee, Tuning of a graphene-electrode work function to enhance the efficiency of organic bulk heterojunction photovoltaic cells with an inverted structure, Appl. Phys. Lett. 97 (2010) 213301.

(10) Y.-Y. Lai, P.-I. Shih, Y.-P. Li, C.-E. Tsai, J.-S. Wu, Y.-J. Cheng, C.-S. Hsu, Interface engineering to enhance the efficiency of conventional polymer solar cells by alcohol-/water soluble C_{60} materials doped with alkali carbonates, ACS Appl. Mater. Inter. 5 (2013) 5122-5128.

(11) C. Duan, C. Zhong, C. Liu, F. Huang, Y. Cao, Highly efficient inverted polymer solar cells based on an alcohol soluble fullerene derivative interfacial modification material, Chem. Mater. 24 (2012) 1682-1689.

(12) S. K. Hau, H.-L. Yip, O. Acton, N. S. Baek, H. Ma, A. K.-Y. Jen, Interfacial modification to improve inverted polymer solar cells, J. Mater. Chem. 18 (2008) 5113-5119.

(13) S. K. Hau, H.-L. Yip, H. Ma, A. K.-Y. Jen, High performance ambient processed inverted polymer solar cells through interfacial modification with a fullerene self-assembled monolayer, Appl. Phys. Lett. 93 (2008) 233304.

(14) T. Yang, M. Wang, C. Duan, X. Hu, L. Huang, J. Peng, F. Huang, X. Gong, Inverted polymer solar cells with 8.4% efficiency by conjugated polyelectrolyte, Energy Environ. Sci. 5 (2012) 8208-8214.

(15) S.-I. Na, T.-S. Kim, S-H. Oh, S.-S. Kim, D.-Y. Kim, Enhanced performance of inverted polymer solar cells with cathode interfacial tuning via-water soluble polyfluorenes, Appl. Phys. Lett. 97 (2010) 223305.

(16) J. H. Seo, A. Gutacker, B. Walker, S. Cho, A. Garcia, R. Yang, T.-Q. Nguyen, A. J. Heeger, G. C. Bazan, Improved injection in n-type organic transistors with conjugated polyelectrolytes, J. Am. Chem. Soc. 131 (2009) 18220-18221.

(17) K. Zilberberg, A. Behrendt, M. Kraft, U. Scherf, T. Riedl, Ultrathin interlayers of a conjugated polyelectrolyte for low work-function cathodes in efficient inverted organic solar cells, Org. Electron. 14 (2013) 951-957.

(18) C.-Z. Li, C.-C. Chueh, H.-L. Yip, K. M. O'Malley, W.-C. Chen, A. K.-Y. Jen, Effective interfacial layer to enhance efficiency of polymer solar cells via solution processed fullerene surfactants, J. Mater. Chem. 22 (2012) 8574-8577.

(19) C.-H. Hsieh, Y.-J. Cheng, P.-J. Li, C.-H. Chen, M. Dubosc, R.-M. Liang, C.-S. Hsu, Highly efficient and stable inverted polymer solar cells integrated with a cross-linked fullerene material as an interlayer, J. Am. Chem. Soc. 132 (2010) 4887-4893.

(20) N. Cho, H.-L. Yip, S. K. Hau, K.-S. Chen, T.-W. Kim, J. A. Davies, D. F. Ziegler, A. K.-Y. Jen, n-doping of thermally polymerizable fullerenes as an electron transporting layer for inverted polymer solar cells, J. Mater. Chem. 21 (2011) 6956-6961.

(21) A. Barbot, B. Lucas, C. D. Bin, B. Ratier, M. Aldissi, Optimized inverted polymer solar cells incorporating Cs_2CO_3-doped C_{60} as electron transport layer, Appl. Phys. Lett. 102 (2013) 193305.

(22) D. K. Schroder, Semiconductor Material and Device Characterization, 3rd Ed., IEEE Press, New York, 2006, p. 209.

(23) B. Qi, J. Wang, Open-circuit voltage in organic solar cells, J. Mater. Chem. 22 (2012) 24315-24325.

(24) C. He, C. Zhong, H. Wu, R. Yang, F. Huang, G. C. Bazan, Y. Cao, Origin of the enhanced open-circuit voltage in polymer solar cells via interfacial modification using conjugated polyelectrolytes, J. Mater. Chem 20 (2010) 2617-2622.

(25) A. Hamed, Y. Sun, Y. Tao, R. Meng, P. Hor, The effect of oxygen and illumination of the in-situ conductivity of C60 thin films, Phys. Rev. B Condens. Matter. 47 (1993) 10873-10880.

(26) C.-Z. Li, C.-C. Chueh, H.-L. Yip, F. Ding, X. Li, A. K.-Y. Jen, Solution-processible highly conductive fullerenes, Adv. Mater 25 (2013) 2457-2461.

(27) T. H. Reilly III, A. W. Hains, H.-Y. Chen, B. Gregg, A self-doping, O_2 stable, n-type interfacial layer for organic electronics, Adv. Eng. Mater**.** 2 (2012) 455-460.

(28) A. Garcia, J. Z. Brzezinski, T.-Q. Nguyen, Cationic conjugated polyelectrolyte electron injection layers: effect of halide counterions, J. Phys. Chem. C 113 (2009) 2950-2954.

(29) D. R. Lawson, D. L. Feldheim, C. A. Foss, P. K. Dorhout, C. M. Elliott, C. R. Martin, B. Parkinson, Near-IR absorption spectra for the buckminsterfullerene anions: an experimental and theoretical study, J. Electrochem. Soc. 139 (1992) L68-71.

Chapter VI

(1) H. -L. Yip and A. K.-Y. Jen, *Energy Environ. Sci*., 2012, **2**, 5994-6011.

(2) T. Yang, M. Wang, C. Duan, X. Hu, L. Huang, J. Peng, F. Huang and X. Gong, *Energy Environ. Sci*., 2012, **5**, 8202-8214.

(3) C. -Z. Li, C. -C. Chueh, H. -L. Yip, K. M. O'Malley, W. -C. Chen and A. K. -Y. Jen, *J. Mater . Chem*., 2012, **22**, 8574-8577.

(4) Z. He, C. Zhong, S. Su, M. Xu and Yong Cao, *Nat. Photonics*, 2012, 6, 591-595.

(5) Na, S. -I.; Kim, T. -S.; Oh, S. -S.; Kim, J.; Kim, D. -Y. *Appl. Phys. Lett.*, **2010**, 223305.

(6) G. Li, C. V. Shrotriya, J. Huang and Y. Yang, *Appl. Phys. Lett*., 2006, **88**, 253503.

(7) L. Jiang, A. Li, X. Deng, S. Zheng and K. -Y. Wong, *Appl. Phys. Lett*., 2013, **102**, 013303.

(8) T. H. Reilly III, A. W. Hains, H. -Y. Chen and B. A. Gregg, *Adv. Energy. Mater.*, 2012, **2**, 455-460.

(9) Y. Vaynzof, D. Kabra, L. L. Chua and R. H. Friend, *Appl. Phys. Lett*., 2011, **98**, 113306.

(10) C. Duan, W. Cai, B. B. Y. Hsu, C. Zhong, K. Zhang, C. Liu, Z. Hu, F. Huang, G. C. Bazan, A. J. Heeger and Yong Cao, *Energy Environ. Sci*., 2013, **6**, 3022-3034.

(11) C. -Z. Li, C. -C. Chueh, H. -L. Yip, F. Ding, X. Li and A. K. -Y. Jen, *Adv. Mater*., 2013, **25**, 2457-2461.

(12) C. -Z. Li, C. -C. Chueh, F. Ding, H. -L. Yip, P. -W. Liang, X. Li and A. K. -Y. Jen, *Adv. Mater*., 2013, **25**, 4425-4430.

(13) D. Albanese, D. Landini and Michele Penso, *J. Org. Chem*., 1998, **63**, 9587-9589.

(14) L. Echegoyen, F. Diederich and L. E. Echegoyen, in *Fullerenes: Chemistry, Physics, and Technology*, ed. K. M. Kadish and R. S. Ruoff, Wiley-Interscience, USA, 2000, ch 1, pp 1-53.

(15) W. -W. Chang, Z. -J. Li, W. -W. Yang and X. Gao, *Org. Lett*., 2012, **14**, 2386-2389.

(16) S. Fukuzumi, I. Nakanshi, J. Maruta, T. Yorisue, T. Suenobu, S. Itoh, R. Arakawa and K. M. Kadish, *J. Am. Chem. Soc*., 1998, **120**, 6673-6680.

(17) H. - L. Hou, Z. -J. Li, S. -H. Li, S. Chen and X. Gao, *Org. Lett*., 2013, **15**, 4646-4649.

(18) S. -E. Zhu, F. Li and G. -W. Wang, *Chem. Soc. Rev*., 2013, **42**, 7535-7570.

(19) M. Baumgarten, A. Gugel and L. Gherghel, *Adv. Mater*., 1993, **5**, 458-461.

(20) C. A. Reed and R. D. Bolskar, *Chem. Rev*., 2000, **100**, 1075-1120.

(21) M. Guldi and M. Prato, *Acc. Chem. Res*., 2000, **33**, 695-703.

(22) D. R. Lawson, D. L. Feldheim, C. A. Foss, P. K. Dorhout, C. M. Elliott, C. R. Martin and Bruce Parkinson, *J. Electrochem. Soc.*, 1992, **139**, L68-L71.

(23) R. D. Bolskar, S. H. Galleger, R. S. Armstrong, P. A. Lay and C. A. Reed, *Chem. Phys. Lett.*, 1995, **247**, 57-62.

(24) V. Brezova, A. Stasko, P. Rapta, G. Domschke, A. Bartl and L. Dunsch, *J. Phys. Chem.*, 1995, **99**, 16234-16241.

(25) D. M. Guldi, H. Hungerbuhler, E. Janata and K. -D. Asmus, *J. Phys. Chem.*, 1993, **97**, 11258-11264.

(26) D. M. Guldi, H. Hungerbuhler and K. -D. Asmus, *J. Phys. Chem. A*, 1997, **10**, 1783-1786.

(27) H. Mohan, D. K. Palit, J. P. Mittal, K. -D. Asmus and D. M. Guldi, *J. Chem. Soc. Faraday Trans.*, 1998, **94**, 359-363.

(28) M. D. Tzirakis and M. Orfanopoulos, *Chem. Rev.*, 2013, **113**, 5262-5321.

(29) S. Fukuzumi, I. Nakanishi, T. Suenobu and K. M. Kadish, *J. Am. Chem. Soc.,* 1999, **121**, 3468-3474.

(30) R. Taylor, J. H. Holloway, E. G. Hope, A. G. Avent, G. J. Langley, T. J. Dennis, J. P. Hare, H. W. Kroto and D. R. M. Walton, *J. Chem. Soc. Chem. Comm.,* 1992, **9**, 665-667.

(31) R. K. Sharma and J. L. Fry, *J. Org. Chem.,* 1983, **48**, 2112-2114.

(32) K. G. Thomas, V. Biju, M. V. George, D. M. Guldi and P. V. Kamat, *J. Phys. Chem. A*, 1998, **102**, 5341-5348.

(33) H. Tamura and M. Tsukada, *Phys. Rev. B*, 2012, **85**, 054301.

(34) A. Wrzyszczynski, M. Pietrzak, J. Bartoszewicz, H. Kozubek, G. L. Hug, B. Marciniak and J. Paczkowski, *J. Am. Chem. Soc.,* 2003, **125**, 11182-11183.

(35) D. P. Cox, J. Terpinski and W. Lawrynowicz, *J. Org. Chem.,* 1984, **49**, 3216-3219.

(36) G. -W. Wang, X. -P. Chen and X. Cheng, *Chem. Eur. J.,* 2006, **12**, 7246-7253.